Investigation of a CalPhaD Approach for the Prediction of Solidification Segregation and its Effect on Solid State Transformations

Dissertation

Presented in Partial Fulfillment of the Requirements for the Degree Doctor of Philosophy
in the Graduate School of The Ohio State University

By

Guilherme Abreu Faria, M. Sc

Graduate Program in Welding Engineering

The Ohio State University

2019

Dissertation Committee

Dr. Antonio Ramirez, Advisor

Dr. Wei Zhang, Member

Dr. Carolin Fink, Member

Abstract

During solidification of multi-component systems, composition partition between the liquid and solid phases is inevitable in most practical applications. This partition induces a segregation profile in the solid phase, which may affect solid-state transformation behavior. Several models exist both to address the formation of this segregation profile and solid-state phase transformations. The ability to model the full history of the material allows for digital testing of manufacturing process parameters, new alloy compositions and post solidification heat treatments.

In this work, we investigate a modelling approach which uses several CalPhaD based models to follow the materials history and the phase transformations taking place during it. The basis and outline are presented and the modelling approach is applied to follow two cases, Cu phase formation in a Grade 91 Creep Strength Enhanced Ferritic Steel and solidification and phase transformations in a non-homogenized alloy 718 material produced through Laser powder bed additive manufacturing. The results of the model application are presented in article form. The first article correlates creep damage to second phase particles coming from solidification. The second article establishes a mechanism for the formation of a Cu phase layer around the second phase particles. The third article compares results of the Scheil model to segregation maps in as-built

additively manufactured alloy 718. The fourth article uses a modelled segregation profile in alloy 718 to model δ phase formation in a heat treatment of the non-homogenized sample, and compares results with in-situ x-ray diffraction quantification of the δ phase. The document concludes with an analyses of the accuracy of the modelling approach and a discussion of the sensibility of the model to its inputs.

Dedication

I dedicate this work to my partner, Julia, to my parents and brother, and to my Columbus family.

I am merely a reflection of your love and support.

Acknowledgments

I would like to acknowledge the support of several different agencies:

- The Electric Power Research Institute (EPRI), for funding and collaboration on the research presented;
- The Institute of Materials Research (IMR) at OSU, for funding on the research presented;
- The Manufacturing and Materials Joining Innovation Center (Ma2JIC), for funding on the research presented;
- The U.S. National Aeronautics and Space Administration (NASA) ESI Program, which supported the work through Award No. NNX17AD13G;
- The American Welding Society (AWS) for a graduate research fellowship;
- Arconic, for providing materials used in the research presented.

The work shown in this document was obtained through the collaboration of several students, professors and researchers. I would like to particularly thank

Alejandro Hinojos,

Kamalnath Kadirvel,

Sebastian Romo,

John Siefert,

Dr. Julian. D. Escobar,

Dr. Xuesong Gao,

Dr. João. P. Oliveira,

Dr. Jonathan Parker,

Dr. Camilo. F. Salvador,

Prof. Boian Alexandrov,

Prof. Yunzhi Wang,

Prof. Wei Zhang,

and especially Prof. Antonio Ramirez.

I would also like to thank Prof. Ramirez's group for the invaluable discussions, and the broader Welding Engineering, Materials Science and Engineering and CEMAS student and staff community for the engaging conversations and knowledge exchange so easily attainable.

Vita

2011……………………………………… B.S. Physics, State University of Campinas

2014……………………………………… M. Sc. Mechanical Engineering, State University of Campinas

2015 to present……………………………… Graduate Research Associate, Welding Engineering Program, Department of Materials Science and Engineering, The Ohio State University.

Publications

1) FARIA, G. A. et al. On the use of metastable interface equilibrium assumptions on prediction of solidification micro-segregation in laser powder bed fusion, **Science and Technology of Welding & Joining**, published online in April 2019 - https://doi.org/10.1080/13621718.2019.1608406

2) ESCOBAR, J. D. et al. Fundamentals of Isothermal Austenite Reversion in a Ti-Stabilized 12cr - 6 Ni - 2 Mo Super Martensitic Stainless Steels: Thermodynamics Versus Experimental Assessments (January 4, 2019). Available at SSRN: https://ssrn.com/abstract=3310170

3) BO, M. R. D.; SALVADOR C. A. F. et al. The effect of Zr and Sn additions on the microstructure of Ti-Nb-Fe gum metals with high elastic admissible strain, **Materials and Design**, vol. 160, 1186-1195, 2018 https://doi.org/10.1016/j.matdes.2018.10.040

4) ESCOBAR, J. D. et al. Meta-equilibrium transition microstructure for maximum austenite stability and minimum hardness in a Ti-stabilized supermartensitic stainless steel, **Materials & design, vol.** 156, 609-621, 2018 https://doi.org/10.1016/j.matdes.2018.07.018

5) GILES, C. et al. Compact arrangement for femtosecond laser-induced generation of broadband hard x-ray pulses, in *High-Brightness Sources and Light-driven Interactions*, OSA Technical Digest (online) (Optical Society of America, 2018), paper ET1B.3. https://doi.org/10.1364/EUVXRAY.2018.ET1B.3

6) ESCOBAR, J. D. et al. Compositional analysis on the reverted austenite and tempered martensite in a Ti-stabilized supermartensitic stainless steel: Segregation, partitioning and carbide precipitation, **Materials & design, vol.** 140, 95-105, 2018 https://doi.org/10.1016/j.matdes.2017.11.055

7) ESCOBAR, J. D. et al. Austenite reversion kinetics and stability during tempering of a Ti-stabilized supermartensitic stainless steel: correlative in situ synchrotron x-ray diffraction and dilatometry, **Acta Materialia**, vol. 138, 92-99, 2017, https://doi.org/10.1016/j.actamat.2017.07.036

8) PARKER J. et al. Life Management of 9%Cr Steels: Assessment of Damage in Ex-Service Grade 91 Steel Stub-to-Header Welds, **EPRI**, Palo Alto, CA, 2017

9) SMITH, R. T. et al. In situ X-ray diffraction analysis of strain-induced transformations in Fe- and Co-base hardfacing alloys. **Scripta Materialia**, v. 98, p. 60–63, mar. 2015. https://doi.org/10.1016/j.scriptamat.2014.11.003

10) MARDEGAN, J. R. L. et al. Magnetic structure of R2CoGa8 (R = Gd, Tb, and Dy): Structural tuning of magnetic properties in layered Ga-based intermetallic compounds. **Physical Review B**, v. 89, n. 11, p. 115103, 4 mar. 2014. https://doi.org/10.1103/PhysRevB.89.115103

11) FARIA, G. A. et al. *Advanced Facility For Parallel Thermo-Mechanical Simulation And Synchrotron X-Ray Diffraction.* In: KANNENGIESSER, T. et al. (Eds.). **In-situ Studies with Photons, Neutrons and Electrons Scattering II**. 1st. ed. Springer, 2014. p. 245–259. https://doi.org/10.1007/978-3-319-06145-0_15

12) SANTOS, R. DA S. et al. Iron insertion and hematite segregation on Fe-doped TiO2 nanoparticles obtained from sol-gel and hydrothermal methods. **ACS applied materials & interfaces**, v. 4, n. 10, p. 5555–61, 24 out. 2012. https://doi.org/10.1021/am301444k

13) ADRIANO, C. et al. *Magnetic structure of Ho2CoGa8 determined by X-ray resonant magnetic scattering*. **Physica B: Condensed Matter**, v. 404, n. 19, p. 3289–3292, out. 2009. https://doi.org/10.1016/j.physb.2009.07.127

Fields of Study

Major Field: Welding Engineering

Table of Contents

List of Tables

List of Figures

Chapter 1. Introduction

In fusion based manufacturing techniques, solidification is accompanied by a distinctive microstructure marked by segregation. This chemical partitioning leads to the formation of eutectic phases such as carbide, intermetallic and inclusion particles in interdendritic regions. It also leads to a compositional gradient along dendrites, creating local chemical compositions distinct from the bulk. Segregation has been associated with many performance issues in several classes of alloys, from steels to Ni based precipitation strengthened materials. These issues are typically associated with the formation or dissolution of phases in a way that is distinct from what would happen in a homogenized material with a bulk composition.

CalPhaD based methodologies have been widely used to predict the formation and dissolution of phases during heat treatments and service conditions with outstanding successful results. However, such approaches are based on calculations using bulk compositions and fail to predict the formation of some phases in solidification microstructures, exactly due to the varying local compositions arising from solidification. On the other hand, CalPhaD based methods for non-equilibrium solidification are available in the literature and have a high degree of success in predicting solidification partitioning and the formation of eutectic phases during solidification.

This project aims at establishing a CalPhaD based modelling procedure that addresses phase transformations in segregated solidification microstructures. The methodology will use a non-equilibrium solidification model to predict solidification microstructures and a local evaluation of the thermodynamic state of the solidified system once solidification finishes, performed through recognized CalPhaD based methodologies. Additionally, the methodology will be extended for heat treatments performed after solidification, considering the kinetic aspects of the microstructure evolution, such as compositional homogenization and phase growth. The methodology was applied in two application cases, one cast steel P91 alloy and one Ni superalloy manufactured through Laser powder bed additive manufacturing. These alloys present a number of challenges from a CalPhaD standpoint. The steel experiences a complex thermo-mechanical history, and on the Ni alloy, the complex interaction of the alloying elements allows a number of different phases to form, while the additive manufacturing process itself creates a unique thermal gradient and microstructures. Together these present an optimal benchmark for the modelling approach to be verified.

The results obtained are presented in the form of ready for submission or published articles. Overall, the studies presented focus on extensive CalPhaD analysis. Other CalPhaD based studies performed by the student include:

- J. D. Escobar et al., “Fundamentals of isothermal austenite reversion in a Ti-stabilized 12Cr – 6 Ni – 2 Mo super martensitic stainless steel: Thermodynamics versus experimental assessments," Acta Mater., vol. 174, pp. 246–259, Aug. 2019.

- M. R. Dal Bó et al., "The effect of Zr and Sn additions on the microstructure of Ti-Nb-Fe gum metals with high elastic admissible strain," Mater. Des., vol. 160, pp. 1186–1195, Dec. 2018.

These are relevant to the CalPhaD methods shown in this document, but not directly correlated with the theme of the thesis and will not be presented.

Chapter 2. Background

2.1. Motivation

During solidification of alloys there will be a region in which the solid and liquid phases will be present at the same time. The different energy configurations of these phases incur that in an absolute majority of cases, the two phases will have their energies minimized if a compositional partitioning occurs. This partitioning is behind a few different phenomena involved in the solidification process, including:

- The undercooling necessary for homogeneous nucleation, where nuclei will have a composition different from the liquid;
- The interface instability associated with cell and dendrite formation;
- The disparity between the equilibrium solidification temperature range and what is observed under normal manufacturing conditions (welding, casting, etc.);
- The micro and macrosegregation profiles observed within the solidification microstructure.

The last point is of special interest for alloy systems requiring heat treatments. Once the material solidifies, the segregated solidified microstructure will tend to homogenize, but often, there is no time during cooling for homogenization to be complete. If the material is submitted to a heat treatment designed for precipitation or other phase transformations, the local compositions will define a local thermodynamic state which will determine the characteristics of the phase transformation, e.g. solvus temperatures, thermodynamically stable phases, kinetics, etc. Dupont *et al* [1] present a case that exemplifies well this phenomena. Figure 1 shows a schematic representation of a segregated cell. If an alloy has a precipitate forming solute with a partition coefficient smaller than one, the cell core will have a leaner composition of this solute. This composition gradually grows towards the cell edge. The solvus temperature of the precipitate will vary with the solute composition. This is shown schematically on Figure 1 a. Figure 1 b shows the as built microstructure, assuming kinetics are enough for precipitation to occur during cooling on the solid state. The precipitate coarseness will be dependent on the temperature at which precipitation starts to occur, resulting in a morphology gradient. If the solute concentration is sufficiently low, precipitates will not form. Figure 1 c shows the result of a solubilization heat treatment made above the solvus temperature for the nominal composition, but below the solvus at the edge of the cell. In this condition, the pre-existing precipitates at the cell edge grow until an equilibrium condition is reached. Some homogenization of the compositional profile may take place, but not enough to dissolve the precipitates formed at high solute concentration areas. Figure 1 d shows what would happen when an aging treatment is done on the microstructure. The areas with pre-existing precipitates are close to an equilibrium condition, so little change takes place. A precipitate structure will appear in the regions of the dendrite containing sufficient solute, with different morphology than the existing one. Depending on the level of homogenization a morphological gradient may be present in this precipitate structure as well.

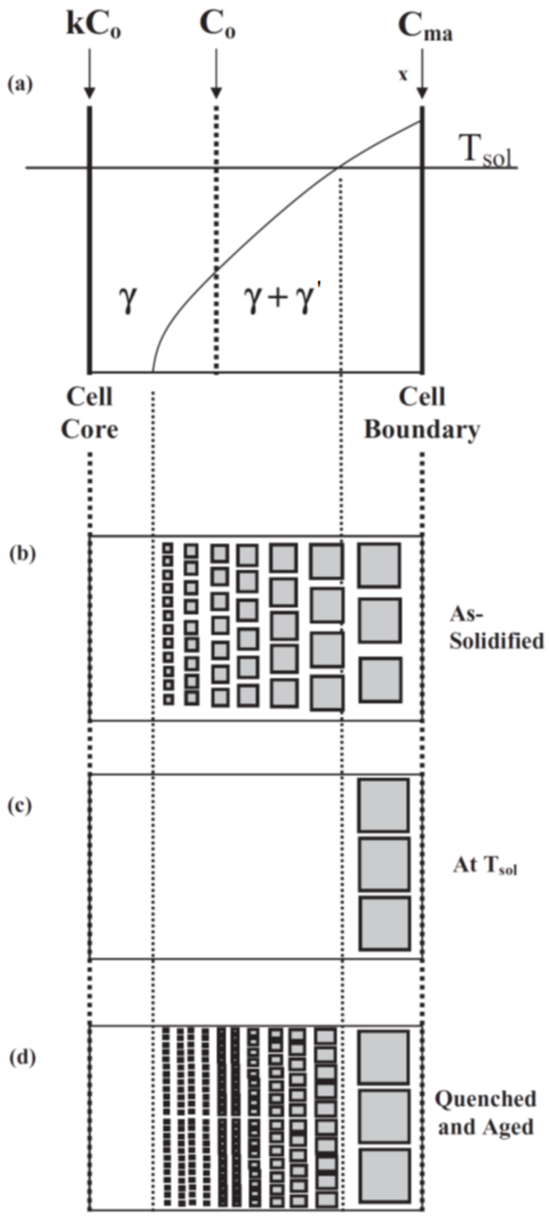

Figure 1: Schematic representation of the effect of segregation in the precipitation phase transformations taking place on a precipitation strengthened alloy during heat treatments. Adapted from [1].

Dupont *et al* also presents an actual case in which this behavior is visible. Figure 2 shows the microstructure of γ’ forming alloy 738 after solubilization and aging heat treatments. The coarsened precipitate structure can be seen around the dendrite edges. The dark region on Figure 2 a is the dendrite core. The precipitate structure is not visible at this magnification, but on the transmission image on Figure 2 b it can be seen.

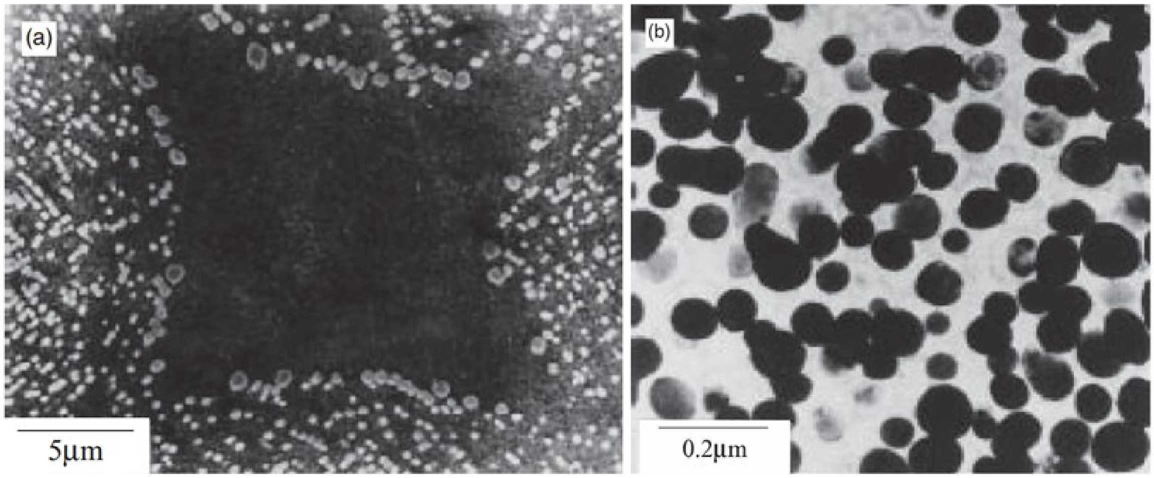

Figure 2: Microstructure of an alloy 738 gas tungsten arc weld. a) overview of dendritic structure. The cell core is visible in the center. b) High magnification image of cell core. From reference [1].

This example illustrates the need for an understanding of the solidification structure and its effect on solid state phase transformations. Understanding the segregation profile and being able to identify the effects of local compositions on the stability of second phases and their formation kinetics is essential to identify the microstructure evolution that may take place.

This information may be discovered computationally through the CalPhaD method. Three phenomena must be considered when addressing the solidification microstructure evolution:

- The formation of the segregation profile during solidification
- The compositional homogenization and dissolution of solidification second phases during cooling on the solid state and subsequent heat treatments
- The thermodynamic stability and kinetics of precipitation resolved for the segregation profile.

All three aspects can be resolved by CalPhaD based computational methods. The establishment of a workflow routine to address this problem allows for digital testing of alloys, the identification of potentially detrimental microstructural conditions, heat treatment temperatures and times. Furthermore, it allows for digital alloy design in high throughput computational experiments, where several alloying conditions are tested, and the resulting microstructure is evaluated to achieve an optimal condition. Finally, the computational methods can be incorporated in integrated computational materials engineering models to perform completely digital experiments, reducing cost on alloy development and process parameters optimization in different manufacturing techniques.

On the next session, we will discuss what the CalPhaD method is and how it can be used to identify the segregation structure and its effect on solid state transformations.

2.2. The CalPhaD Method

The CalPhaD methodology is based on the application of materials thermodynamic concepts for the construction of phase diagrams. In a phase diagram, a boundary identifies the transition point between different phase configurations. These boundaries are an indication of when a phase transformation becomes possible. For example, when a system experiences cooling, the liquidus line identifies the temperature beneath which a solid phase would become thermodynamically stable. Similarly, in a system being heated, the solidus indicates the temperature at which a liquid phase would become stable.

If the equations of state for a system are known, these boundaries can be identified analytically [2]. These equations of state can be any energy description of the system, such as Gibbs free energy or Helmholtz free energy. Thermodynamics states that at a phase boundary, the derivative of the system energy over its composition must be equal for all present phases. The coordinates of a phase diagram boundary can be found by identifying the points where derivatives, or tangents in binary systems) are equal for different phases. This concept is illustrated in Figure 3. Under such strategy, phase diagrams can be fully built if the Gibbs free energy formulation is known for the full range of temperature and composition analyzed.

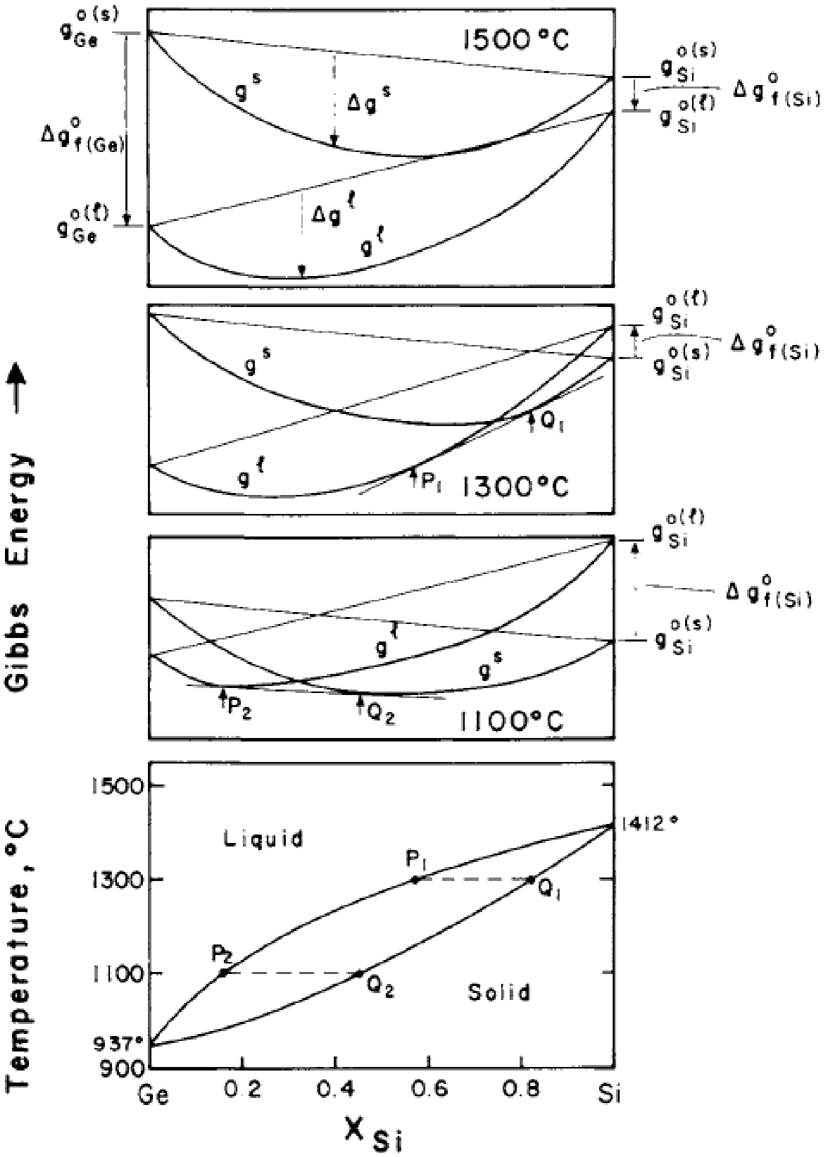

Figure 3: Construction of a Ge-Si phase diagram based on the evaluation of Gibbs free energy curves. Adapted from [2].

CalPhaD stands for Computational Calculation of Phase Diagrams. Although the strategy described was known before its introduction, it was within the CalPhaD framework that a computational strategy was devised and popularized. The history behind its development can be traced back to the beginning of the 20th century, where initial attempts to develop mathematical methods to calculate phase diagrams were presented by several authors. On the late 60s, Kaufman proposed a computational contextualization of one of these models, with considerable success on binary alloys [3]. This method was based on the construction of Gibbs free energy and other thermodynamic data for unary systems with a single phase, stable or otherwise, and describing a multicomponent system through a combination of the free energy contribution of all its components [4].

Kaufman's proposal was based on using a regular solution model to represent the Gibbs free energy of a solution. Under this formulation, the Gibbs free energy G'^{α} of phase α in a system can be described as:

$$G'^{\alpha} = \sum_i x_i G_i^{0\alpha} + RT \sum_i x_i \ln x_i + \sum_i \sum_{j>i} x_i x_j \Omega_{ij}^{\alpha} \qquad \text{eq. 1}$$

where

- x_i is the molar fraction of element *i*;
- $G_i^{0\alpha}$ is the Gibbs free energy of phase α in a unary system for element *i*;
- Ω_{ij}^{α} is a parameter independent of temperature and composition, but explicitly defined for phase α and element i.

In equation 1, the second term is the entropy addition from the mixing of elements in the solution. Analogously, the third term is the enthalpy of mixing, that is, the energy change due to the nature of bonds between atoms of different elements in the solution. This term may be positive or negative and will have a remarkable influence on the phase diagram.

For example, a large positive value is behind miscibility gaps, while a large negative value is associated with line compounds, that is, phases with specific stoichiometry. There are several formulations for the Ω parameter [5]. For example, a typical representation is the Redlich-Kister polynomial:

$$\Omega_{ij}^{\alpha} = \sum_{k=0}^{m} a_k^{ij,\alpha} \left(x_i - x_j\right)^k \qquad \text{eq. 2}$$

The term $a_k^{ij,\alpha}$ is defined for every phase α and element pair ij. Together with G^0, the information required to define parameter Ω must be known to make use of the CalPhaD method. Nowadays, thermochemical databases used in CalPhaD will contain the information necessary to define these parameters, allowing software to construct full n-1 dimensional Gibbs free energy surfaces.

The initial approach proposed by Kaufman predicted some inaccurate systems, but the improvement on existing approaches was successful enough that these sprouted discussion and community involvement. Further development followed, in part driven by the creation of the CalPhaD conference and journal and by the establishment of a community of researchers working on the field. The 70s and 80s were marked by improvements on the formulation of Ω and the development of software and databases from several research groups, culminating in user friendly, commercial products and better models and more accurate databases. This development continues to this day, where thermodynamic databases can be found for new systems such as high entropy alloys, and improved databases can be found for traditional systems, such as Ti and Al based alloys.

The last three decades also saw the development of software applying models which use phase diagram information to solve problems indirectly related to phase diagrams. Examples include models for solidification segregation, diffusion in solutions and precipitation reactions. The next sections will talk in detail about CalPhaD associated models addressing these three phenomena. The solidification portion will focus on composition as a function of fraction of solid type equations. These were chosen on this work due to their intrinsic compositional versatility and computational efficiency.

2.2.1. Solidification

From a practical point of view, solidification cannot happen in equilibrium. Full equilibrium represents the situation in which the solid and liquid will constantly have a homogenous composition, which is derived from the solidus and liquidus lines on the equilibrium phase diagram. This condition is achieved in geological times, but not in manufacturing processes. However, as discussed in [6], there are different degrees of departure from full equilibrium, based on an associated solidification rate. The faster the solidification, the farther the system will be from an equilibrium condition. These degrees can be organized in a hierarchy as shown on Table 1.

Table 1: Hierarchy of Equilibrium on Solidification. Adapted from [6]:

1) Full Diffusional (Global) Equilibrium	• No chemical potential gradients (composition of phases are uniform) • No temperature gradients • Lever rule applicable
2) Local Interfacial Equilibrium	• Chemical potential for each component continuous across the interface • Phase diagram gives compositions and temperatures only at Solid-Liquid interface
3) Metastable Local Interfacial Equilibrium	• Important when stable phase cannot nucleate or grow fast enough • Metastable phase diagram (a true thermodynamic phase diagram missing the stable phase or phases) gives the interface conditions
4) Interfacial Non-Equilibrium	• Phase diagram fails to give temperature and compositions at interface • Chemical potentials are not equal at interface

Typical manufacturing practices based on solidification include casting and many welding and additive manufacturing processes. In these processes the typical solidification conditions will be characterized by local interface equilibrium and local interface metastable equilibrium. Under these conditions, although the whole system is not at thermodynamic equilibrium, the solid-liquid interface will be at local equilibrium, i. e., the chemical potentials of an element must be equal on each side of the interface.

As such, CalPhaD derived information can still be used to evaluate the composition at the interface if the conditions of the system are known. These consist of temperature, local composition, etc. Naturally, these conditions will vary as the material solidifies, due to compositional partitioning between solid and liquid. Resolving these conditions require understanding the element balance between the solid and liquid phases, or rather, how diffusion affects the composition distribution across the two phases.

In a majority of practical applications, and particularly for welding, the cooling rate is such that the diffusion of substitutional solute in the solid state is negligible, whereas the dendrite arm spacing is reduced enough that the composition on the liquid is mostly homogeneous. If three assumptions are postulated as:

- The composition in the liquid is always homogeneous;
- There is no diffusion in the solid;
- At the interface, the composition of the solid is defined by the composition of the liquid through the partition coefficient ($C_S = k_0 C_L$);

Conservation of mass in the system forces the composition of the liquid to obey the following differential equation:

$$\frac{dC_L}{C_L} = \frac{1 - k_0}{1 - f_S} df_S \qquad \text{eq. 3}$$

If the system is dilute, the solidus and liquidus lines on the phase diagram can be considered as straight lines, and k_0 will be constant. In this case, this equation can be integrated to

$$C_L = C_0 (1 - f_S)^{k_0 - 1} \qquad \text{eq. 4}$$

$$C_L = C_0 k_0 (1 - f_S)^{k_0 - 1} \qquad \text{eq. 5}$$

Several authors have derived different forms of equation 4, namely Gulliver in 1922, Hayes and Chipman in 1938, Scheil in 1942 and Pfann in 1952 [6], although it is most commonly known as the Scheil or Scheil-Gulliver equation, or the non-equilibrium lever rule.

This strategy will work both for Local Interface Equilibrium and for Local Metastable Interface Equilibrium, provided that the initial assumptions are applicable. The difference between equilibrium and metastable equilibrium is which phases are allowed to form. In the metastable case, solidification may be fast enough so that the most thermodynamically stable phase cannot nucleate. In such a condition, a new phase diagram must be determined, in which such phase is absent. If the Scheil equation is applied in the metastable diagram, it is therefore representing a Local Metastable Interface Equilibrium.

For some conditions, the analytical form of the Scheil equation will break down. These are cases in which k_0 depends on the composition, or when multiple phases are forming and a temperature invariant transformation is not taking place. In such conditions, the equations can be solved numerically. The numerical solution is based on the iterative solution of equation 4 for different f_S values. Starting at a small f_S value, C_S and C_L are calculated from the composition C_0 of the alloy. On the next iteration, f_S is changed, the previously calculated C_L is taken as the new C_0, k_0 is calculated for the new C_0 and the calculation is performed again.

At a first glance, the iterative process can be run simply by increasing f_S on each iteration. However, there are different ways of increasing the f_S value through iterations. On this work, many of the Scheil calculations presented were done using the software Thermo-Calc® [7]. In that software, iterations are performed by changing the temperature of the system. The algorithm is presented below:

1- The Liquidus temperature is determined for composition C_0

2- Temperature is reduced by ΔT, and the composition of the liquid phase (C_L) and solid phase(s) (C_S) are determined.

3- The molar fraction of the solid phase(s) is calculated as df_S. The fraction of solid f_S at any iteration is the sum of all calculated df_S values.

4- C_0 is taken as the calculated C_L.

5- Steps 2 to 4 are repeated until f_S reaches one.

Although this strategy seems convoluted if compared to simply incrementing f_S, it works better when the liquid is transforming on two solids at the same time, as equation 4 does not need to be applied for two different solid phases.

The initial development of the Scheil equation was based on a simplified case of unidimensional solidification, meaning it was applied for the directional solidification of a rod, in which the solid-liquid interface advances as a unified front. This would be equivalent to a planar solidification mode. The most common solidification modes across manufacturing processes are columnar dendritic, cellular dendritic and cellular [8].

However, the Scheil method can still be used for a cellular or dendritic structure if the solidification front is cylindrical.

One issue must be considered regarding the Scheil approach for microsegregation. The Scheil method would lose its validity if there was any diffusion in the solid or lack of complete mixing in the liquid. If one of the two conditions is false, the other can be assumed to be true, as the diffusivity of a solute in the liquid is typically 1000 times higher than in the solid. As such, if complete mixing is not present in the liquid, then diffusivity in the solid is negligible. If there is diffusion in the solid, then there is complete mixing in the liquid.

Other researchers developed segregation equations based on a mass balance approach similar to Scheil, but still taking into consideration the either diffusion in the solid or compositional profiles in the liquid. Two cases will be discussed on this text, the Brody-Flemings model for mushy zone microsegregation [9] which solid back-diffusion, and the Giovanola and Kurz [10] model for microsegregation under rapid solidification, which considers solute gradients in the liquid.

In the Brody-Flemings model, Fick’s first law of diffusion is used to correct the composition of the solid at the interface, changing the conditions for the mass balance equation. This yields a dependence on the length scale of the dendritic structure and the time scale through which solidification takes place. Compositions of the solid and liquid as a function of fraction of solid can be written as [11]:

$$C_L = C_0 \left(1 - \frac{f_S}{1 + k_0 Fo_S}\right)^{k_0 - 1} \quad \text{eq. 6}$$

$$C_S = C_0 k_0 \left(1 - \frac{f_S}{1 + k_0 Fo_S}\right)^{k_0 - 1} \quad \text{eq. 7}$$

Fo_S is a dimensionless term known as the solutal Fourier number, defined as

$$Fo_S = \frac{4 D_S t_f}{\lambda_2^2} \quad \text{eq. 8}$$

where D_S is the solute diffusivity in the solid, t_f is the time from beginning to end of solidification and L is the length scale through which solidification takes place. When $Fo_S k_0 \ll 1$, equations 6 and 7 reduce back to equations 4 and 5, as would be expected when solidification happens rapidly, when solid diffusivity is low or when the length scale is sufficiently large. We can evaluate the value of Fo_S for welding conditions by estimating t_f and L, and sourcing typical values of k_0 and D_S.

For most solutions, k_0 ranges from 10^{-1} to 10, although it will most commonly be less than one. We will take a typical k_0 to be 10^{-1}. We can consider substitutional solute diffusion to be negligible if $Fo_S k_0 < 0.01$, meaning it is negligible when $Fo_S < 0.1$.

Diffusivity data is scarce for temperatures close to solidification, but the order of magnitude of D_S does not change remarkably from solute to solute. As such, one specific case can be reasonably extended for other solutions. For analysis, we will take the tracer impurity diffusion coefficient of Ni in Fe γ at 1400°C, which is 6.6×10^{-14} m^2/s [12].

The typical cooling rate for welding processes ranges from 10^2 to 10^6 ºC/s [13]. For castings, this value can go from 10^{-2} to 10^3 [14]. Since the solidification temperature range for metal alloys typically has an order of magnitude of 10^2 K, this results in a t_f of 10^{-4} to 10^4 s.

λ_2 is the secondary dendrite arm spacing. This can vary widely from material to material and process to process, but generally ranges from 10^{-4} to 10^{-7} m.

Figure 4 shows the value of Fo_S calculated for these parameters. The gray region indicates the range in which $Fo_S > 0.1$. Generally, the length scale of the solidification structure is connected to the cooling rate. A few different empirical relations for the dendrite arm spacing of C steels [15], [16] and for Ni superalloys [17] as a function of cooling rate are shown. The expected conditions for the alloy analyzed in chapters 3 and 4 are also shown. As can be seen, the hypothesis of no substitutional solute diffusion is valid for most cases shown, valid for the two cases studied in this work and expected to only have an effect on large casting conditions.

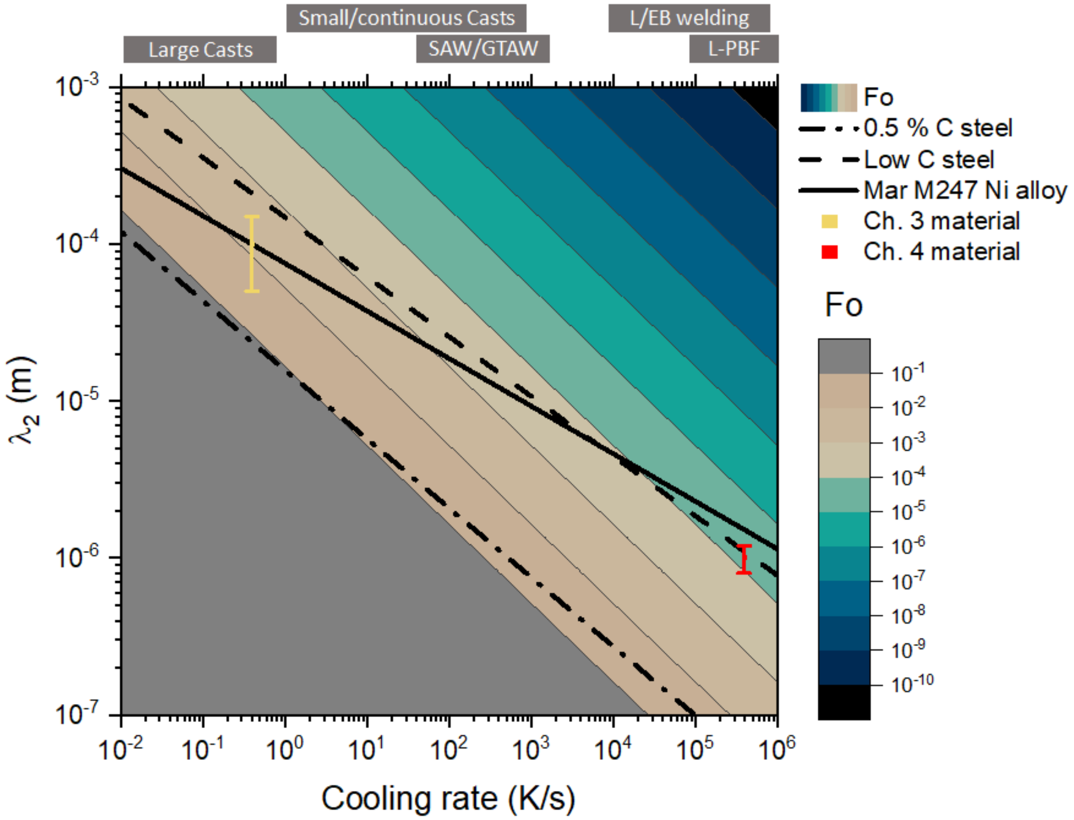

Figure 4: Fo_s map for cooling rates and secondary dendrite arm spacing values typically seen on alloy solidification. The grey region indicates the region where diffusion on the solid-state during solidification cannot be neglected. The cooling rate for different manufacturing processes is shown. The lines are based on empirical equations correlating cooling rate and secondary dendrite arm spacing for different materials. The estimated/measured conditions for materials studied on Chapters 3 and 4 are also shown.

These conclusions are valid for substitutional solute partitioning. The diffusivity of interstitial solute is orders of magnitude higher than substitutional solute. For such cases, back-diffusion on the solid is common, as is the case for C in steels. The Scheil equation can still be applied to successfully reproduce segregation profiles if a paraequilibrium model is used to construct the phase diagram in which the Scheil numerical method calculation is based [7].

Addressing compositional gradients in the liquid is much more complicated. This is due to the complex diffusion fields taking place near the dendrite tip. Nonetheless, compositional gradients in the liquid will influence the solid cell composition. The solute accumulation on the interface on the liquid side shifts the lever rule composition which defines the composition of the solid side. As the dendrite grows, more of the solute content partitions to either solid or liquid (depending on the value of k_0), shifting the composition of the solid away from any predictions made by the Scheil model.

Giovanola and Kurz addressed this issue by using a combination of models [10]. At the beginning of solidification, compositional gradients will be present at the interdendritic region. As cell cores grow, the diffusion fields in the liquid will eventually intersect, leading to a complete mixing region (Figure 5). Their strategy is to use a quadratic modelling approach for the region in which the liquid composition is transient and revert back to the Scheil equation when it becomes homogeneous. The point of reversion happens when the fraction of solid reaches f_x, or the point at which the liquid in the interdendritic or intercellular region is homogeneous (line 4 in Figure 5).

The composition of the solid at the interface is described as:

$$C_S = \frac{-a_2 + \left(a_2^2 + 4a_1(f_s - a_3)\right)^{\frac{1}{2}}}{2a_1}, \quad \text{for } 0 \le f_s \le f_x \qquad \text{eq. 9}$$

$$C_S = C_x k_0 \left(\frac{1 - f_S}{1 - f_x}\right)^{k_0 - 1}, \qquad \text{for } f_x < f_s \le 1 \qquad \text{eq. 10}$$

where C_x is the composition at the solid side of the solid-liquid interface when $f_S = f_x$, and a_1, a_2 and a_3 are semi empirical parameters. C_x, f_x, a_1, a_2 and a_3 are related by a system of five equations. Although they have physical significance, the parameters are independent from any solidification related characteristics, such as dendrite spacing or dendrite tip speed. Solving the system requires previous knowledge of the segregation structure, that is, a specific pair of C_S and f_S values.

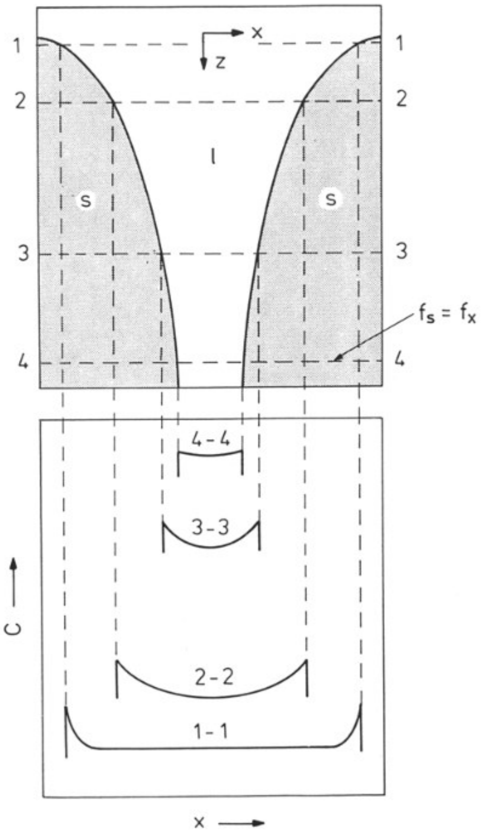

Figure 5: Schematic representation of cellular array. The bottom figure shows the transverse compositional gradients behind the tip. Adapted from [10].

This model has been successfully used to represent compositional profiles in solidification structures. However, it never experienced widespread usage due to its need for initial knowledge of the system being modelled. Most approaches for transient behavior on the liquid composition are based on numerical methods which solve the diffusion equations across a region representing the solidification structure. This must be done on a case by case scenario and can be computationally expensive. In chapter 4 for example, a comparison is made between the results from the Scheil model and a diffusion simulation performed in Thermo-Calc®. Other more sophisticated approaches include phase field and cellular automata models, which solve mass transfer and energy configuration of the system concomitantly [18]–[20]. These still are CalPhaD based, as the driving forces for diffusion are based on Gibbs free energies derived from the CalPhaD method, but do not necessarily consider a local equilibrium condition. These models are computationally expensive and seldom applied with more than two elements in the system.

Despite their differences all the models presented so far reflect the local stable or metastable equilibrium conditions described in Table 1. Non equilibrium solidification is common for extremely high cooling rates such as splat cooling, but otherwise it is a rare occurrence, not observed in welding or casting. However, for additive manufacturing, it can be a factor. Cooling rates in additive manufacturing can achieve 10^6 °C/s for Laser powder bed fusion depositions [21]. The departure from equilibrium can be understood by considering the speed at which the solid-liquid interface advances. If the interface is sufficiently fast, atoms which would normally partition to the liquid cannot diffuse from the interface sufficiently fast and are “trapped” in the incoming interface. Aziz proposed a relation to address this phenomenon by deriving an effective partition coefficient [22]:

$$k_v = \frac{k_0 + a_0 V/D_L}{1 + a_0 V/D_L} \qquad \text{eq. 11}$$

where V is the solid-liquid interface speed and a_0 is a typical interatomic spacing. k_v can then be used in an algorithm like the one used for Scheil to correct the C_S and C_L compositions determined at each iteration. Equation 8 shows that if V is sufficiently high, k_v goes to one, meaning that the solid will have the same composition as the liquid. If $V \rightarrow 0$, $k_v \rightarrow k_0$, representing an equilibrium or metastable equilibrium condition. It also shows that there will be a transition region between the two conditions.

Figure 6 a shows the composition of the cell tip as a function of fraction of solid for a Ni – 4.5%wt. Nb system. The diffusivity of Nb in the liquid was calculated as 5.037x10^9 m^2/s using Thermo-Calc® MOBNI4 database, and interatomic spacing was taken as 3.6 Å. As the interface speed increases, the composition at the dendrite tip departs from the equilibrium C_S value eventually reaching C_0 for speeds higher than 10^3 m/s.

For cellular or dendritic solidification, the maximum interface speed will be the scan speed of the laser. For additive manufacturing, the typical order of magnitude is 1 m/s. This determines a maximum value for the interface speed at the cell tip. The actual cell tip speed will be a projection of the scan speed on the direction of maximum thermal gradient, typically at an angle regarding the scan trajectory. As such, the interface speed can be estimated at around 10^{-1} m/s.

Figure 6 b is constructed by using k_v on each iteration of the Scheil algorithm by considering V constant. It shows that as the interface speed increases, the composition of the whole cell trends towards C_0. In actuality, this is not representative of a cellular solidification mode typically seen in additive manufacturing, as the interface speed would drop as the cell grows. Resolving this would require determining the local interface speed, which requires the solution of the local temperature and composition conditions at the interface. As such, it cannot be represented in a $C_S = f(f_S)$ type equation. Nonetheless this equation can be used to identify the dendrite tip composition. Figure 6 a shows that the effect of solute trapping would be negligible for the analyzed case in chapter 4 (0.6 m/s scan speed).

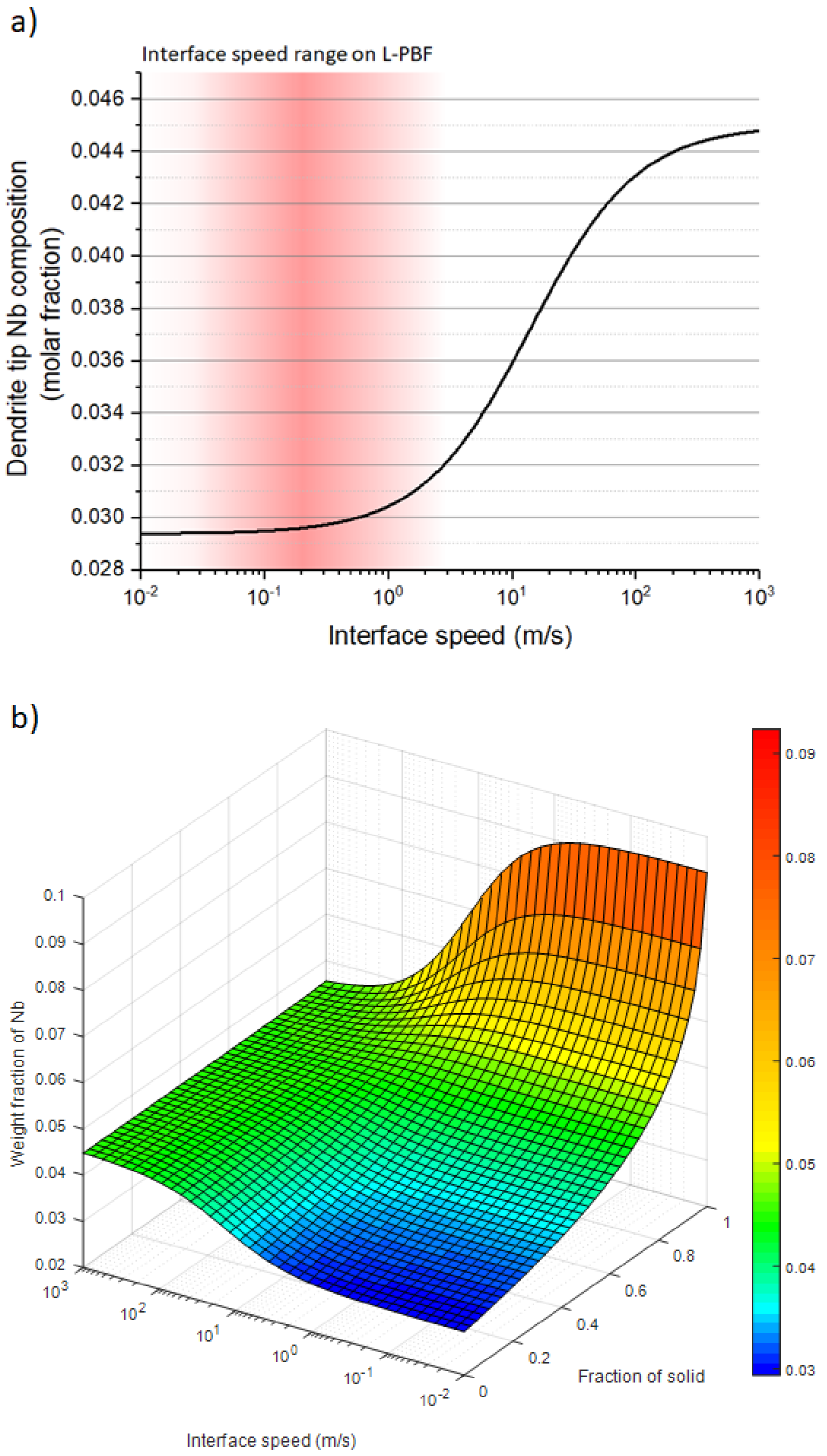

Figure 6: Effect of solute trapping on the composition of a cell as a function of interface speed based on equation 11. a) Composition at dendrite tip. b) Composition over the whole cell assuming fixed interface speed.

2.2.2. Phase transformations on the solid state

Two CalPhaD based strategies will be used in this work to model phase transformations in the solid state, both of them applied through the software Thermo-Calc®.

The first is based on solving mass flow through a simulated volume. The volume is represented as a unidimensional grid, where the solute content for an n-component system is resolved for each point of the grid at each time iteration by solving the diffusion equation in all points [23]:

$$J_k = -\sum_{j=1}^{n-1} D_{kj}^{n} \frac{\partial \mu_j}{\partial x} \qquad \text{eq. 12}$$

J_k is the diffusive flux of element k, D_{kj}^{n} is a (n-l)x(n-1) matrix of diffusivities and $\frac{\partial \mu_j}{\partial x}$ is the chemical potential gradient of element j. Although the model is unidimensional, symmetrical geometries can be represented through scaling factors on the grid allowing the simulation of planar, cylindrical and spherical diffusion fluxes. The diffusion model used can also resolve a two-phase problem by considering a moving interface between two phases. Once an interface is defined, a local equilibrium condition is enforced at the interface. This determines the boundary condition for solving eq. 12 adjacent to the interface. Diffusion is then solved inside each phase using eq. 12 and the new compositions of each grid point are calculated. Finally, the interface is moved to maintain mass balance between the two phases. This model was used in chapters 3 and 4.

The second model is a mean-field approach for precipitation. This is implemented in Thermo-Calc® and is based on the Kampmann-Wagner numerical approach to simulate concomitant nucleation, growth and coarsening of precipitates in a compositionally homogeneous matrix [24]. A combination of pre-established models is used to address homogeneous and heterogeneous nucleation, precipitate growth and coarsening.

This modelling approach cannot address a segregated matrix, but if the diffusion fields are sufficiently small, that is, if the diffusion distance is limited, different regions of a cell can be simulated independently.

2.3. A unified CalPhaD approach for solidification microstructure evolution

CalPhaD is established as an accurate approach to predict compositional partitioning, phase fractions, etc. When combined with other simulation techniques, it can provide composition dependent information which allow for the determination of microstructural morphology, local compositions, phase distributions, etc. However, modelling microstructural morphology is computationally expensive, and when applied through methods like phase field, the compositional scope must be limited.

The phase transformations taking place on the solid state will be severely affected by local composition, and since many can take place at the same time, it is important to understand how each and every element partitioned during solidification. As demonstrated in the previous section, the non-equilibrium lever rule, or Scheil method, can be used to understand how the composition at the solid side of the solid-liquid interface changes as the solid grows. This technique is computationally fast and readily applicable to multicomponent systems, as it only requires the determination of the system's phase diagram. If this composition is interpolated in a solidification morphology, e.g. a cylindrical cell or dendrite arm, the composition can be mapped onto the morphology. This approach would not be valid in a homogenous nucleation case, as the undercooling required for nucleation would change the equilibrium composition at the first layer of solid to form. However, in most manufacturing processes involving solidification, the solid phase either grows epitaxially or nucleation is heterogeneous [8]. In such cases, the undercooling required for nucleation can be neglected [25]. Afterwards, other techniques can be used to identify the solid-state phase transformation behavior. Both techniques presented in the previous section to evaluate solid state phase transformations are also computationally expensive, and require a compositional down-selection. However, once the solidification structure is known, this down selection can be done by considering which elements most affect the phase transformation or precipitation reaction being analyzed.

Hence, a modelling approach based on these techniques can be built as shown on Figure 7:

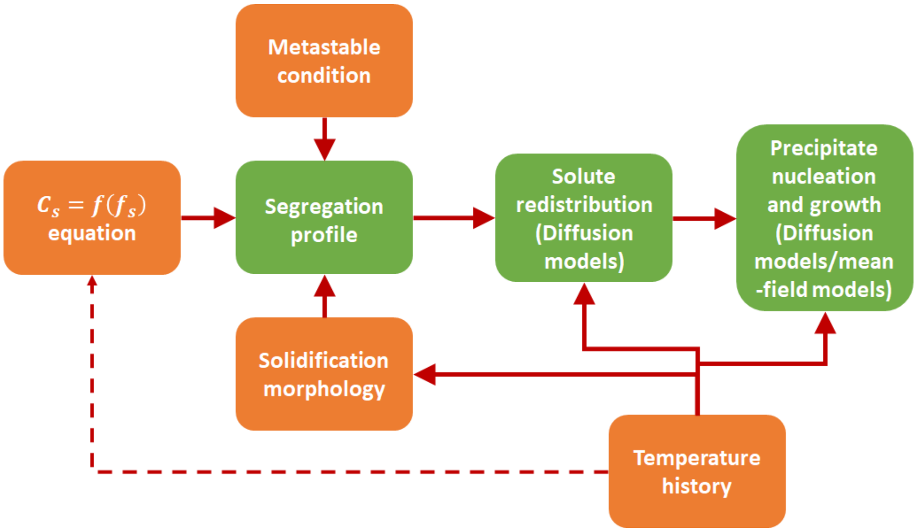

Figure 7: General sketch of the modelling approach being evaluated in this thesis. Green rectangles indicate the phenomena being evaluated. Orange rectangles indicate external information or models that must be chosen to evaluate the microstructure.

The orange rectangles on Figure 7 indicate external information that must be known to run the model.

- Metastable condition indicates the phases that would form during solidification. The phase selection will affect the construction of the phase diagram and differentiate between the entries 2 and 3 in Table 1.
- The $C_s = f(f_s)$ equation indicates the model used to correlate the composition of the growing solid with the fraction of solid in the system. This may be the Scheil equation, the Brody-Flemings model, etc.
- Solidification morphology indicates the solidification mode but also its length scale. This may be defined through empirical equations or through fundamental models.

- Temperature history is the most important aspect which must be defined. The main input derived from temperature history is the cooling rate. During solidification, it may be used to identify dendrite arm spacing through empirical models. At a solid-state condition, the cooling rate will affect the time available for a phase transformation to occur or for homogenization to take place. Other factors associated with thermal history, such as temperature gradient or solid-liquid interface speed, may be used to inform fundamental dendrite arm spacing models or the segregation model used. Temperature history may be determined by heat transfer models, by measurement, or even by estimation.

The green rectangles on Figure 7 indicate the phenomena being evaluated by the modelling approach.

- Segregation profile refers to the construction of a digital representation of the solidification microstructure. This includes the arrangement between the solidification matrix phase and solidification second phases, the length scale of the solidification microstructure, and the quantitative evaluation of how this segregation profile is distributed across the matrix phase.
- Solute redistribution refers to homogenization which may take place during cooling at solid state during solidification. This may also refer to solidification second phase growth or dissolution. The length scale for this phenomenon is the dendrite or cell size. As such, local behavior is not as important, and this is better addressed by the long-range diffusion models discussed in session 2.2.2.

- Precipitate nucleation and growth refers to precipitate formation across the segregated microstructure. The approach for this case is heavily dependent on the system being analyzed. Depending on the relation between diffusion distance and dendrite or cell length scale, precipitates may nucleate locally through the compositional profile of the cell, or nucleate at specific positions of the cell and growing by consuming the adjacent segregated solute. In the first case, it would be better addressed by a mean field model. In the second, it is better addressed by a long-range diffusion model. In the case where two separate precipitation reactions are happening concomitantly, the two models may be used at the same time.

2.4. Objectives

This modelling structure has the potential to address the motivation of this work. The sequential application of the models allows for considering the effect of the materials history on the evolution of the microstructure and uncover the different transformation pathways observed in alloys. Furthermore, the possibility of creating a single simulation engine that has all the information exchange between different modelling software built-in allows for quick digital prototyping of new alloy compositions and of untested heat treatment schedules. However, many of the aspects involved in the application of the CalPhaD based models are undefined. The goal of this work is to apply the modelling approach in different application cases, identifying the best strategies for the choice of models used to inform the simulations, and determination of how much characterization is necessary to inform the decisions made by the user in the application of the models.

The itemized objectives are listed below:

- Create a prototype of the modelling procedure shown on Figure 7. The prototype will include algorithms to read the information outputted by a software and conditioning this output for other software, capable of addressing other modelled phenomena.
- Apply the prototype in different simulation cases, focusing on different materials and different processes. Analyze how well the modelling approach addresses the simulation needs of the analyzed cases.
- Compare the modelling results with extensive characterization of the analyzed microstructures. Verify if modelling predictions are accurate.
- Identify the different sources of input information for the modelling approach and how sensitive model results are to variations in this input.
- Identify the developments necessary to turn the modelling approach prototype in a single application, capable of high throughput usage and readily applicable to different alloy systems and processes.

Chapter 3. Identification of Solidification Originated Microstructural Features and their Effect on Creep Properties on CSEF Steels

This chapter focuses on the application of the modelling approach in Grade 91 cast steels. This is an interesting application of the modelling procedure for several reasons:

- These steels undergo several different thermal processing steps at different temperatures;
- Despite the alloying content of each element being relatively low, the number of elements in the system is high, and the system must be simplified to model the behavior in the solid state. In some cases, this requires more than just element down-selection;
- The history of the analyzed parts is roughly ten years. For this reason, much of the information on how the steel was processed is lost. This means that the temperature and time evolution during processing must be estimated;
- The matrix phase undergoes massive transformations at several points during the processing history. As such, any signs of the solidification microstructure are lost.

The main goal of the studies presented on this chapter was to identify the characteristics of preferential creep cavity nucleation spots in the steel microstructure. Ultimately, these nucleation spots were found associated with solidification microstructure features.

Section 3.1 focuses on characterization of creep damage, and although some CalPhaD calculations are presented, it does not use the modelling approach. However, the characterization results are necessary to create a tie between the creep damage and the solidification microstructure.

Section 3.2 presents the first application of the modelling approach. It focuses on how the formation of a Cu phase is tied to the segregation profile coming from solidification. The solidification equilibrium condition assumed is Local Interface Equilibrium (entry 2 in Table 1). Some elements were removed from the solidification simulation due to lack of database information, but these elements are present in a small fraction and would have little effect on the overall solidification structure. The $C_s = f(f_s)$ equation used was the Scheil model, applied in a modified paraequilibrium phase diagram to consider C back diffusion in the solid. The temperature history was derived from heat treatment guides for Grade 91 steels and from typical cooling rate values for large steel casts. The solidification morphology considered was dendritic due to its prevalence in large steel casts, and the length scale of the dendritic structure was determined through an empiric equation.

3.1. Impurity content as a risk factor on the creep performance of CSEF steels – part 1: preferential creep cavitation on inclusions

This work was performed in collaboration with:

John Siefert[1], Jonatan Parker[1], Boian Alexandrov[2] and Antonio Ramirez[2]

1) Electric Power Research Institute.
2) Welding Engineering Program, Materials Science and Engineering Department, The Ohio State University

Guilherme Abreu Faria performed most of the characterization, and all of the analysis and modelling.

John Siefert and Jonatan Parker provided guidance, the automated SEM+EDS particle detection and the Laser Scanning Confocal Microscopy data.

Boian Alexandrov and Antonio Ramirez provided guidance.

KEY WORDS: CSEF steels, P91, Inclusion

Abstract

Grade 91 steels are creep strength enhanced ferritic steels strategic for the power generation industry given their unique combination of high temperature performance and cost benefit. However, this material has a track record of failures associated with reduced

creep performance at welded joints heat affected zone. Although many studies focus on metallurgical aspects, there is evidence that other characteristics, such as impurity level can affect these materials performance. In this study, we investigate the effect of inclusions on creep damage on three samples removed from failed Grade 91 components. Inclusions are shown to be correlated with cavity nucleation and shown to be a considerable detrimental aspect for creep performance in Grade 91 steels.

3.1.1. Introduction

Creep Strength Enhanced Ferritic (CSFE) steels are steels designed for high temperature applications. The high temperature strength on these materials is achieved through a carefully engineered microstructure, with a high density of subgrain boundaries and finely dispersed carbides. Grade 91 is a type of CSFE steel, developed as an improvement to other Cr and Mo bearing steels used in pressure vessels in several industries[26]. These steels are comprised of approximately 9% wt. Cr, 1% wt. in Mo and 0.1 % wt. in C, also bearing N and other secondary carbide formers such as Nb and V in smaller contents. The alloying additions and heat treatments required by code grant a ferritic or martensitic structure with high carbide content and solid solution strengthening, resulting in good creep properties and excellent resistance to high temperature service conditions. Grade 91 was proposed in the 70's[27] and adopted as an economical and technical solution to power plants working in the supercritical steam regime, at temperatures above 550 °C.

Since then, it has been widely applied in power plants given its unique creep properties and lower costs compared to other high temperature material solutions.

Most of the strengthening on Grade 91 steels comes from the formation of intragranular $M_{23}C_6$ carbides and MX carbonitrides, which stabilize the subgrain boundary network and prevent dislocation movement. In the lower part of the heat affected zone (HAZ), extensive research has indicated that recovery mechanisms associated with precipitate dissolution and coarsening can disrupt this dislocation and precipitate network, leading to diminished creep resistance and accelerated creep failure[28]–[31]. These regions are known as Type IV locations[32], where many of the failures in Grade 91 components are observed.

There is evidence that the performance of these materials is also associated with impurity element content. Although Grade 91 codes allow some presence of impurities, there is evidence that increased control is necessary to prevent premature creep failure. Previous studies have shown that several impurity elements can have detrimental effects on creep properties[33]. Of particular note are the effects of S and Al. Experiments show that there is a correlation between S content and time to failure, meaning, increasing the S amount decreases the time to failure. The effect of Al has been studied mostly regarding its ratio with N. This is due to the high propensity for formation of AlN when such elements are present. In heats with high Al:N ratio, most of the N is consumed in the formation of AlN, impairing the formation of beneficial MX carbonitrides. Essentially, materials with high Al:N ratios present low resistance to tempering and therefore, reduced creep strength[34].

Recently, two coal based power plants, the Aberthaw[35], [36] and Rugeley[37] power plants in the United Kingdom, experienced premature failures in service in key components pertaining to the steam transport infrastructure. These components were headers designed for carrying steam from the boilers to turbines. Failure was present in the stub to header welds of the components and while they were expected to last for 150000 hours, damage was noted prematurely at a third of this time in Aberthaw and half of it in Rugeley. Both components were manufactured from Grade 91 steels, and further characterization indicated that the poor creep properties of the materials were the likely cause of failure.

Extensive characterization and research have shown that these components undergone similar processing and working conditions, undergoing proper heat treatments, welding procedures and later being exposed to similar temperatures and loads. However, the materials with poor performance had one key difference if compared with one with satisfying creep behavior, they had a much higher impurity and tramp element content. A number of failures have been reported for Grade 91 components, but despite the fact that the root cause of several of these failures can be attributed to improperly conducted materials processing, a number of materials produced to specifications still present poor performance. There is an increasing understanding that this loss in creep resistance and ductility is associated with chemical composition, particularly the impurity level[33].

In this work, we analyze the creep cavity distribution and cavity surroundings in three samples removed from the two components. The analysis aims at understanding if local microstructural features, particularly, the presence of inclusions, can be behind the premature failure.

3.1.2. Experimental

Materials Analyzed

In total, three samples were used for comparative analysis. All samples used in this project were removed from failed components from two power plants in the UK. Two samples were removed from the Aberthaw plant component, namely B2 and TP1, and one from the Rugeley plant component, namely H1. Although the two samples removed from Aberthaw came from the same component, they were removed from parts coming from different material heats.

Failure was always observed in the heat affected zone of stub to header welds. Heat treatments and welding procedure were consistent in all components. Operation temperatures were similar, and damage was noted in both power plants in similar time scales. In addition, the components were removed from service at similar times. Table 2 summarizes the thermal history and operation conditions of all three components. Additionally, this table shows the main alloying composition, and a few of the alloying elements or impurities that are discrepant across the samples.

Table 2: Summary of operation conditions and discrepant composition in the three samples.

		Aberthaw		**Rugeley**
		B2	TP1	H1
Weld procedure		GTAW root GMAW fill	GTAW root GMAW fill	GTAW root GMAW fill
PWHT		~760°C/2hours	~760°C/2hours	~760°C/2hours
Work Temperature and Load		~570°C/ ~80MPa	~570°C/ ~80MPa	~585°C/ ~80MPa
Damage noted/component replaced		50k hours/ 85k hours	50k hours/ 85k hours	84k hours/ 94k hours
Major alloying elements (wt. %)	Cr	8.77	8.33	8.88
	Mo	0.94	0.94	0.93
	C	0.10	0.10	0.08
	V	0.21	0.21	0.21
	Nb	0.071	0.070	0.061
Micro alloying and impurity Level (wt. %)	Al	0.040	0.020	0.034
	S	0.010	0.002	0.009
	Cu	0.19	0.05	0.18
	As	0.0128	0.0042	0.0136
	Sn	0.0080	0.0030	0.0083
	Sb	0.0023	0.00063	0.0019
	Pb	0.00075	0.00003	0.00062

As reported on [33], the base material removed from the Aberthaw components were used to produce creep samples. Creep tests indicated that the B2 heat presented very little creep ductility if compared with the TP1 heat.

Stubs were joined to the headers through circumferential welds with the circumference being coaxial with the stubs. The welds were sectioned in a plane perpendicular to the weld direction (Figure 8).

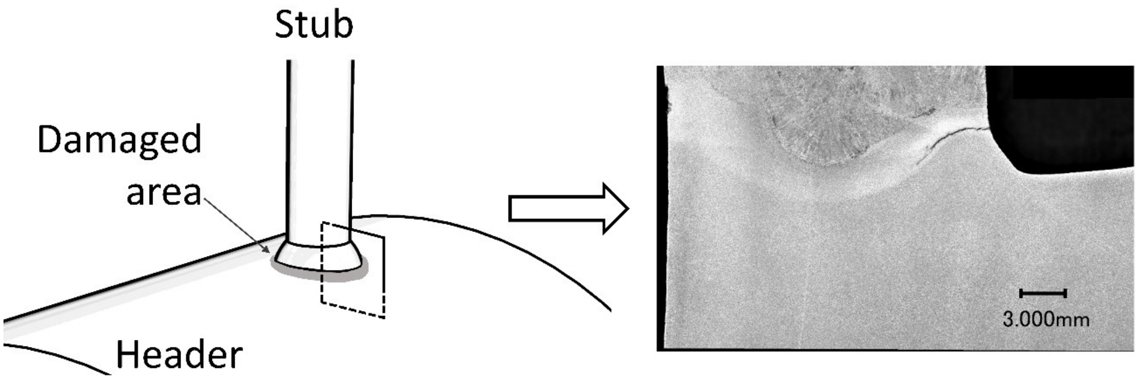

Figure 8: Schematic of the portion of the components from which the samples were removed. The micrograph shows the etched microstructure of sample H1.

All samples presented creep cavities along the heat affected zone (HAZ). For the Confocal Laser Scanning Microscopy (CSLM) and Scanning Electron Microscopy (SEM) measurements, the surface of the samples was polished down to colloidal silica. No etching was used.

Damage analysis

Creep failure is normally associated with the transition from secondary to tertiary stage creep. On this transition, the material starts to present creep cavities. The extent of creep damage in a material can be understood by observing the density and distribution of cavities. To identify the extent of damage in all samples, the surface of the samples was imaged using CSLM. Measurements were set so there was a clear contrast between matrix and cavities, with a resolution of 670 nm/pixel. The images formed a grid covering the entire region on the samples where cavities were observed. The images taken from each sample were analyzed using the particle detection feature in software ImageJ. In total, 11980 cavities were identified in B2, 6263 cavities in TP1 and 43651 in

H1. To cut out improper identification of image speck, only cavities with an area larger than 3.6 μm^2 were considered.

Inclusion and second phase analysis

One potential difference that may arise from the different compositions in the three analyzed samples are the second phases and inclusions present in the phases. Two strategies were used to analyze what these potential phases may be, CalPhaD and automated particle measurements in an SEM.

Given the long time the material spent at service temperature, it is expected that it will be at or close to the predicted equilibrium state at such temperature. Besides calculating the phase distribution at service temperature, thermodynamic calculations were carried out to understand the phases present in the alloys, their stability with temperature and the different solvus temperatures in the different alloys. The phase diagram calculations were all based on the CalPhaD method using the software Thermo-Calc®. All calculations were performed using the TCFE9 database from Thermo-Calc®. In general, thermodynamic calculations had to be restrained to a limited composition, to guarantee both coverage in the database as well as an increased chance of convergence. The elements used were Fe, Al, Cr, Cu, Mn, Mo, Nb, V, Si, C, S, O and N. The phases considered for the phase diagram calculation were Fcc, Bcc, Liquid, Laves, Sigma, MnS, M23C6, AlN and Spinel (Al2O3/MgO).

The inclusion analysis through SEM were performed in an automated microscope using a Tungsten source with 20 keV beam energy. Measurements were performed on sections of base material extracted from the three components and covered an area of 51.468 mm^2. Particle recognition analysis was performed with a threshold from 1 μm to 228 μm. Once an inclusion is identified, the nature of the inclusion is determined through EDS, with a measurement time from 1 to 2 s. A total of 7293 inclusions were found on B2 (141.7 inclusions/mm^2), 916 in TP1 (17.8 inclusions/mm^2) and 6672 on H1 (129.63 inclusions/mm^2). Depending on composition, the inclusions were classified under one of the following phases: MnS, Alumina, Spinel, which contains high presence of Al, Mg and Ca, and AlMnS. Many of the observed inclusions were unclassified.

Cavity neighborhood analysis

SEM measurements were performed with a FEI/Philips XL-30 Field Emission ESEM. This equipment was used to perform backscattered electron imaging and energy dispersive X-ray spectroscopy (XEDS). Imaging focused on cavities. In most observations, cavities were associated with a number of second phases (Figure 9). Backscattered electrons were used as the optimal imaging mode due to the atomic number contrast which is achievable at low electron beam energies.

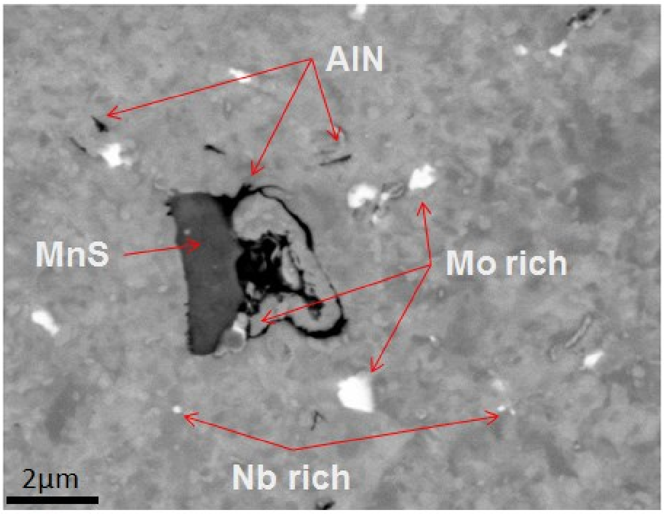

Figure 9: 7keV Backscattered electron image in B2. Typical second phases observed in the cavity environment are shown.

Despite the fact that such images allow for a good morphology characterization, from these alone it is not possible to differentiate between Mo and Nb rich particles, or between S and Al rich inclusions. X-ray energy dispersive spectroscopy mapping was used to identify the compositional distributions across the sample. These results were combined with CalPhaD calculations to identify which phases should be present in the matrix structure.

A total of 36 cavities per sample were analyzed through EDS mapping. Maps were taken with a 0.05 µm step size with a beam energy of 10 keV. This energy was chosen to guarantee a high spatial resolution. As such, element quantification was based on L edges for the transition metals considered.

The neighborhood of the cavities was also analyzed through EBSD measurements. These measurements were taken with a 0.03 µm step size, also with a beam energy of 10 keV.

3.1.3. Results and discussion

Damage analysis results

Figure 10 a shows maps of the cavity densities measured across all samples. The maps were taken in a rectangular grid following the heat affected zone in the three analyzed joints. The densities shown were calculated by averaging the number of cavities in 250 µm wide squares. Figure 10 b shows the outline of the rectangular regions shown on Figure 10 a.

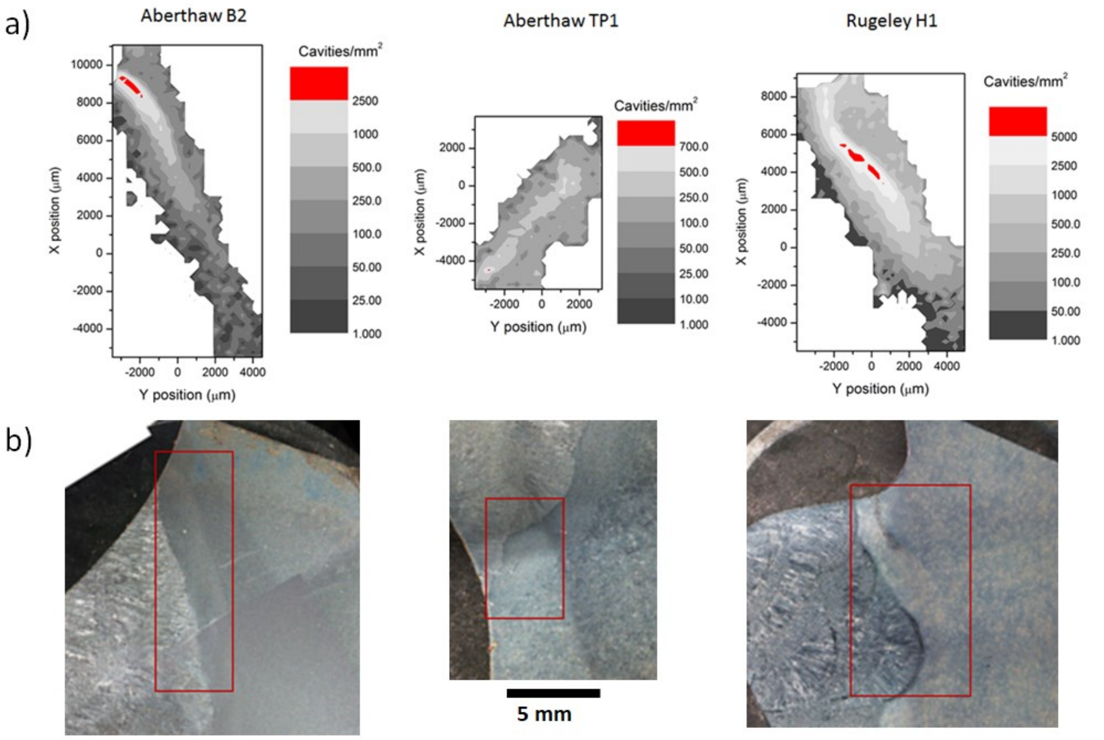

Figure 10: a) Cavity density map for the three analyzed materials. Density was evaluated in 250x250 μm^2 regions. b) The red squares indicate the regions mapped in each sample.

The cavity densities on the B2 and H1 heats are much higher than what is observed for TP1. The maximum density observed for H1 is around 5000 cavities per mm^2, for B2 it is 2500 cavities per mm^2 and for TP1 it is 700 cavities per mm^2. In all samples, cavity density is spread through a straight line along the HAZ, parallel to the fusion zone. However, in B2 and H1 there is a damage concentration point, presumably indicating the onset of a crack. In fact, the region above the peak density in H1 contains a crack formed by coalescence of cavities, which was not considered in the cavity count, hence the lower density in that region. In all samples, damage seems to concentrate around the intercritical, and fine-grained heat affected zones (ICHAZ and FGHAZ)

The areas of cavities in all samples were also evaluated. Figure 11 shows cavity area histograms for the three samples. Despite the differences in total cavity count across the samples, TP1 area distribution skews towards larger areas while H1 and B2 are centered towards lower areas. B2 and H1 are richer in smaller voids compared to TP1. The mode for B2 and H1 is at 20 µm^2 while it is lower at 10 µm^2 for TP1. However, the distribution quickly drops for higher areas in B2 and H1 while for TP1 the distribution remains roughly constant (albeit falling), even reaching a higher number of cavities than B2 for areas larger than 60 µm^2. H1 always show a higher number for all areas, but this sample does show a much larger cavity count. This indicates that the B2 and H1 materials have a higher propensity for cavity nucleation than TP1, while having less driving force for cavity growth.

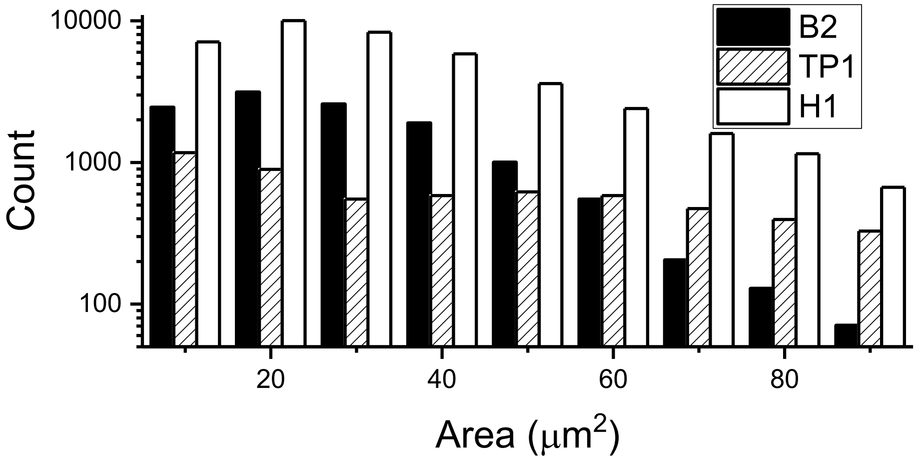

Figure 11: Area histogram for observed cavities in the three samples.

Inclusion and second phase results

The phase distribution in the alloys was calculated as a function of temperature from 1700°C to room temperature. Figure 12 shows the molar fractions in thermodynamic equilibrium versus temperature for the H1 sample. Several phases are expected to be present at the work temperature. These include Al_2O_3, MnS, MX carbonitrides, AlN and Laves. Within the discussion of this work, focus is directed at the previously mentioned phases. σ and α' phase becomes stable at temperatures below the service temperature. These phases are not expected to form given their low formation kinetics. A Cu rich FCC phase is also predicted close to the service temperature. This phase will be discussed on part 2 of this work.

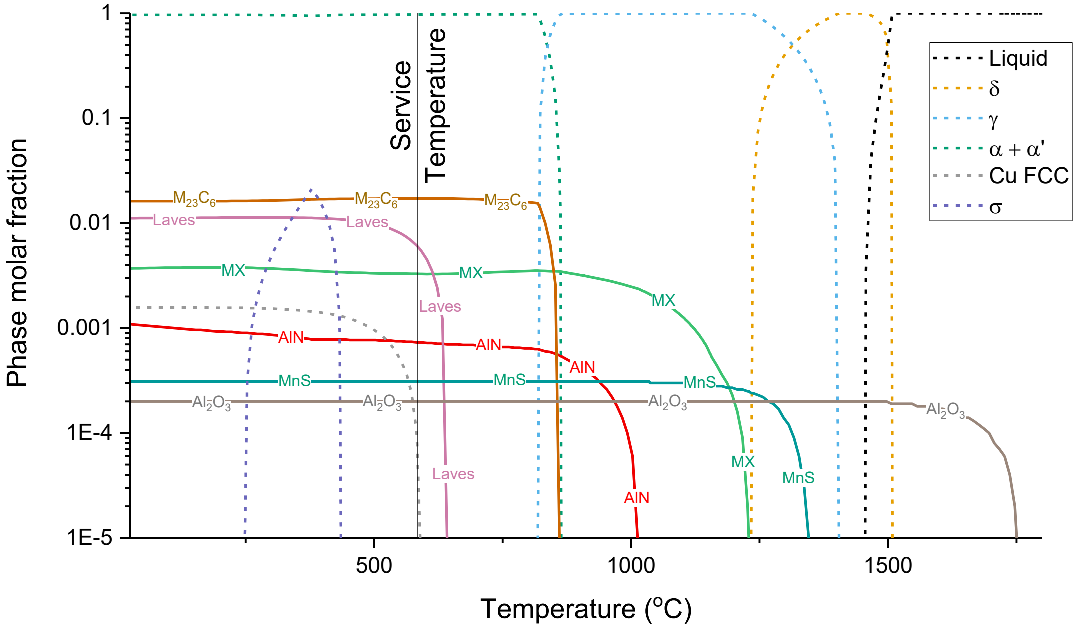

Figure 12: Property diagram for the Rugeley H1 sample. The diagram shows the molar fraction of the phases studied against temperature in Celsius. The temperatures at which phase transformations and precipitation reactions happen can be seen. Vertical scale from 0 to 0.005.

Based on the calculations, it is possible to construct Table 3, with the phases present at the service temperature, their molar and volume fractions and atomic fraction compositions. The data presented on the table was calculated at 570°C for the Aberthaw samples and 585°C for the Rugeley sample.

Table 3: Phase information for the phases present at the service temperature for all samples.

Phases	Molar fraction			Volume fraction			Composition (at. frc.)
	B2	TP1	H1	B2	TP1	H1	
BCC (matrix)	0.98	0.98	0.99	0.98	0.98	0.98	-
$M_{23}C_6$	0.02119	0.019	0.0172	0.01909	0.02	0.01545	0.6Cr 0.09Mo 0.07Fe
MX	3.16E-03	3.46E-03	3.28E-03	2.59E-03	2.60E-03	2.66E-03	0.4V 0.08Nb 0.4N 0.1C
Laves	5.97E-03	0.00536	5.96E-03	6.67E-03	0.00602	6.63E-03	0.33Mo 0.46Fe 0.2Cr
Al_2O_3	1.70E-04	5.11E-05	2.00E-04	1.70E-04	1.40E-04	2.00E-04	Al2O3
MnS	3.40E-04	5.43E-05	3.10E-04	3.40E-04	6.80E-05	3.00E-04	MnS
AlN	10.6E-4	7.00E-04	7.30E-04	9.20E-04	6.10E-04	6.40E-04	AlN

A few observations can be taken from this table. Firstly, MnS and Al_2O_3 contents are significantly higher on B2 and H1, with values around five times higher than TP1. Most of the observed phases have the same composition and volume fraction at the service and room temperatures. This is an indication that the particles and precipitates observed at room temperature during the characterization procedures are representative of their state at the service temperature.

The automated SEM analysis focused on detecting primarily inclusions. The densities of these inclusions are shown on Figure 13, as well as the fraction of observed inclusions for each sample. As can be seen on the figure, B2 and H1 show a much higher inclusion density than TP1, reaching an order of magnitude higher value. Also, the most common inclusions are MnS and Alumina. There is still a high number of unclassified inclusions, which is particularly high for H1. However, parsing through the data, 89% of the unclassified particles in B2 contain Mn and S, albeit not in the expected stoichiometry. This number reaches 85% on H1. Therefore, most of the unclassified particles in H1 and B2 are expected to contain some MnS. The analyses performed also show average sizes for the particles. These numbers are shown in Table 5.

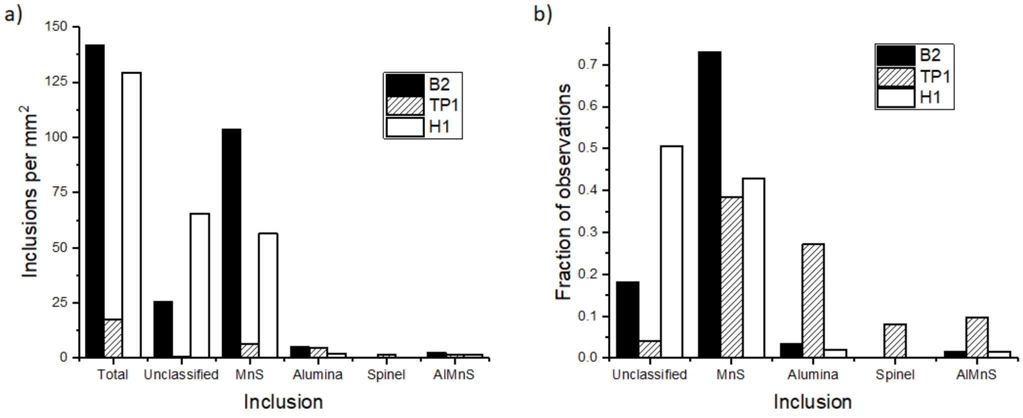

Figure 13: a) Inclusion densities detected by the inclusion analysis performed by SEM+EDS automated detection. b) Fraction of observations for all inclusion phases for all samples.

Cavity neighborhood analysis

The damage concentration around cavities was evaluated through EBSD mapping. These measurements were only performed in samples B2 and H1, the two samples that presented higher damage. Measurements concentrated at regions adjacent to the highest damage region. In B2, the grain structure (Figure 14 b and d) is comprised of refined grains with few, larger grains scattered throughout, potentially indicating a ferritic/martensitic structure typical of the ICHAZ or of regions of the FGHAZ in which a diffusive γ→α can be observed during cooling, as described by reference [26] for grade 91steels. In H1, the microstructure presents larger grains with a more homogeneous size distribution (Figure 14 a and c). In both cases there was no indication of preferential nucleation sites for cavities in the grain structure itself. Cavities were observed adjacent to larger grains, but also on the middle of refined grain regions.

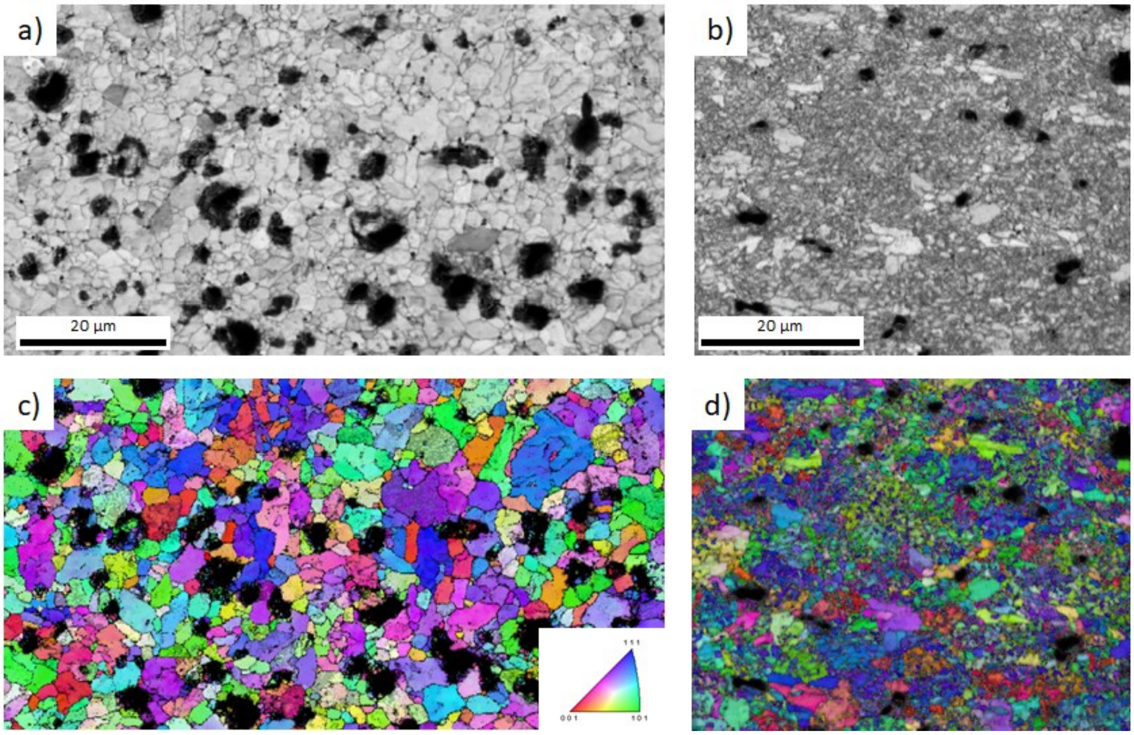

Figure 14: Image quality map on H1 (a) and B2 (b) samples. Orientation maps for the same region in H1 (c) and B2 (d). Orientation is plotted regarding the surface normal.

In the majority of cavities analyzed throughout this project, second phases were present interfacing the cavity itself, as shown on Figure 9. In some cases, the second phases were easily identifiable through their composition, such as MnS and Al_2O_3+MgO spinel. In others, such as AlN or Nb rich MX carbonitrides, the phases were identified through its rich solute content and respective morphologies. One of the most common observations were Mo rich globular particles. Based on the CalPhaD results, these would be Laves particles. Another common observation was Al rich needle like particles, identified as AlN. All second phases observed were categorized as one of the following phases: AlN, $M_{23}C_6$, NbC, MnS, Al_2O_3, Al_2O_3+MgO spinel and SiO_2. Other phases which have been previously identified in the literature[33], [38] as being detrimental to creep properties such as Z phase, BN or Ni and Sb intermetallic phase were not observed. The number of observations of each phase at the cavity interface plus a morphology and size description for each second phase are shown on Table 4. The size and morphology evaluations are based on any observation of the particle within the measured region. For some second phases, such as $M_{23}C_6$, no particle was observed in the interface of a cavity, despite the fact that several $M_{23}C_6$ particles were identified.

Table 4: Size and morphology of the particles observed. The number of particles associated with a cavity for each phase is also shown.

		MnS	Al_2O_3	Al_2O_3/ MgO	SiO_2	Laves	NbC	AlN	$M_{23}C_6$
Size (μm)	B2	0.82 ± 0.49	1.92 ± 0.84	-	-	0.33 ± 0.13	-	0.30 ± 0.13	≤0.2
	TP1	1.04 ± 0.59	1.00	2.50 ± 0.82	-	0.62 ± 0.47	0.66 ± 0.43	-	≤0.2
	H1	1.26 ± 0.60	1.22 ± 0.34	1.17± 0.24	3 x 2	0.34 ± 0.12	0.22 ± 0.16	0.25	≤0.2
Inclusion/second phase Morphology		Globular	Spherical	Spherical	Polyhedral	Globular	Spherical	Needle	Spherical
Distribution*	B2	14	6	0	0	25	17	2	0
	TP1	18	9	3	0	14	0	10	0
	H1	18	9	3	1	25	17	2	0
**Total number of cavities measured per sample is 36*									

The majority of cavities interface with some second phase. The most common phases in such observations were Laves, MnS, Aluminum rich oxides, AlN and Nb rich MX carbonitrides. Previous studies in CSEF steel components removed from service have also identified Laves particles adjacent to creep voids[39], and suggest that such particles were detrimental to creep behavior. Laves phase forms at the expense of $M_{23}C_6$ carbides[40], and as such, may have a detrimental effect similar to AlN, in which it reduces the density of beneficial carbides. Nonetheless, Laves, AlN and MX carbonitrides are densely dispersed across the microstructure. Figure 15 shows a backscattered electron image taken from the microstructure of the damaged region in sample B2. Some instances of such phases are pointed by arrows, and their high occurrence can be seen. Therefore, there is a high probability that either a cavity nucleation spot would be adjacent to one of such phases or that the cavity would grow into it.

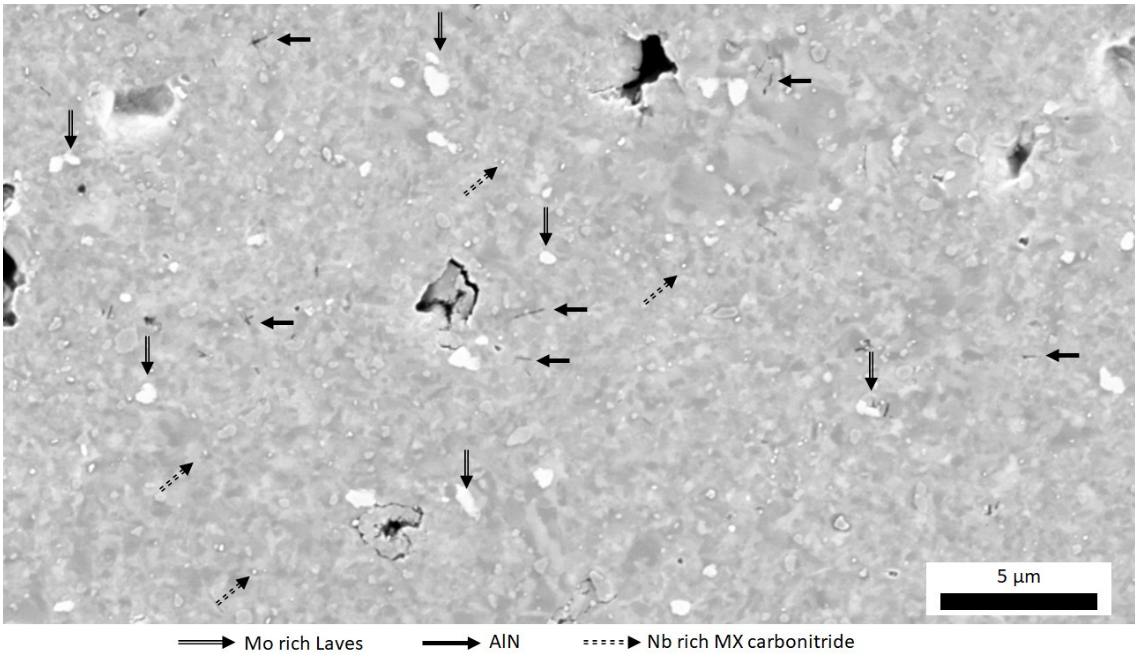

Figure 15: Backscattered SEM image of sample B2. The areas indicate various second phases present in the microstructure.

As for the MnS and Al oxide inclusions, these are much less dense across the microstructure, and it is remarkable that many of the cavities are found in association with these inclusions. Figure 16 shows the percentage of observed cavities associated with both types of inclusions.

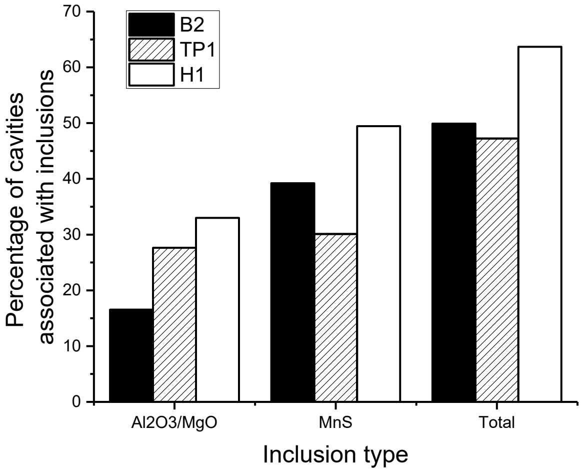

Figure 16: Percentage of observed cavities associated with higher risk phases/unwanted phases.

Between 50% and 65% of the observed cavities are associated with an inclusion. Considering that we observed the cross section of cavities, these numbers are likely higher in the bulk material than in the sectioned plane. This indicates a larger risk for cavity formation around such inclusions than on the rest of the microstructure. It is also important to note that the percentage of association is consistent across all samples, meaning that the cavity formation mechanism around the inclusions is similar. Additionally, as shown by Figure 10, TP1 presents lower cavitation density than B2 and H1, while also presenting lower inclusion levels, as shown in Figure 13 and Table 3. The consistent association of cavities and inclusions as well as the correlation between higher inclusion density and higher cavity density implies a mechanism through which low creep resistance is tied to higher inclusion content.

Cavity and inclusion density comparison

Despite the high association with cavities and inclusions, it is important to compare the densities of both instances across the microstructure to understand if the inclusions are the actual source of the high cavity densities in H1 and B2 as compared to TP1. If inclusion density is much smaller than cavity density, then another microstructural feature must be responsible for cavity nucleation. If it is much higher, than the association may be coincidental, as was the case for Laves, AlN and MX phases. As described in the previous session, inclusion densities were determined through a SEM based inclusion detection method. However, the inclusion analysis was performed with a lower threshold of 1 μm for the inclusions, and as shown on Table 4, the average size of inclusions observed through EDS mapping is around this value. Some inclusions may have been neglected on the analysis resulting on lower values for density from the inclusion analysis. To get additional inclusion density values through an alternate method, the inclusion volume fractions predicted by CalPhaD and the average particle sizes determined through EDS mapping were combined. Each particle was assumed to have a spherical shape with a diameter with the same value as the ones reported on Table 4. Using the volume fraction reported on Table 3, the number of cavities in a rectangular prism volume of 1x1 mm with a height equal to the diameter of a particle was calculated. That way, the resulting volume density is equivalent to the area density of inclusions. The volume fractions derived from CalPhaD assume an equilibrium condition, which is not necessarily true for the materials analyzed. However, both MnS and Aluminum oxides are formed on liquid during the material manufacturing, and due to the high temperature at the moment of formation of these inclusions, they can be expected to be at an equilibrium condition. Additionally, given the lack of morphology precision on EDS maps, the calculated numbers are susceptible to large errors, but the order of magnitude of the calculations are expected to be accurate. These values are reported on Table 5, along with the density values retrieved from automated SEM inclusion analysis.

Table 5: Volume fraction, average sizes and particle densities determined by CalPhaD combined with EDS mapping and by the automated SEM and EDS analysis. The table also includes maximum and average cavity densities.

	Phase	Volume fraction ($x10^{-4}$)			Avg. particle size in µm			Particle density* /mm^2		
		B2	TP1	H1	B2	TP1	H1	B2	TP1	H1
Thermodynamic + EDS maps	Al_2O_3/ MgO	1.7	1.4	2.0	1.50 ±0.5	1.1	1.1 ±0.4	82	33	231
	MnS	3.4	0.68	3	0.7±0.4	0.8 ±0.4	1.2 ±0.6	749	85	257
	Total							831	118	488
Automated Inclusion Analysis	Al_2O_3	0.55	0.38	0.91	3.4	2.8	6.1	4.9	4.9	2.7
	MnS	2.47	0.10	8.6	1.6	1.3	3.8	103.8	6.9	56.5
	Total							141.7	17.8	129.63
Cavity dist.	Top Cavity density							~2500	~700	~5000
	Average cavity density over analyzed region							221	176	551

*For the thermodynamics and EDS maps analyses, particle density was determined based on the volume fraction calculated and by assuming that each particle had a diameter as reported in Table 4. The matrix volume considered was a 1 x 1 mm prism with the thickness of the particle.

Table 5 shows a discrepancy between expected density from thermodynamic and EDS map data and the automated inclusion analysis. This discrepancy can be explained through the shortcomings of both analysis methods. The CalPhaD combined with EDS mapping methodology is based on few observations, which reduces their statistical significance if compared to the inclusion analysis. Additionally, the consideration of a single average value for the inclusions rather than a distribution including larger diameters skews the calculated density towards larger values, over predicting the density calculations. As for the automated inclusion analysis, the minimum diameter threshold in the analysis ignores smaller inclusions. Many of the unclassified inclusions also show Mn and S in their composition, although these were not considered for the density evaluation. Therefore, this methodology under predicts the density value. As such, the actual inclusion density on the analyzed samples is expected to be between the reported values from the two methodologies. Nonetheless, both approaches have the same trend regarding different samples and different inclusions.

Save for a few cases, the trend in inclusion density determined through both approaches in the three samples reflect the trend in cavity densities in these samples. While B2 has the higher inclusion density, H1 has the higher cavity density. However, H1 was under service for longer in a higher temperature and was submitted to higher strain.

The maximum cavity density in all samples is roughly one order of magnitude higher than the inclusion density in all samples. Comparing average cavity densities across samples can be a source of error given that the mapped regions are not necessarily comparable in terms of applied strain, especially given the inhomogeneity of cavity distributions. Still, the average cavity densities on the damaged area has the same order of magnitude as the inclusion densities. There is a larger difference in the case of TP1, but as can be seen on Figure 10, the cavity distribution on this sample is quite different from that observed on B2 and H1.

Overall, there is a match between cavity and inclusion densities in all samples. This behavior would not be expected if the density of other phases such as AlN or $M_{23}C_6$ were considered, given the much higher density of these phases in the matrix.

3.1.4. Conclusion

There have been many studies researching the loss of creep properties in the heat affected zone of Grade 91 steels. These studies often concentrate in loss of creep strength due to metallurgical reactions such as carbide coarsening and lath recovery in the HAZ. However, other studies have shown that other compositional parameters, particularly impurity and micro alloying element levels also affect creep behavior. As mentioned before, this is evidenced by the difference in creep behavior between B2, H1 and TP1. Based on the studies presented in this work, a mechanism through which this is happening is proposed. To build an argument for such mechanism, some of the conclusions arising from the different characterization approaches are discussed.

From the macro damage distribution section, a clear relationship between poor creep ductility and high cavity density exists. It is also shown that the materials with lower ductility present cavities of lower size, indicating that in the poor ductility materials plastic deformation is creating more cavities rather them growing preexisting ones. The density measurements indicate that although the strongest cavitation region is concentrated in H1 and B2, cavitation happens throughout a large region of the heat affected zone in all samples. This distribution is also wide, encompassing a large range in the heat affected zone, and damage is not confined in any specific zone, such as the fine grained or intercritical HAZ. Essentially, that means that cavity nucleation and growth in the analyzed case is mostly independent of the matrix microstructure.

This argument is reinforced by the EBSD measurements. These show that there is no indication of damage accumulation around specific grain arrangements. If the matrix microstructure of H1 and B2 are compared, these show quite different microstructure, with H1 showing large grain sizes and a ferritic morphology, and B2 showing a martensitic ferritic dual phase microstructure. However, the damage extent on these phases is similar.

If the cavities are correlated with second phases, a clear trend arises. Most of the cavities in all samples are associated with some second phase, with only approximately 10% of cavities not associated with any phase. If the fact that the cavities are sectioned is considered, this is even more remarkable, given that the observed cavities not associated with a second phase could be just a hemisphere of a cavity which is associated. The second phases include inclusions, but also AlN, NbC and Laves. The later ones are densely scattered through the microstructure and the most common morphology association of the cavity with a phase indicates that most of the cavity surface is not in contact with the phase particle itself. In most of these cases it is possible that the cavity grew into a second phase particle. If these phases are ignored, what remains is that most of the cavities, up to 60%, are associated with inclusions. These inclusions are specifically MnS and Al and Mg oxides. At no point NiSn or BN phases were found, so even though these are noted high risk phases for cavity nucleation, they are not the source of poor creep performance in these materials.

One interesting observation is that the percentage of cavities associated with a particular inclusion is roughly the same in all samples. If the inclusion density is calculated or measured in the samples, the estimated values always follow a similar trend. B2 has the higher inclusion density, followed closely by H1. TP1 has the lower inclusion density, much lower than the two previous samples. As for cavity density, a similar trend follows, TP1 has the lowest density, B2 has a much higher density, and is followed closely by H1. Given that inclusion and cavity densities are comparable and that the number of cavities associated with inclusions is roughly the same in all samples, it follows that the inclusions are preferential cavity nucleation sites and are behind the differences in cavity density and damage extent in the samples.

By collecting these points, the failure on these materials can be explained as follows. Through the creep life of the components, the microstructure experiences constant plastic deformation. This leads to strain accumulation at interfaces. In regions near the interfaces between the matrix and inclusions, the strain energy accumulation required to open a cavity is reduced, and cavities start opening at much lower strains. This can happen either by the nucleation of a cavity in the interface between two phases or through accumulated damage in the pliable inclusions. This leads to an early transition from stage 2 to stage 3 creep, resulting in premature failure. A smaller inclusion content would still lead to cavity nucleation at earlier stages if compared with an inclusion free material, but if the cavity density is sufficiently low, this transition would be slower resulting in a longer service life.

One issue with this description is that it is based on inclusion densities in the whole material, and therefore, applies to the whole material, whereas the damage is clearly concentrated in the heat affected zone. Several mechanisms can reduce creep performance and creep strength in the heat affected zone. During service, this region would experience larger deformations under the same load if compared to the base metal. This would increase strain energy accumulation in the interfaces if compared with the rest of the material, and the onset of cavitation would happen at lower times in the HAZ, explaining why strain is accumulated in this region. Consequently, the poor creep performance in these materials is given by a concomitant effect of creep susceptible microstructure and abundance of susceptible cavity nucleation spots, arising from the high impurity level and inclusion densities.

3.2. Impurity content as a risk factor on the creep performance of CSEF steels – part 2: Cu concentration around impurities

This work was performed in collaboration with:

John Siefert[1], Jonatan Parker[1], Camilo Fernandes Salvador[2], Joao Oliveira[3] and Boian Alexandrov[4]

1) Electric Power Research Institute
2) Institute of Physics, University of Sao Paulo
3) Department of Mechanical and Industrial Engineering, New University of Lisbon
4) Welding Engineering Program, Materials Science and Engineering Department, The Ohio State University

Guilherme Abreu Faria performed most of the characterization, and all of the analysis and modelling.

Camilo F. Salvador and Joao Oliveira provided the TEM foil production and TEM measurements

John Siefert, Jonatan Parker, Boian Alexandrov and Antonio Ramirez provided guidance.

KEY WORDS: CSEF steels, P91, Impurity content, Creep cavitation

Abstract

This work focuses on three different Grade 91 materials coming from failed components in power plants. Except for small compositional differences, the three analyzed materials had the same processing history and service condition. However, one of the materials present a much higher creep ductility. Previously, creep cavitation on these materials was associated with the presence of inclusions. In this work, a Cu rich phase is observed around inclusion particles which are associated with creep cavities. The Cu phase was only observed around two of the materials, and both had a lower creep ductility. A mechanism for the formation of this Cu phase is proposed and verified through thermodynamically modelling Cu segregation during casting, Cu diffusion during processing history and Cu phase growth during the service condition.

3.2.1. Introduction

The drive for the use of supercritical steam in power plants has pushed for an increase in operational temperatures. At such temperatures, creep damage on the steels used in the power plant construction becomes an issue. Creep strength enhanced ferritic (CSEF) steels are widely used in power plant components for their superior creep properties up to 600 ºC. These properties are originated by a refined tempered martensitic microstructure with finely dispersed carbides[41]. Grade 91 is a CSEF steel with 9% wt. Cr and 1% wt. Mo with additions of secondary carbide forming elements such as Nb or V. Although it was initially developed for nuclear power plant applications in the 1970's[42], it has been largely adopted by the fossil fuel power generation industry.

When grade 91 materials fail during service, this often happens through type IV cracking, meaning cracking occurring through the inter-critical and small grained heat affected zone (HAZ) [43]. In part 1 of this paper, three materials removed from failed components were analyzed. Creep damage on the samples was concentrated in the HAZ and was ultimately correlated with the inclusion densities in the materials. Of the three materials analyzed, the one with a smaller inclusion concentration had a higher creep performance, particularly, higher creep ductility. Another important aspect that differentiates these samples is the concentration of Cu on the alloy compositions. The Cu content in the higher performance sample was approximately four times smaller than in the other two. Cu presence in Grade 91 has been shown to reduce creep time to failure [44], [45], and a stricter upper limit of 0.1% wt. Cu has been suggested for improving the general performance of P91 steels [33]. Additionally, the rupture life of Cu doped heats is shown to be independent of Cu content. It has been suggested that the effect of Cu comes from stabilization of a Cu rich FCC phase at high temperatures.

In this work, a series of observations of such Cu phase are reported, specifically in association with inclusion particles. The Cu FCC phase appears as an interlayer between inclusion and matrix. A mechanism for the formation of this phase is proposed and verified through thermodynamic modelling of the relevant homogenization and phase transformation behavior.

3.2.2. Experimental Method

Samples

In total, three samples were used for comparative analysis. All samples used in this work were removed from failed components from two power plants in the UK [35], [37]. The alloying compositions of the three samples were derived from ICP, IGF and Combustion measurements, and are shown on Table 6.

Table 6: Chemical compositions of the samples analyzed in this work.

Sample	**Elements (weight %)**						
	Al	B	Cr	Cu	Mn	Mo	Nb
B2	0.04	0.0015	8.77	0.19	0.41	0.94	0.071
TP1	0.02	0.005	8.30	0.05	0.40	0.94	0.070
RH1	0.034	<0.001	8.88	0.18	0.41	0.93	0.061
Sample	Elements (weight %)						
	Ni	P	Si	Sn	Ti	V	Zr
B2	0.12	0.009	0.41	0.008	<0.002	0.21	<0.002
TP1	0.19	0.012	0.33	0.003	<0.002	0.21	<0.002
RH1	0.14	0.012	0.14	0.0083	0.002	0.21	<0.002
Sample	Elements (weight %)						
	As	Pb	Sb	C	S	O	N
B2	0.0128	0.00075	0.0023	0.10	0.01	0.003	0.0454
TP1	0.0042	0.00003	0.00063	0.10	0.002	0.0024	0.0424
RH1	0.0136	0.0006	0.0019	0.08	0.009	0.0035	0.0447

Failure was always observed in the heat affected zone of stub to header welds. Heat treatments and welding procedure were consistent in all components. Operation temperatures, damage development and removal from service was similar in all components. Additional information can be found in part 1 of this work.

Characterization

Samples were sectioned perpendicular to the weld direction and metallographically prepared for characterization. No etchant was used. Characterization of cavities was done by combining backscattered imaging and Energy dispersive spectroscopy mapping.

SEM measurements were performed with a FEI/Philips XL-30 Field Emission ESEM. A total of 36 cavities per sample were analyzed through EDS mapping. Maps were taken with a 0.05 μm step size with a beam energy of 10 keV. This energy was chosen to guarantee a high spatial resolution. As such, element quantification was based on L edges for the transition metals considered.

On the Aberthaw B2 sample, a focused ion beam microscope was used to produce a foil by sectioning an under-surface cavity. TEM data was collected using a FEI TF-20 Tecnai 200 kV TEM in HAADF mode. All electron microscopy characterization was performed at the Center for Electron Microscopy and Analysis at the Ohio State University.

Thermodynamic calculations

The CalPhaD method was used to investigate the phase transformation behavior in the samples. Phase diagrams, Scheil-Gulliver [7] solidification calculations and diffusion with interface mobility models [23] were used to simulate the material. Fe-Cu pseudo binary phase diagrams were produced based on the Aberthaw B2 sample composition. In general, thermodynamic calculations had to be restrained to a limited composition, to guarantee both coverage in the database as well as an increased chance of convergence.

Phase diagrams were based on Fe, Al Cr, Cu, Mn, Mo, Nb, Si, C, S, O and N. For the Scheil-Gulliver simulations, O was removed, whereas for diffusion simulations, Fe and Cu were always used, and when the treatment temperature was above the $M_{23}C_6$ carbide solvus, Cr, Mo and C were added.

The goal of thermodynamic modelling was to investigate the effect of the multiple heat treatments on the initially segregated cast microstructure. As will be shown on the results section, the Scheil model showed a strong Cu solute partition which indicates that there was enrichment of Cu in the solidification grain boundaries. Grade 91 steels typically follow the following processing steps:

1. Forging at 1200°C for 1h
2. Homogenization at 1100°C for 30min
3. Tempering treatment at 760°C for 2h
4. Welding
5. Post Weld Heat Treatment at 760°C for 2h

The Diffusion simulations had a temperature evolution designed to emulate this history. Cooling and heating were also included throughout the simulation due to the fact that mobility is higher in the bcc phase and this would be the matrix phase below A_1. However, it was not possible to simulate the transformations from austenite to ferrite and from ferrite to austenite at each step due to simulation instability. Observing these transformations was not the goal of the simulation and given the fast time frame in which these happen, they are not expected to change the compositional profiles. Also, as will be shown on the results section, Cu was highly undersaturated in both ferrite and austenite phases at the transformation temperatures, so no major driving forces for Cu mobility in these temperatures is expected. Therefore, the transformation temperature interval was cut from the simulation. During cooling and heating the system was simulated with a BCC phase at temperatures below A_1 and with an FCC matrix above A_3.

Since the goal of the simulation was to observe the effect of the temperature history in the compositional profile, the size of the system was assumed to be half of the secondary dendrite arm spacing of a solidification microstructure. The system was constructed as a unidimensional compositional profile with cylindrical symmetry. The compositional profile from the Scheil calculation was taken as the compositional profile of the system where 0% solid corresponded to the outer edge of the system and 100% solid corresponded with its center. After a step was completed, the compositional profile of that step was used as the initial profile of the next step. Heating and cooling rates were assumed as 1°C/s, which is reasonable for air cooling in such a large component. In the case of the weld a higher cooling rate of 10 °C/s was applied given the locality of the heating. In actuality, the component is expected to have a higher temperature change rate at higher temperatures and a lower rate at lower temperatures. However, since mobility is higher at elevated temperatures, this is still a conservative projection and the element mobility seen in the simulations is expected to be higher than reality. Cr, C and Mo were used in the system in addition to Fe and Cu in all steps where carbides were not present. In the tempering and PWHT step, C supersaturation should lead to carbide precipitation, however, simulating this phenomenon was not possible in the software since it leads to divergence, and therefore C was removed. In the service condition, the presence of Cr and Mo lead to similar issues, so these elements were also removed. The carbide formation does not involve Cu and it is impossible to simulate it concomitantly to Cu diffusion. If the precipitates are not formed, the matrix would be supersaturated and the solvus temperature and driving forces for Cu precipitation would not be representative of the actual system. In the service condition, the system only contained Fe and Cu, but driving forces were representative of the thermodynamic calculation predictions for the actual alloy. Additional information on how this was achieved can be found on the supporting materials.

The system followed the temperature profile shown on Figure 17.

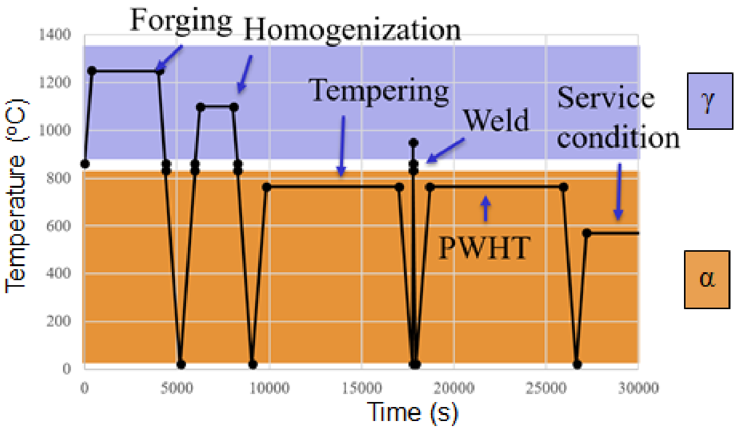

Figure 17: Time-temperature sequence used in the simulations for the Cu shell morphology.

3.2.3. Results

Characterization

As discussed in part one, creep cavities were often associated with inclusion phases. In many of such phases, a Cu rich region was found around the inclusion. Such regions were always seen around Al2O3 and MnS particles. Figure 18 shows some of these observations. The Cu rich region is seen either on top or surrounding the inclusions. It is interesting to note that no Cu rich regions were found in the TP1 sample. When Cu was found by itself, it had a small spherical morphology with a size of roughly 100 nm. Cu not associated with an inclusion was never found associated with a cavity.

Figure 19 shows the distribution of inclusions in measured cavities and how many of them were associated with a Cu layer. Most inclusion particles in the B2 and H1 samples which were associated with cavities also had Cu surrounding it.

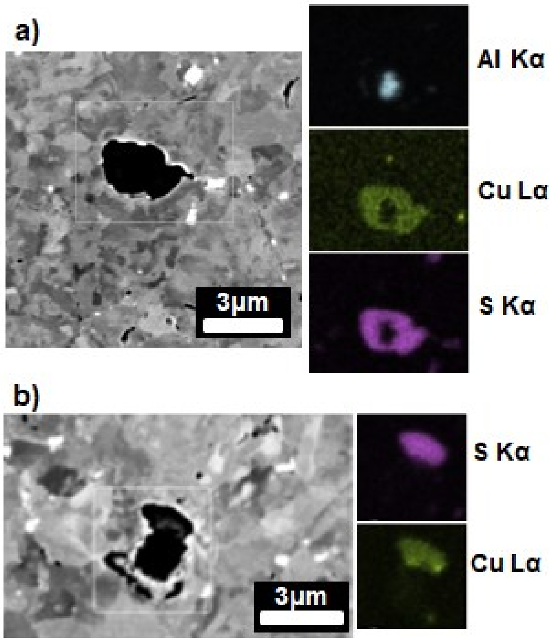

Figure 18: Backscattered electron Images and EDS maps from observed cavities, both made with 10 keV and displayed on the same scale. Figure (a) was obtained from the B2 sample, and Figure (b) from the H1 sample.

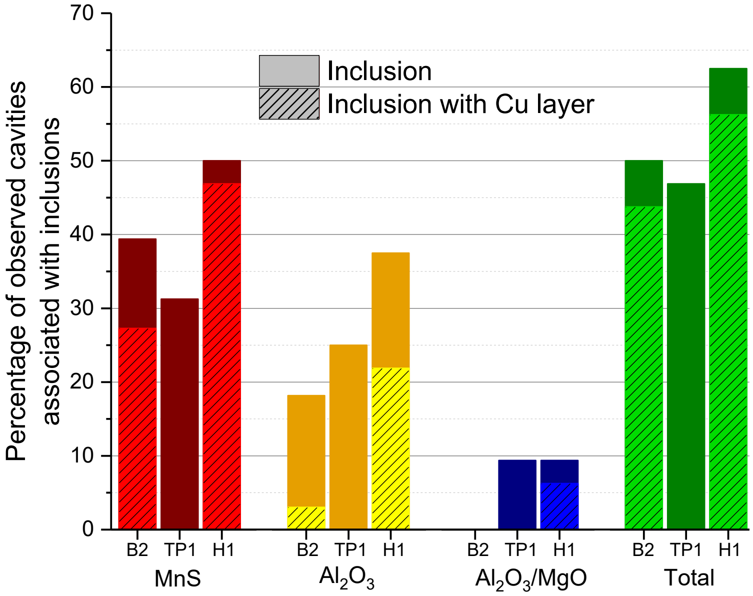

Figure 19: percentage of cavities associated with inclusions. Both the total number of inclusions and number of inclusions containing Cu layers are shown.

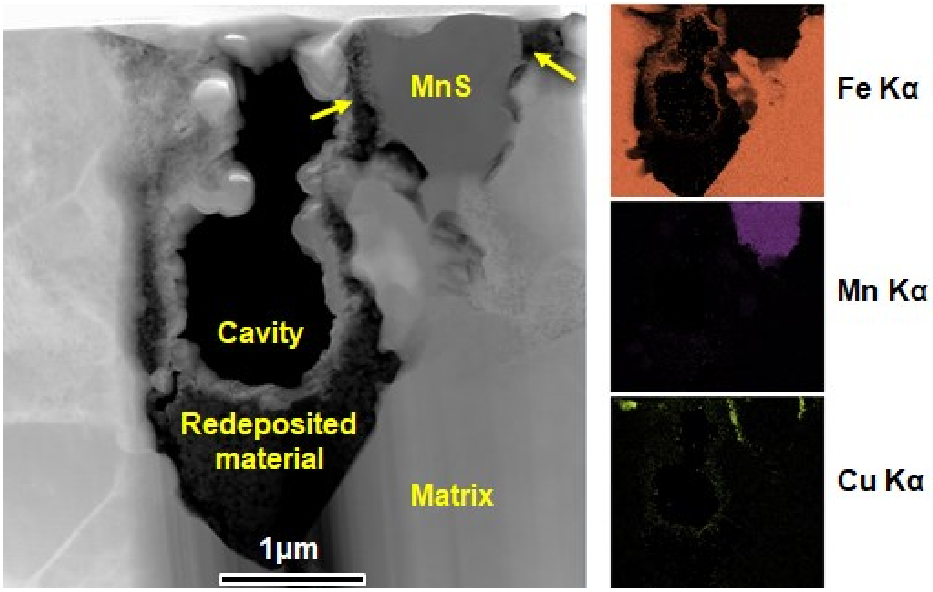

Figure 20: FIB foil obtained from a plane intersecting a cavity. The insets show the spectroscopy signals obtained for Fe, Mn and Cu. The Cu rich areas around the MnS particle are indicated by arrows.

Figure 20 shows the foil obtained from the B2 sample. The cavity can be seen at the center, lined with redeposited material originated from the trenching process in the FIB. The EDS map obtained from the foil shows a MnS inclusion neighboring the cavity. Cu enrichment is shown around the MnS particle, particularly at the interface between the inclusion and cavity. This suggests that Cu is initially present as a layer between the inclusion and matrix. Additionally, the superimposed presence of Cu in the S rich regions on Figure 18 is likely due to Cu presence around the MnS particle rather than a mixture of Cu, Mn and S, and the reason behind the superimposing signals is the penetration depth of the electron beam.

Thermodynamic simulations

Figure 21 shows a pseudo binary Fe-Cu phase diagram made with the composition of the B2 sample. The blue line shows the solvus boundary for a Cu rich disordered FCC phase. Pseudo-binary diagrams made with the TP1 and H1 compositions have the Cu rich phase solvus line in the same position. The points shown on the diagram indicate the Cu composition for the three materials and their respective service temperatures. This indicates that a Cu FCC phase would be stable at service temperature for the H1 and B2 components, but not for the TP1 component.

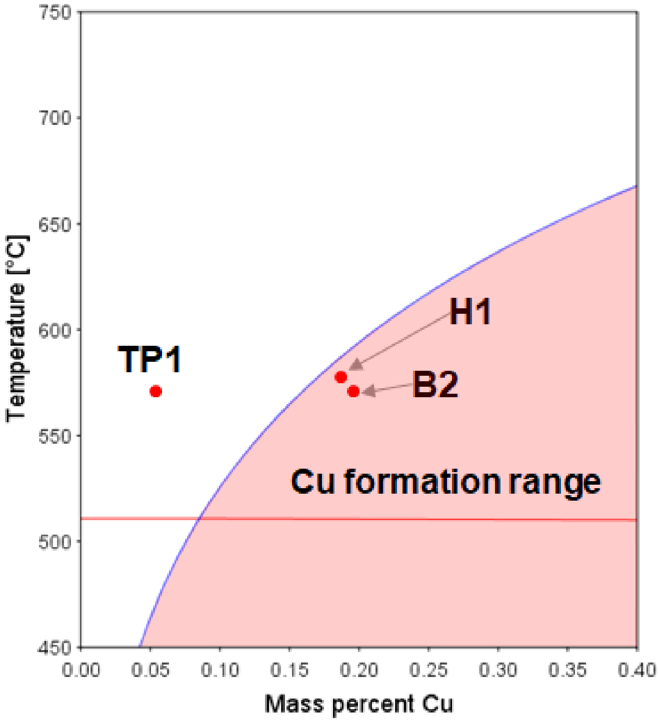

Figure 21: Pseudo binary Fe-Cu phase diagram for the B2 sample composition. The Cu FCC phase formation region is shaded in red. The white region represents Fe α. The Cu content vs service temperature for the three samples are indicated.

During the processing history of P91 components, these steels are subjected to several heat treatments on temperatures above the solvus for the Cu rich phase. In an attempt to understand how the Cu layer was formed on the B2 and H1 components, a mobility simulation was prepared to understand the phase growth with time. Based on the density of cavities and their association with inclusions, it is reasonable to assume a distance of around 200 µm between cavities surrounded by the Cu. A simulation was set with a spherical geometry, with equally spaced 100 cells. The simulation was performed with some undercooling to compensate for the differences between the simplified Fe-Cu system and the actual alloy. The determination of the undercooling is done on the supporting materials section.

Initial attempts at running the simulations used a homogeneous composition along the system, having a value equivalent to that of H1 or B2. However, in these simulations, nucleation never occurred, even after setting the nucleation energy barrier to a low value of 10^{-8} J/mol. Attempts were also made in adding an active Cu FCC embryo, but the resulting embryo would eventually dissolve back in the matrix. Therefore, even though the systems are below the solvus line for Cu rich FCC, simulations indicate that this phase wouldn't form. This is probably because random walk diffusion driving force (points towards homogeneous composition) is higher than chemical potential driving force (points toward uphill diffusion). The random walk diffusion is driven by an increase in the system entropy whereas the chemical potential driving force is driven by the precipitation reaction enthalpy. It is likely that under these conditions, even though the

FCC phase is stable, random walk diffusion is preventing the atomic movement necessary to grow the FCC phase.

This indicates that, if the supersaturation is increased locally beyond a certain point, the driving force for atomic movement towards an embryo would compensate random walk movement, and the embryo would grow. Therefore, if the matrix carried any spatial variation in Cu concentration, richer areas would be the nucleation spots for Cu rich FCC. Cu has a high solidification partitioning coefficient in Fe, and a possible mechanism for this compositional variation would be the segregation profile arising during solidification. To determine how this segregation would take place, Scheil simulations were undertook with the three materials. The compositions used are shown on Table 6. The model assumed C and N as fast diffusers and did not allow α→γ transformation during cooling. The simulations show that for all samples solidification takes place mainly as ferrite, with some formation of austenite and MnS at the end of solidification. It was not possible to include O in the calculations due to lack of database information, and therefore it was not possible to include Alumina or Spinel as possible phases. Figure 22 shows the phase mass fraction for all phases as a function of temperature. All alloys form a small amount ranging from 0.7-2 mass percent of austenite after the material is mostly solidified as ferrite. They also form a small amount of MnS at the end of solidification, with roughly 0.01 mass % in B2 and H1 and 0.001 mass % on TP1.

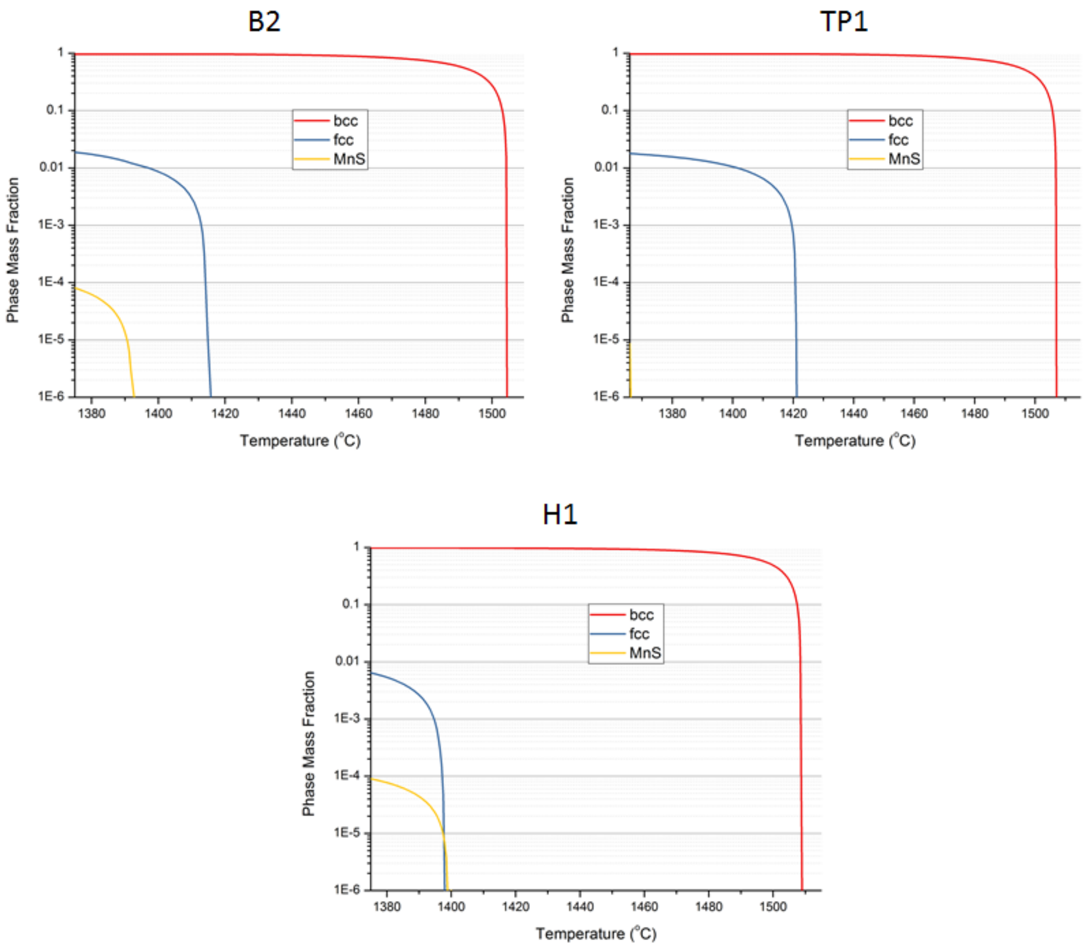

Figure 22. Phase mass fraction as a function of temperature for the three materials as predicted by the Scheil calculations.

The Scheil calculations also show the high segregation happening for Cu. The last region to be solidified can reach up to 0.33 wt. % on H1, 0.375 wt. % on B2, and 0.12 wt.% on TP1. The Cu fraction on a solidified layer is shown as a function of solid mass fraction for the three materials on Figure 23.

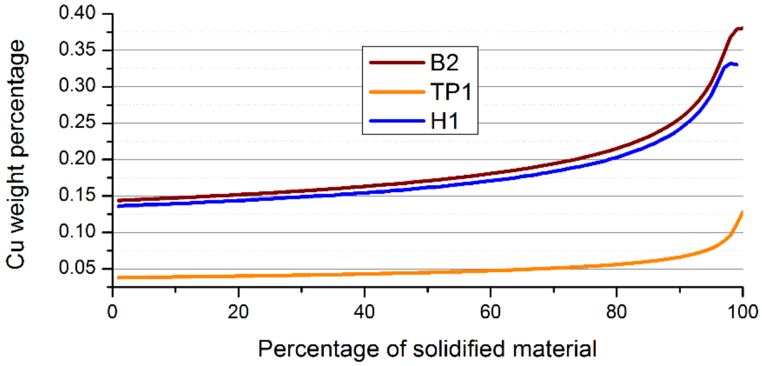

Figure 23: Cu weight fraction content for a solid layer formed when a certain mass percentage of the whole material was solidified. Values were calculated using a Scheil-Guliver model with increased mobility for C and N, and are shown for the three analyzed materials.

These indicate that there is a severe compositional variation on the solidified matrix. If this compositional variation remains until service temperature, a considerable fraction of the matrix on B2 and H1 would be highly supersaturated. The supersaturated region would be adjacent to the MnS particles formed at the end of solidification and possibly to other inclusions formed on the liquid, such as Al_2O_3 and MgO. However, the materials undergo a complex temperature history before service, and it is necessary to check if the segregation profile would not be erased through the different processing steps. In order to do this, the compositional profile observed on the Scheil calculations has to be transferred to the diffusion module on Thermo-Calc®. The strategy followed to achieve this was to assume a columnar dendritic solidification structure, given the high likelihood that this was the structure on the cast.

Such a solidification structure will carry two different segregation mechanisms, one on a micro level, and one on a macro level. The Scheil model is readily applied on the micro level, given its assumption of complete mixing in the liquid and no mixing in the solid. Therefore, this compositional profile is readily applied to the compositional variation on secondary dendrite arms within a dendritic solidification structure. The edges of the dendrites will have higher Cu content, and the vertex between dendrites will be the most Cu rich region. To properly set the Diffusion model, the secondary dendrite arm spacing must be known. Reference [46] reports a functional equation that relates the size of secondary dendrite arm spacing with the cooling rate in low alloy steels with 0.1 to 0.9 %wt. of C. This relationship is originally based on reference [16]. The reported equation is:

$$\lambda = 148\left(\dot{T}\right)^{-0.38} \qquad \text{eq. 13}$$

where λ is the secondary arm spacing and $\dot{T}$ is the cooling rate. Reference [46] also reports the cooling rates for typical casting procedures. The values reported range from 10^{-5} °C/s in large castings 10^{3} °C/s in small, continuous and die castings. These define a very large cooling rate range, and defining a value for the components analyzed cannot be done precisely. In terms of size, these components match the description of large castings. Some Grade 91 components are made from continuous casting processes but these are normally restricted to smaller sizes than the components analyzed here [27]. If the equation is applied to the lower limit of larger castings, 10^{-2} °C/s, the yielded spacing is 850 μm, however, this cooling rate is outside of the range of data originally studied in reference [16] and may result in a different solidification morphology. Also, with such a low cooling rate, the hypothesis of no solid diffusion on the Scheil equation is not valid.

Since the region being studied is closer to the surface of the part, it is reasonable to assume that locally it had a higher cooling rate. A 0.5 °C/s rate results in a secondary dendritic arm spacing of 200 μm, 2 °C/s rate results in a spacing of 100 μm and 20 °C/s rate results in 50 μm. For the comparison between the samples, a spacing of 100 μm was chosen to reflect an average behavior between the different possibilities.

The diffusion model was set as a cylindrical model with its center coinciding with the middle point between secondary dendrites. The size of the model was set so that its radius matched half of the secondary dendrite arm spacing. The segregation predicted by the Scheil model was interpolated to convert the data from solid fraction to distance from the middle point, with 100% solid coinciding with the zero position, the center of the model. This approach is illustrated in Figure 24. In the way the model is set up, there would be variations on composition at different angles around the cylinder axis. Although these variations can be estimated, they cannot be implemented on the model, as the diffusion module necessarily simulates mathematically unidimensional systems, although it represents a two dimensional one by applying symmetry conditions.

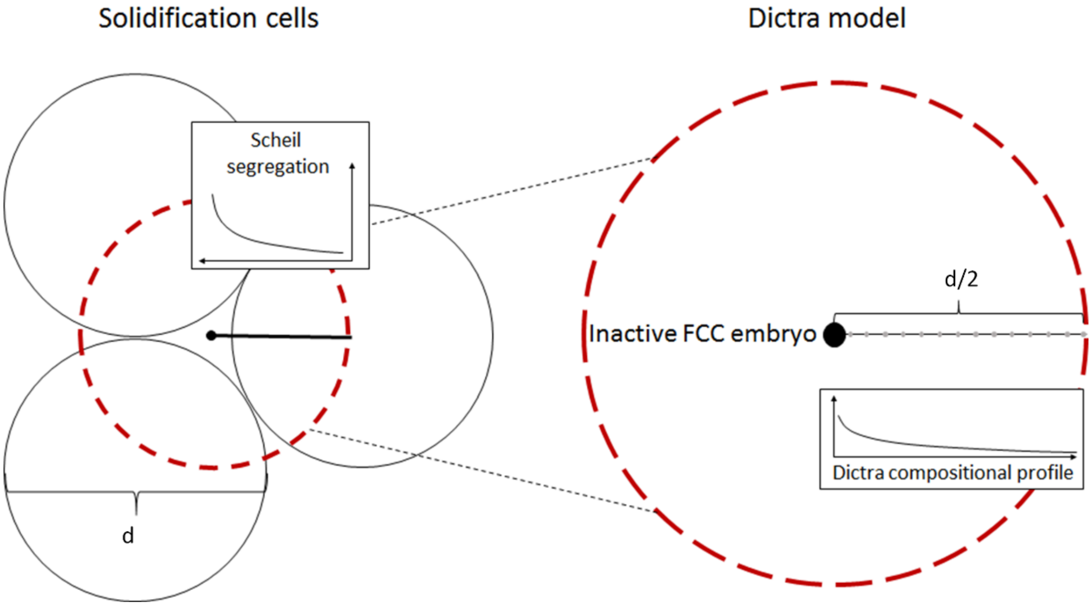

Figure 24: Schematic representation of the strategy behind the Diffusion model. The model is built with cylindrical symmetry and assumes that the center is the last part of the material to solidify. The center was also the position of the FCC Cu embryo in the final stages of the simulation

The cycles reported on Figure 17 were applied to all samples considering a model radius of 50µm, Figure 22 shows the results for the Cu concentration from Scheil, after the Piping, after the Homogenization treatment and after PWHT. At service temperature, an undercooling of 5 ºC and 12 ºC was applied to the B2 and H1 samples respectively, once again to compensate for differences between the Fe-Cu system and the actual alloy.

As can be seen on Figure 22, the larger segregation happens for B2. In all cases, the forging process causes a severe drop in the local segregation. This drop diminishes considerably in the following steps, causing a maximum reduction of 0.01% wt. in the higher concentration area. Essentially, with the model set up in this manner there is little effect on the segregation profile for Cu after the first step. Following PWHT, the model was submitted to the service condition, wherein a Cu FCC inactive nucleus was located at the center of the model and it was allowed to evolve for 100k hours. Figure 26 shows the compositional profile evolution for several times.

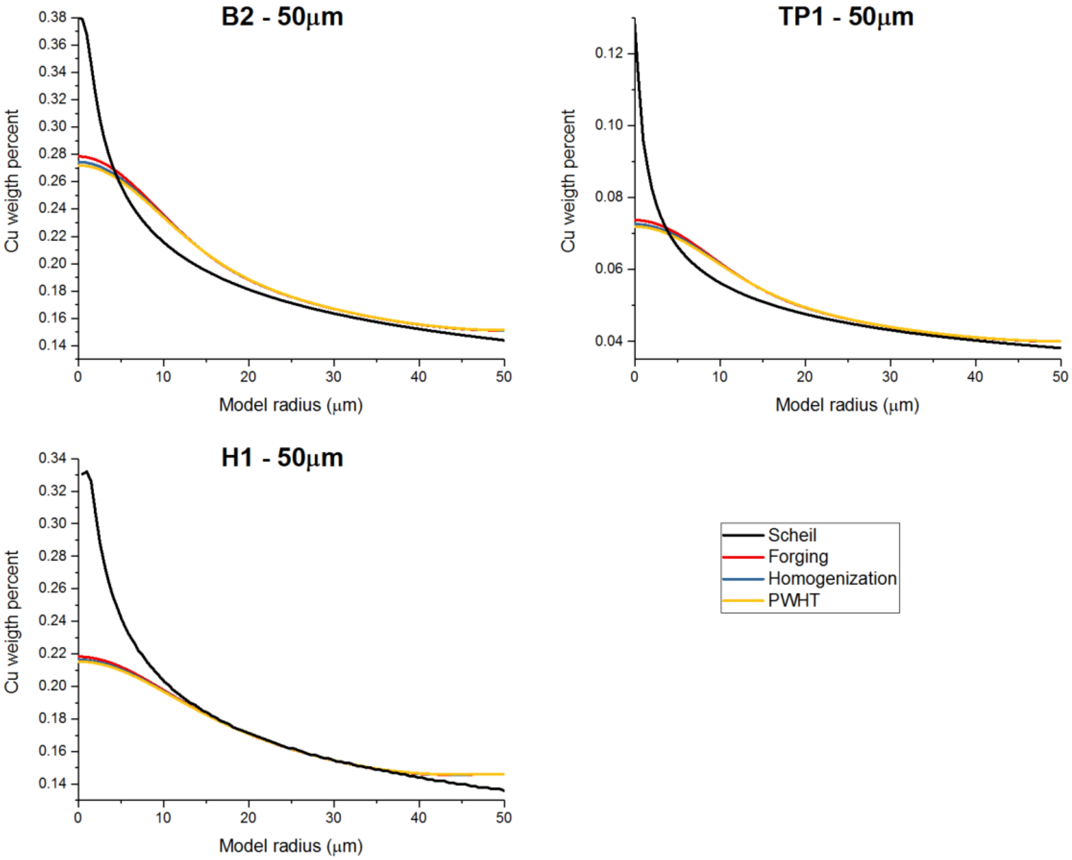

Figure 25: Compositional profile evolution after several simulation steps (Forging, homogenization and PWHT) for the three materials. The model was cylindrical with a radius of 50 μm and the graphs display the Cu weight percent concentration as a function of radius. The initial composition extrapolated from the Scheil model is also shown.

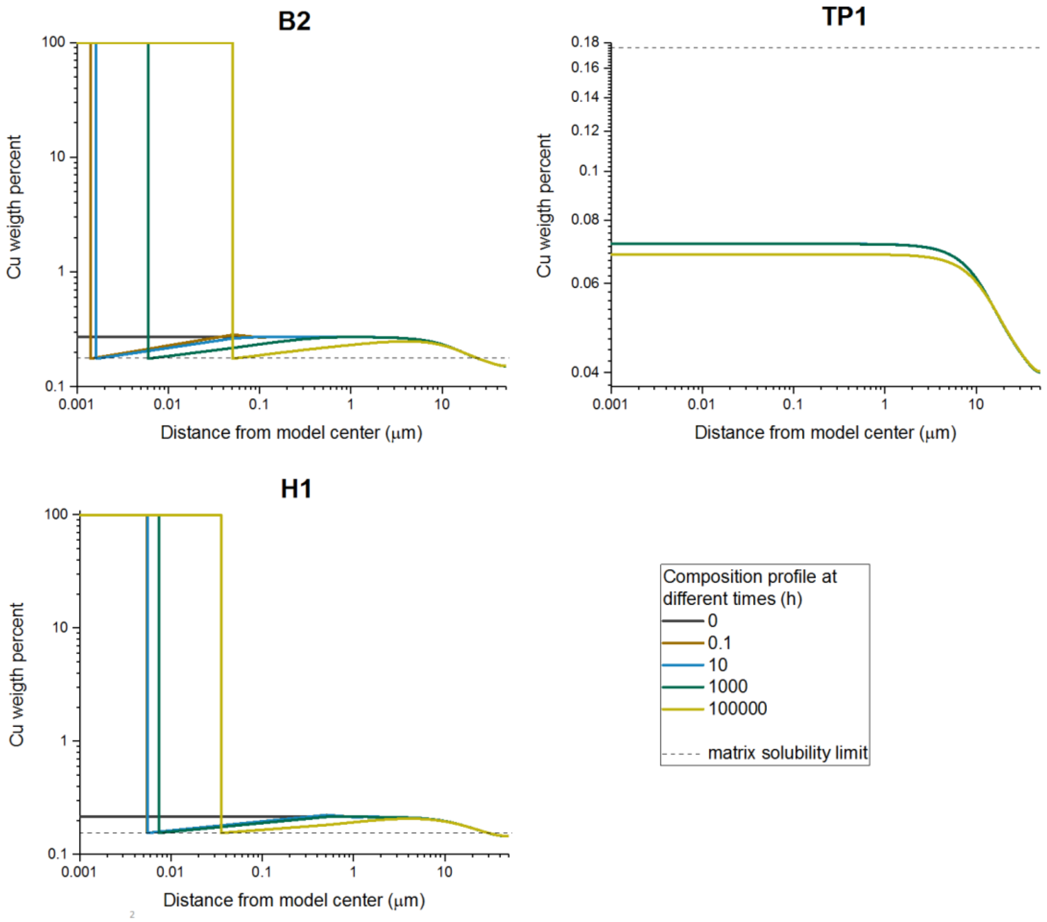

Figure 26: Composition profile at the service temperature for the three materials at several different times. The model was cylindrical with a radius of 50 μm and the graphs display the Cu weight percent concentration as a function of radius. The matrix solubility limit is also shown.

Figure 26 shows that nucleation and growth is happening both for H1 and B2. On TP1, there is no supersaturation in any region of the model therefore, FCC formation never happens. In B2 and TP1, most of the material is still supersaturated. The Cu particles grew up to tens of nanometers, mostly at the expense of the highly saturated region close to the center of the model. The position of the interface as a function of time is shown on Figure 27. Nucleation happens at time zero and growth is fast at small times, slowing down as time advances. The diffusion module does not model nucleation probability or rate of embryo formation. Instead, if enough thermodynamic driving force exists, the inactive phase will nucleate. In the case of the B2 and H1 models, nucleation happens at the first iteration, at essentially time zero. As shown on Figure 27, the Cu layers would have grown a few tens of nanometers reaching a size of roughly 30 nm when damage was first noted. The Cu layers were identified in the samples through EDS mapping using TEM and SEM. From TEM measurements, the Cu layer thickness is around 50-80 nm (Figure 20), matching model predictions within an order of magnitude.

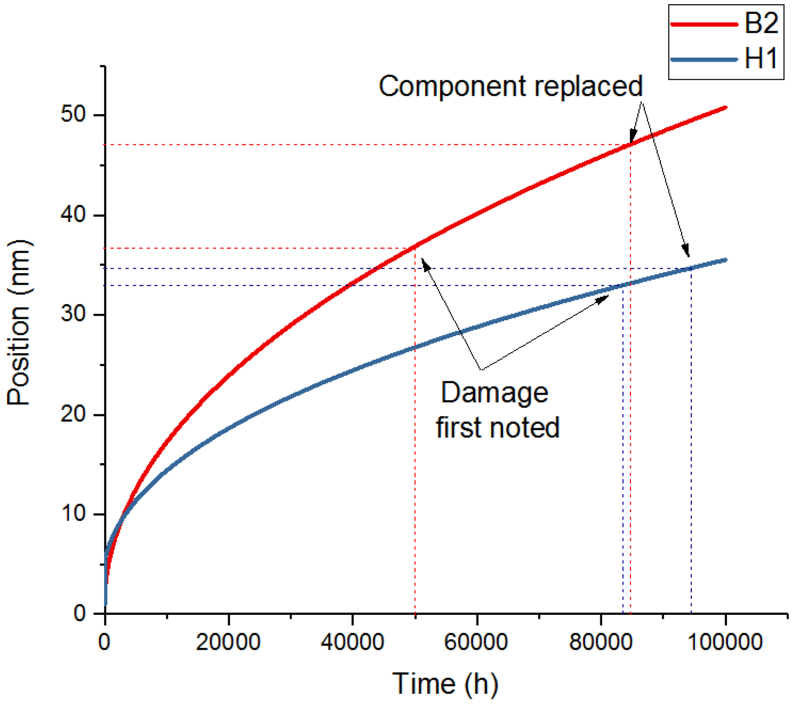

Figure 27: FCC interface position as a function of time. The FCC nucleus was inserted at time zero in the position 0. The model was cylindrical with a radius of 50 µm. The lines display the interface position for the B2 and H1 samples. Times at which damage was first noted and at which the components were replaced are also shown.

There are two main effects that can drastically change the results taken from the models. The first one is a change in mobility in the service temperature, which will affect the growth rate of the FCC Cu layers. The second is the size of the models, which as discussed before, is defined by the secondary dendritic arm spacing which vary widely with cooling rate. To observe the consequence of changes in these parameters, the model used for B2 was repeated with changes in mobility and model size.

The growth rate of Cu layers is mostly affected by the diffusivity of Cu atoms in the BCC matrix. In the temperatures analyzed, diffusivity may be extremely affected by features on the material which increase diffusivity. In higher temperatures this effect is negligible given the large vacancy density values, therefore, this effect would not apply on the processing history of the material. However, during service and in the heat affected zone, the material experiences large plasticity given the creep conditions, which would yield a large dislocation density and therefore, dislocation assisted mobility would have a large effect. To verify this effect, the simulation of B2 in service condition was repeated using a dislocation assisted diffusivity model. The dislocation density was assumed to be $10^{14}/m^2$, which is consistent with high plastic deformation[47] and a reduction of 20% was assumed for the energy barrier for an atomic jump. The position of the interface as a function of time is shown on Figure 28:

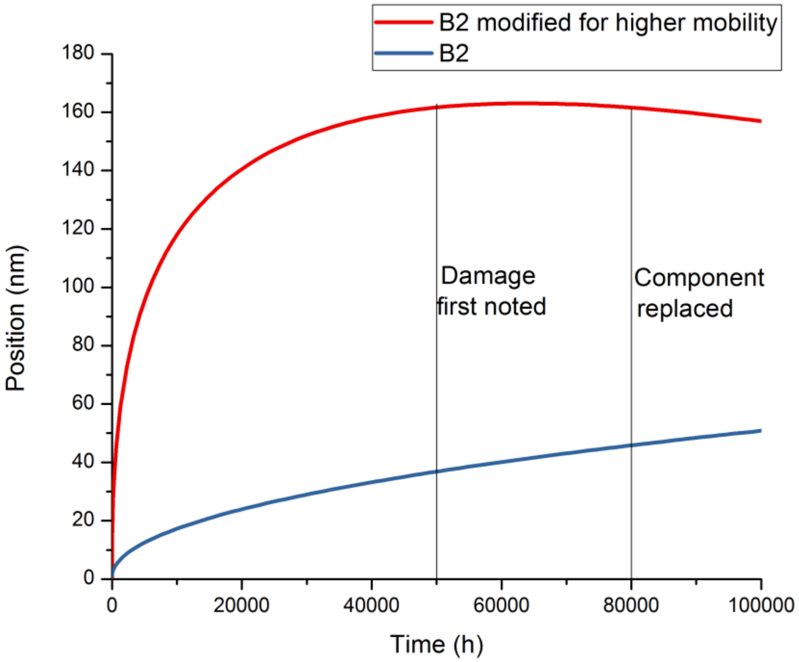

Figure 28: FCC interface position as a function of time. The FCC nucleus was inserted at time zero in the position 0. The model was cylindrical with a radius of 50 µm. The lines display the interface position for the B2 sample under the standard model and modified to include dislocation assisted mobility. Times at which damage was first noted and at which the component was replaced are also shown.

Figure 28 shows that with the increased diffusivity model the size of the layer can reach up to 150 nm which is consistent with some of the SEM EDS maps. Figure 28 also shows that the interface position for the higher mobility model recedes with time. This is caused by the fact that a small region of the model closer to the maximum radius is undersaturated with Cu. With time, Cu atoms in the FCC layer start to move back into the matrix to fill this region up to the max solubility level, which causes the interface total size to diminish. This is shown on Figure 29, where at a time of 100k hours, most of the matrix is at the saturation level, and a region with radius higher than 30 µm is increasing its Cu level. Nonetheless the equilibrium size would be close to 120 nm, which is still consistent with the EDS mapping observations, although slightly higher than what is observed through TEM imaging.

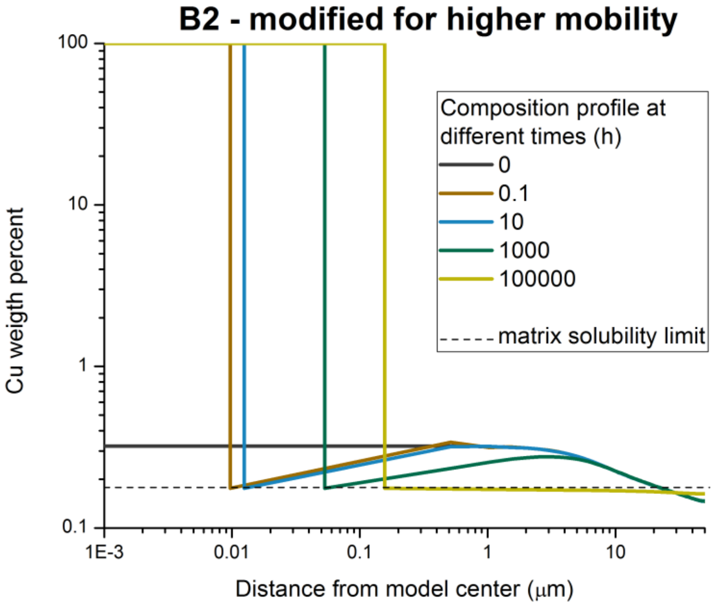

Figure 29: Composition profile at the service temperature at different times for the B2 sample calculated with a model modified to include dislocation mobility. The model was cylindrical with a radius of 50 μm and the graphs display the Cu weight percent concentration as a function of radius. The matrix solubility limit is also shown.

As for the effect of the model size, since it is not possible to define a cooling rate directly, it is interesting to observe what would be the effect of a larger or smaller cooling rate on the FCC phase behavior during service. As mentioned before, this rate will determine the secondary dendrite arm spacing and therefore the model size. To observe this effect, simulations were done with the B2 sample with three different model sizes. These were

100 μm, 50 μm, and 25 μm in radius, correspondent to cooling rates of 0.5 °/s, 2°/s and 20°/s respectively. Figure 30 shows the compositional profiles for the three cases after Forging, Homogenization and PWHT:

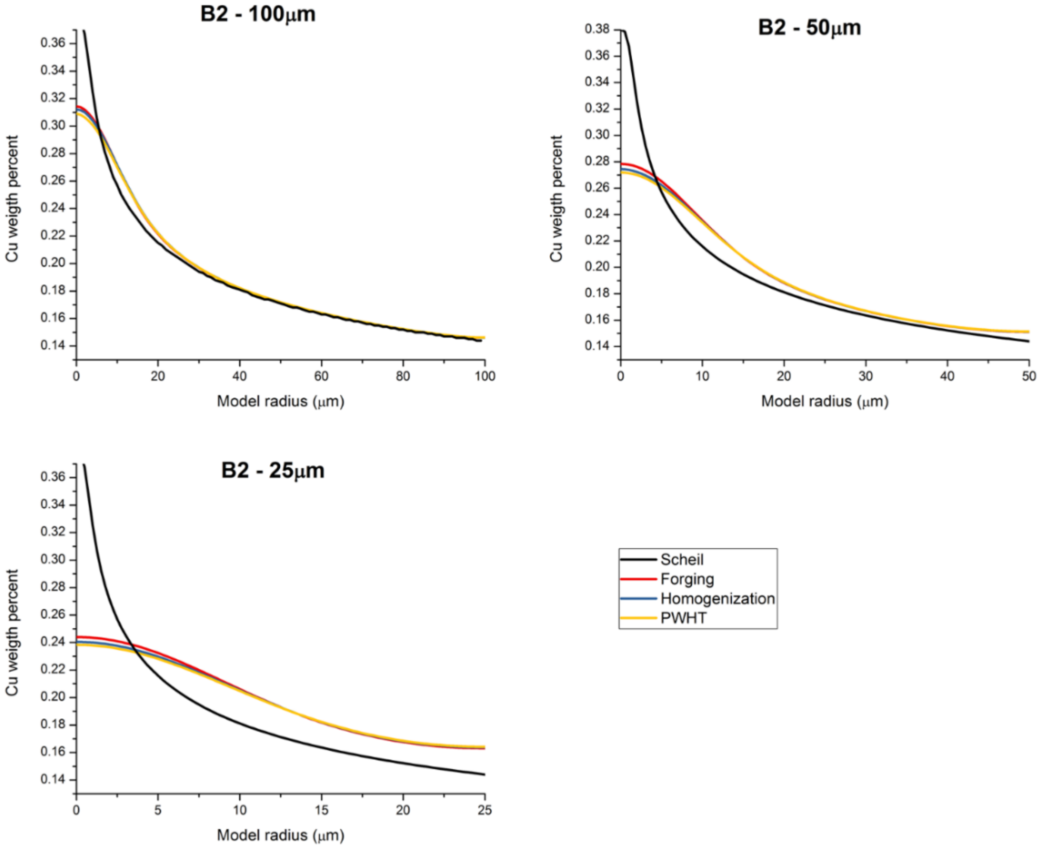

Figure 30: Compositional profile evolution after several simulation steps (Forging, homogenization and PWHT) for the B2 sample calculated in models with three different sizes: 100, 50 and 25 μm in radius. The model was cylindrical and the graphs display the Cu weight percent concentration as a function of radius. The initial composition extrapolated from the Scheil model is also shown.

Figure 30 shows the large effect of the model radius. The larger the radius, the smaller will be the drop in composition on the saturated region. Once exposed to the service temperature step, the FCC phase in the model with 25 μm radius never activated. The reason is the same for the lack of activation when the composition distribution was homogeneous. The position of the interface as a function of time is shown on Figure 31. Growth rate for the 100 μm model is higher than that for the 50 μm model. This is likely because the region adjacent to the FCC phase has a much higher saturation, and therefore, higher diffusion flux. As the interface grows, this behavior would likely change given the larger distances that Cu atoms must traverse to reach the interface.

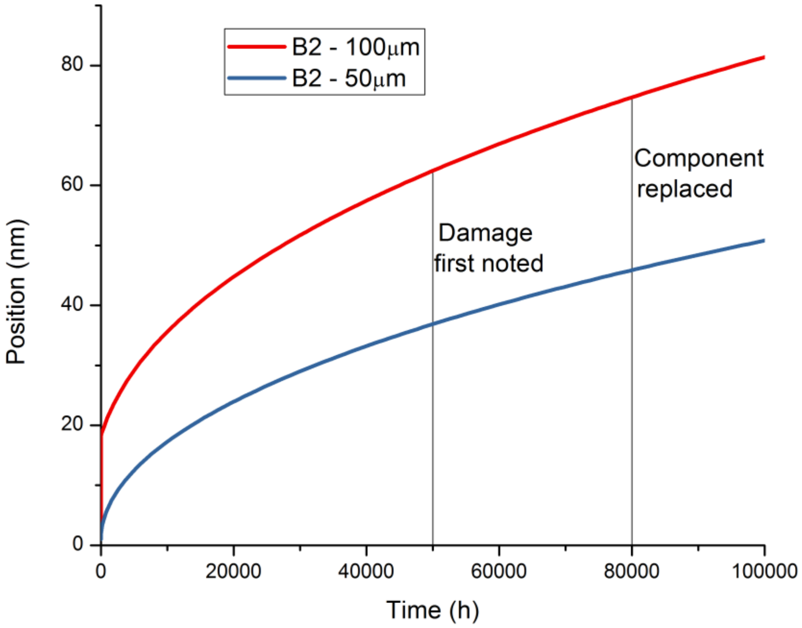

Figure 31: FCC interface position as a function of time. The FCC nucleus was inserted at time zero in the position 0. The model was calculated for sample B2 and the graph displays the position for two different model sizes, 100 and 50 μm. Times at which damage was first noted and at which the component was replaced are also shown.

3.2.4. Discussion

Characterization results show that inclusion particles associated with creep cavities consistently show a Cu presence as seen on the EDS maps. TEM characterization of one of such inclusions show that a pure Cu layer is actually present as a 50 to 100 nm layer between the inclusion and the matrix. This is the case specifically for inclusions present when the material was melted or formed at the end of solidification. As reported previously, the TP1 component had less creep damage than the other samples, while also having a smaller inclusion density. Notably, this component also had the lowest amount of Cu in its composition, and none of the observed inclusions had a Cu layer associated with them. This indicates that along the inclusions, the observed Cu layer may be a catalyst for creep cavity nucleation. Notably, in the TEM foil observed, the Cu layer was more prevalent in the interface between inclusions and cavities, suggesting that the cavity may have nucleated at such position.

A CalPhaD based Pseudo-binary Fe-Cu phase diagram for the studied materials shows that a Cu rich disordered FCC phase is thermodynamically stable at the service condition for the B2 and H1 components, but not for TP1. Even then, the service temperature is very close to the solvus temperature for the Cu rich phase, and simulations indicate that growth of this phase would not take place within the time frame of the materials service history if the Cu composition distribution was homogeneous along the microstructure. However, nucleation and growth could happen through heterogeneous nucleation on Cu enriched regions of the microstructure.

The Cu rich phase is often found associated with MnS, which in the three analyzed materials forms at the end of solidification. Cu partitions to the liquid in the materials analyzed and the matrix would have a higher Cu concentration at the end of solidification adjacent to MnS and other particles coming from the liquid. Even with this local enrichment the Cu content in the matrix is undersaturated until the material reaches the service condition, and the compositional gradient is not steep enough to promote the mass flux necessary to homogenize the Cu composition across the complex thermal history experienced by the components. Once at service temperature the local enrichment of Cu coming from the solidification process is enough to promote nucleation and growth of the Cu phase.

In summary, the formation mechanism for the Cu layer can be hypothesized as follows:

1) During solidification, most solute atoms are rejected from the solidifying material into the liquid. These include Mn, S and Cu among others. As more material solidifies, the liquid becomes richer in these solute atoms and a higher concentration of solute is retained at each solidifying layer, leading to a compositional gradient from the center of a dendrite to its edge.
2) By the end of solidification, MnS particles start to form in the liquid. Some of the preexisting particles in the liquid, such as Al_2O_3 and other inclusions may also be trapped in between dendrites, close to the forming MnS. The last region of the matrix to solidify is adjacent to these particles, and it is also the region with the highest Cu concentration in the fully solidified matrix.

3) During the material’s thermal history some homogenization takes place, but a compositional gradient subsists, with its maximum still adjacent to the MnS particles.
4) When the material reaches the service temperature, a pure Cu FCC phase becomes stable. This phase will nucleate in the regions where driving force is increased, that is regions where supersaturation is highest. These correspond to the regions at edges of dendrites. The growth of the Cu layer is fed by the solute enriched surroundings.

The mechanism is illustrated in Figure 32.

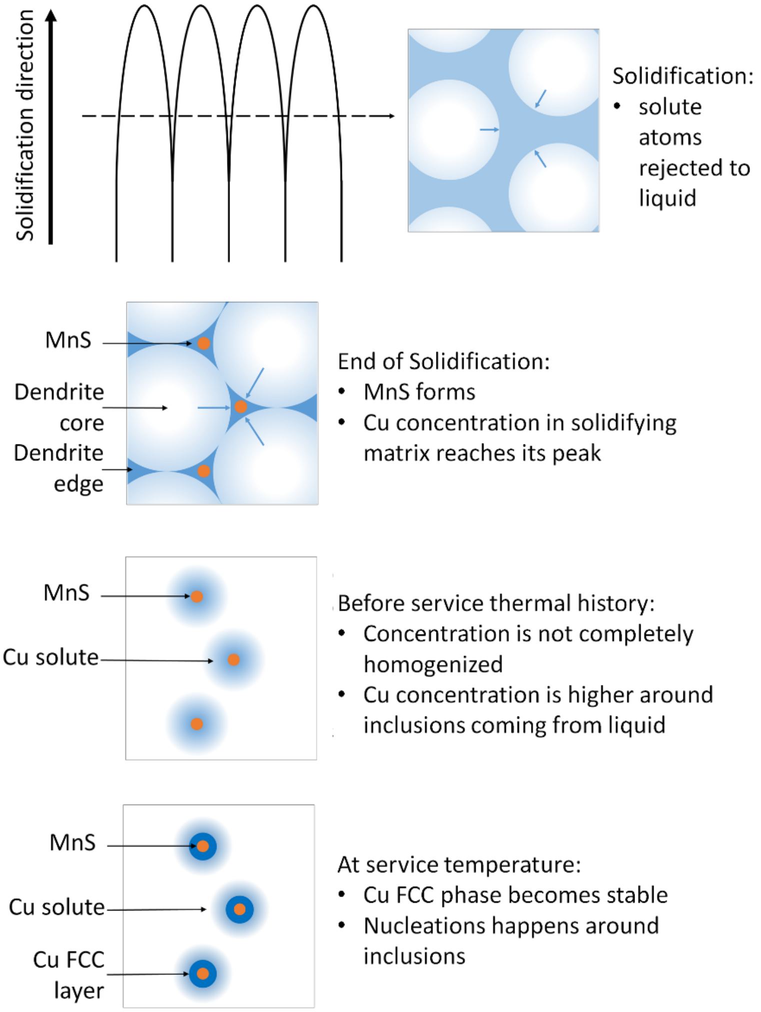

Solidification:
- solute atoms rejected to liquid

End of Solidification:
- MnS forms
- Cu concentration in solidifying matrix reaches its peak

Before service thermal history:
- Concentration is not completely homogenized
- Cu concentration is higher around inclusions coming from liquid

At service temperature:
- Cu FCC phase becomes stable
- Nucleations happens around inclusions

Figure 32: Schematic representation of the Cu FCC layer formation process.

Some discussion is still warranted regarding the modelling results. The forging process has a large effect on dissipating the Cu segregation as after this step, the Cu content in the Cu rich regions can reach ¾ to half of its original value, depending on the secondary dendrite arm spacing. The additional treatments, such as homogenization, tempering and PWHT have little effect on the compositional profile for Cu. However, the effect of the forging step was solely related to changes in compositions coming from diffusion at that temperature. During forging, the material also experiences intense deformation. Still, although this deformation can be expected to stretch or compress the segregation profile, the Cu compositional distribution would still be monotonic, with a rich and poor region. Dislocation assisted mobility can also be neglected due to the ease of dislocation annihilation and high vacancy equilibrium density, both existing at such high temperature.

The behavior of the model is largely dependent on its size. If a secondary dendrite arm spacing of 50 μm (equivalent to 20 °C/s) is considered, the matrix would be homogenized, and Cu FCC would not form in the service temperature. Homogenization is less effective for larger spacings, but these would be caused for lower cooling rates. If the cooling rates are sufficiently low, diffusion in the solid would have to be considered during solidification and the Scheil composition profile would no longer be applicable. This means that there is a middle range for which segregation is considerable and the dendrite spacing is large enough that the thermal history will not erase it. Based on the simulations presented, this interval is around 10^{-1} to 10^{1} °C/s, although precise values for the limits would require further studies.

3.2.5. Summary and conclusions

Based on part 1 of this work, one of the materials analyzed had better creep performance than the other two. Observations show that in the majority of analyzed creep cavities on the two materials with lower creep performance, the present inclusions were surrounded by a Cu layer.

The presence of Cu seems to have a major effect on creep cavitation given the high number of inclusions in B2 and H1 containing Cu layers, and furthermore, the number of inclusions with Cu layers associated with cavities. CalPhaD predicts that at the analyzed temperatures, a Cu FCC phase should form in the materials. However, diffusion simulations in Thermo-Calc® show that this won't happen if the Cu compositional distribution is homogeneous. If there are Cu rich regions, nucleation will occur, and the Cu phase will be stable. Given the high partition of Cu during solidification, the last region to solidify will be Cu rich. Additionally, for the expected conditions for the casting of Grade 91 components, the thermal processing history of the material is not sufficient to erase this partitioning, unless solidification is abnormally fast. During service condition, this Cu rich region serves as a nucleation point for Cu rich FCC phase and prevents the Cu compositional distribution from homogenizing. Simulations show that growth of this phase is slow but could happen through the material's lifetime in service. If mobility is increased, growth is accelerated and reaches equilibrium condition in about one fifth of the expected lifetime. In both cases, the thickness of the Cu layer according to the model is comparable to experimental results. Due to the simplifications and assumptions used in the Cu FCC formation model construction, it is not possible to get precise values for the behavior of this transformation. However, the assumptions made are consistent with what should happen in the alloys, and the behavior observed during the simulations will apply to the analyzed materials.

Another phase that forms at the end of solidification is MnS. There is also the possibility that Al oxide particles remained in the liquid until the end of solidification. This explains both how MnS particles form around Al oxide, and also show that the richest Cu region would be around the MnS particles. This added Cu phase can have an increased effect on reducing interfacial energy and promoting crack nucleation. In fact, as discussed in [33], the presence of Cu above 0.1 % wt. is detrimental to creep properties. After this threshold, increased amounts of Cu do not affect performance. As shown on Figure 21, at the service temperatures, the FCC Cu phase would form at compositions above around 0.1 % wt. Therefore, the formation of the Cu phase observed here and its correlation with diminished creep performance is consistent with previous observations[33][44]. Furthermore, this detrimental effect is correlated with the Cu concentration and sequential Cu FCC formation around inclusions.

A question still remains regarding the effect of the Cu shell around inclusions in the creep properties of the materials. Previous studies have shown that loss of creep ductility due to inclusions occur from the early nucleation of creep cavities around inclusions [44]. The formation of the Cu layer around such can aid in increasing interfacial energy and reduce incubation time for cavity nucleation, but may also not participate in the cavitation process. In the samples analyzed, the sample with higher creep ductility had the smallest inclusion content, but also the smallest Cu content. To separate the effect of Cu, Further characterization of failed components with different inclusion and Cu content is necessary. Particularly, the evaluation of components with high inclusion but low Cu content will elucidate which compositional aspects require stricter control.

3.2.6. Supporting Materials

Detailed description of Time-temperature sequence used in the simulations for the observed Cu shell

The following table shows the temperature profile to which the system was subjected during the diffusion calculations. Groups of steps correspond to different steps of the thermodynamic processing of the materials. Depending on the temperature the materials were subjected to, a different phase had to be used on the matrix. This phase is also shown for each step.

Table 7: Detailed information on temperature and time used in the processing steps simulated on the Grade 91 material.

Process being simulated	Temperature profile	Phase used as matrix
Piping	Heat to 1250°C at 1°C/s	Austenite
	Stay at 1250°C for 3600s	
	Cool to 865°C at 1°C/s	
	Cool from 831 °C to 300°C at 1°C/s	Ferrite
Homogenization	Heat to 831°C at 1°C/s	
	Heat to 1100°C at 1°C/s	Austenite
	Stay at 1100°C for 1800s	
	Cool to 865°C at 1°C/s	
	Cool from 831 °C to 300°C at 1°C/s	Ferrite
Tempering	Heat to 765 °C at 1 °C/s	
	Stay at 765°C for 7200s	
	Cool to 300 °C at 1 °C/s	
Welding	Heat to 831 °C at 50 °C/s	
	Heat to 950 °C at 50 °C/s	Austenite
	Cool to 865 °C at 15 °C/s	
	Cool from 831 °C to 300 °C at 5°C/s	Ferrite
PWHT	Heat to 765 °C at 1 °C/s	
	Stay at 765°C for 7200s	
	Cool to 300 °C at 1 °C/s	
Service condition	Heat to service temperature, either 570 °C or 585 °C at 1 °C/s	
	Stay at service temperature for 100k hours (3.6 x 10^8 s)	

Adjustment of simulation conditions for Cu shell growth simulations

Due to simulation limits, it was not possible to get convergence on the service temperature with more elements than Fe and Cu, therefore only these two elements were used. The issue with this simplification is that the binary phase diagram for Fe and Cu is not necessarily representative of the pseudo-binary for the alloys. Figure 33 shows the binary phase diagram for Fe and Cu with the service temperatures and compositions for H1 and B2. As can be seen, H1 is above the Cu solvus, and in this simplified system, would not lead to nucleation. To compensate for that, the Gibbs free energy difference between the matrix and matrix + Cu FCC phase was calculated with the complete composition of both alloys in their service temperatures. This difference was found to be -0.0203 J/mol in H1 and -0.0294 J/mol in B2.

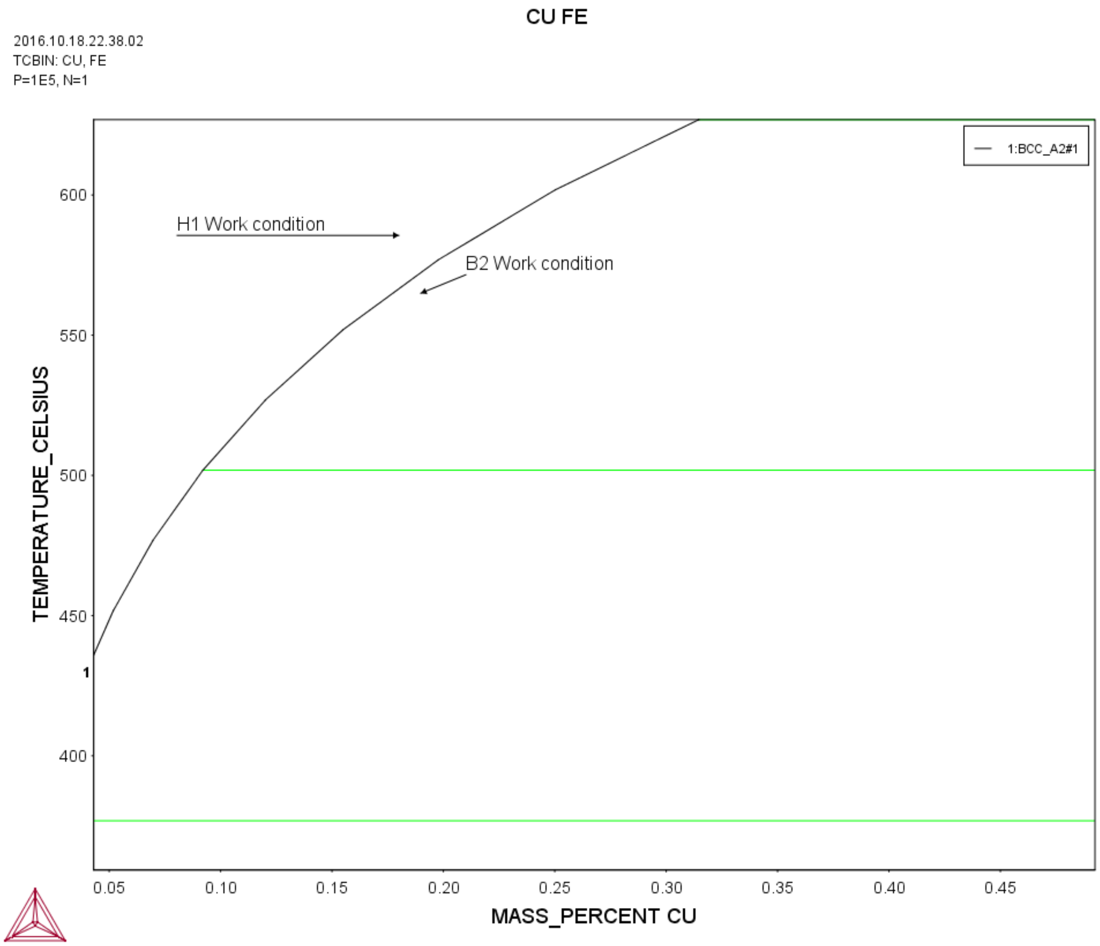

Figure 33: Binary phase diagram for a Fe-Cu system. The work temperature and compositions for B2 and H1 are also shown.

For the simulation to properly represent the actual case, two main characteristics must be emulated. The first one is the free energy gain when nucleation happens, since this will contribute to the mobility driving force, and the diffusivity of the elements in the system. Diffusivity will depend mostly on vacancy concentration and bond energy of the atoms in the matrix. These are not expected to change remarkably when the actual system is compared with a simplified matrix containing only Fe and Cu, since in the actual system, Fe represents roughly 95% of the atoms in the matrix after the PWHT. Therefore, the major adaptation that must be made is to change the simplified system conditions to properly represent the Gibbs free energy difference after FCC Cu formation. To do this, the Gibbs free energy difference on the BCC → BCC + FCC precipitation reaction in the Fe-Cu binary system was calculated as a function of temperature for compositions 0.19 and 0.18 weight % Cu. These energies are shown in Figure 34(#) below. As shown on the Figure, to get a Gibbs free energy difference equivalent to the alloys, the Fe-Cu system has to be set at a temperature of 553 °C for H1 and 565 °C for B2. All calculations performed to represent B2 were done in the Fe-Cu system with a composition of 0.19 weight percent Cu, and to represent H1, with 0.18 weight percent Cu. Whenever these calculations were performed in the service temperature, the calculations were done at 553 °C and 565 °C for H1 and B2 respectively. For TP1, the temperature used was also 565 °C.

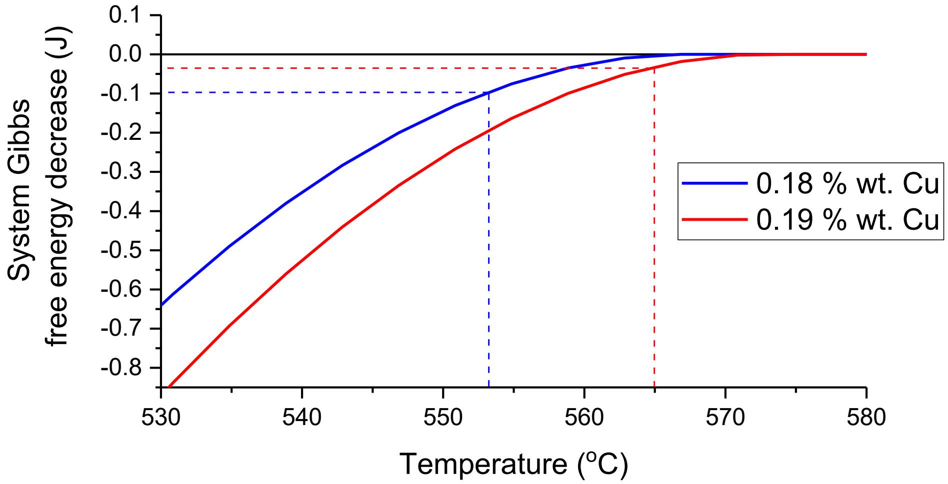

Figure 34: Gibbs free energy decrease on the BCC to BCC + FCC precipitation reaction in the Fe-Cu binary alloy calculated for Cu weight percent of 0.18 and 0.19. The service temperature and temperature in which the Gibbs free energy matches the value for precipitation in the alloy system in its service temperature are also shown for H1 (a) and B2 (b).

Chapter 4. Characterization and Modelling of the Segregation Profile in Additively Manufactured Ni alloys and its effect on Solid State Phase Transformations

This chapter contains a more mature usage of the solidification methodology portion of the modelling approach. The application case is additively manufactured Ni superalloy 718. This is an interesting application case as alloy 718 experiences heavy segregation during solidification, and this segregation is more pronounced for Nb. Nb is also the element which induces the precipitation of the main strengthening phase, γ”, and of δ phase. As such, segregation can have a large effect on the precipitation behavior of as-solidified parts. Additionally, on Laser powder bed additive manufacturing, the cooling rates and thermal gradients experienced by the material are on the opposite extreme to the solidification conditions explored in the previous chapter.

On section 4.1, it was necessary to create an actual compositional map of the as-solidified microstructure for comparison with measured data. This was done following the same approach used in in Chapter 3, to correlate f_s with the square of cell radius. This approach has been done several times in the literature [11], [48], but it loses its meaning at the intersection of neighboring dendrites. In this Chapter, this is addressed by considering a periodical cell arrangement.

The equilibrium condition for solidification was metastable interface equilibrium, and some exploration of a non-equilibrium solidification is also presented (entries 3 and 4 on Table 1 respectively). The metastable condition for the construction of the phase diagram was defined based on a literature review of the phases typically observed during solidification. Temperature history during solidification was taken from simulations found in the literature concerning the same material manufactured under similar conditions. Solidification morphology was defined as cellular based on temperature gradient vs. solidification rate diagrams found in the literature, and on microstructural observations. The length scale of cells was defined using a modified fundamental model for primary dendrite arm spacing. The $C_s = f(f_s)$ equation used was the Scheil equation. The effect of non-homogeneity in the liquid and solute trapping during solidification is analyzed through different models.

In section 4.2, the modelled segregation profile is used to investigate transformations in the solid state. Long range diffusion simulations for phase growth are performed similarly to what was done on section 3.2. However, in this Chapter, time resolved data is presented for the transformation kinetics, allowing a better evaluation of the model. In addition, local precipitation behavior is evaluated.

4.1. On the use of Metastable Interface Equilibrium Assumptions on Prediction of Solidification Micro-segregation in Laser Powder Bed Fusion

This work was performed in collaboration with

Kamalnath Kadirvel[1], Alejandro Hinojos[1], Wei Zhang[1], Yunzhi Wang[1] and Antonio Ramirez[1]

1) Department of Materials Science and Engineering, Ohio State University, Columbus, OH, United States

Guilherme Abreu Faria performed most of the characterization and modelling, and all of the analysis.

Kamalnath Kadirvel provided the dendrite arm spacing determination.

Alejandro Hinojos provided the TEM data presented.

Wei Zhang, Yunzhi Wang and Antonio Ramirez provided guidance.

This article has been published on a special Additive Manufacturing issue of the Science and Technology of Welding and Joining Journal. Full reference:

G. Abreu Faria, K. Kadirvel, A. Hinojos, W. Zhang, Y. Wang, and A. J. Ramirez, "On the use of metastable interface equilibrium assumptions on prediction of solidification

micro-segregation in laser powder bed fusion," Sci. Technol. Weld. Join., vol. 24, no. 5, pp. 446–456, Jul. 2019.

Keywords: Nickel base superalloy 718; Non-equilibrium Solidification; Scheil segregation model; Additive Manufacturing

Abstract

Many models have been developed to explore solidification segregation and dendrite structure in additive manufactured parts. However, these models are either limited in compositional scope or computationally expensive, compromising their application. Numerical solidification models based on interface metastable equilibrium assumptions, such as the Scheil model, are a good alternative. They are computationally efficient and readily applicable to multi-component systems. In this work, the micro-segregation results obtained using the Scheil model are compared with compositional profiles measured in a laser powder bed fusion (L-PBF) build of alloy 718. Using a model for primary dendrite arm spacing, a methodology to predict solidification micro-segregation compositional maps based on the Scheil model is presented and quantitatively contrasted against experimental data measured in a dendrite by transmission electron microcopy. The accuracy of the methodology and the validity of its implicit assumptions on L-PBF conditions are discussed.

4.1.1. Introduction

Metal additive manufacturing (AM) is a transformative technology addressing manufacturing challenges in several fields, such as aerospace and biomedical. One of the most applied AM techniques is powder bed fusion with a laser heat source (L-PBF)[49]. L-PBF is based on the scanning of a focused laser beam on a powder layer surface in a pattern that fills the cross-section shape of the part being built. Once a layer is complete, a new powder layer is applied over the previous surface and the laser is scanned for the next cross-section. In L-PBF, the dimensions of the molten pool are on the order of a hundred microns, and as such, the distance between adjacent tracks and layer thickness are typically around 50 μm. This leads to a very refined surface roughness and high fidelity to designed part shape. The small molten pool rapidly solidifies, resulting in a microstructure that resembles a weld. This microstructure is quite unique, with very refined (~1 μm) columnar or equiaxed grain structure [21].

Alloy 718 is a Nb bearing, precipitation strengthened Ni-base superalloy[50], [51]. Its high corrosion resistance combined with its high strength at elevated temperatures make it an ideal material for applications involving long exposure to high temperatures, such as aerospace and energy industry components. The need for complex geometry parts in these industries makes L-PBF of alloy 718 a strategic priority[52]. Additionally, alloy 718 is known for its good weldability, resulting from its slow precipitation kinetics, when compared to other Ni superalloys [8]. The uniqueness of the solidification structure from L-PBF requires specific post processing conditions for homogenization, strengthening aging or stress relief heat treatments. Typically, the heat treatment conditions have been developed based on the nominal composition of the alloy, or on empirical evaluation of materials produced through other conventional methods. However, when applied on L-PBF parts, they can generate undesirable results. For example, Amato et al. [53] observed formation of γ” in alloy 718 processed using L-PBF after an annealing and Hot Isostatic Pressing (HIP) treatments, both performed at temperatures above 950 °C. However, the γ” solvus temperature for the nominal composition is close to 900 °C. In alloy 718, Nb partitions to the liquid during solidification. As Nb stabilizes δ and γ” phases, the higher Nb content at interdendritic regions increases solvus temperatures and accelerates precipitation reactions.

In order to accelerate the deployment of additively manufactured parts, tools that can adequately predict solidification microstructures and how they can be post-processed are required. Phase field models (PFM) [20], [54], [55] can provide quantitative predictions of microstructure evolution. Specifically, they can be used to study dendritic structure formation, solute segregation and solidification texture during AM [18], [56]–[58]. However, these methods are computationally expensive to be performed at the large length and time scales required by the additive manufacturing process. Hence, many PFM studies [18], [57] restrict the simulations to binary alloys while the real alloy system is typically multicomponent. Some studies further assume constant cooling rate and thermal gradient [56], [57] which may not be a reasonable assumption as it is known that different regions of the melt pool experience different cooling rates and thermal gradients [59].

During electron-beam power-bed fusion process [60] the changes in solidification rate and thermal gradient can be large enough to change the grain structure from columnar to equiaxed configuration.

Given the limits involved in the use of PFM, there is a need for alternative modelling approaches which satisfy the requirements for speed and versatility of some AM applications. An alternative approach is the use of interface metastable equilibrium (IME) assumptions. Under this approach, the compositions at the solid/liquid interface at a specific temperature can be calculated based on metastable equilibrium phase diagram information, without the need for kinetic calculations. One example of a modelling approach based on such assumptions is the Scheil-Gulliver method[25]. This method is widely used to predict solidification behavior and second phase formation in many alloy systems, including Ni superalloys [61]. However, it does not consider morphology in its formulation. Nonetheless, if the solidification morphology diagram for alloy 718 is considered [62], the typical values for thermal gradient and interface velocity in L-PBF would result in a columnar dendritic structure. Under this condition, the solidification grains observed are formed through epitaxial nucleation and growth, so free nucleation of the matrix phase (e.g., γ) in the liquid pool is not commonly observed. Therefore, by predicting the primary dendrite arm spacing (PDAS) between cells, assuming that radial growth of dendrite cells is isotropic on the plane perpendicular to growth direction, and combining it with results from IME based methods, the segregation profile across cells can be determined.

In this work, we evaluate the use of solid-liquid IME assumptions for predicting as-solidified microstructures in L-PBF of alloy 718. Results from the IME based Scheil method are combined with PDAS calculations to obtain micro-segregation maps, and modelling results are contrasted against measured compositional profiles. The effect of implicit IME and Scheil hypotheses on the final result is also addressed.

4.1.2. Experimental Method

Builds

The additive manufacturing parts analyzed were produced as 15 x 15 x 15 mm^3 test blocks. The detailed processing conditions are available in reference [51], and some key processing parameters are provided in the following for completeness. Builds were produced in an EOSINT M280 machine. Laser power of 285 W and scanning speed of 960 mm/s were used. The substrate was preheated to 80 ºC, layer height was 40 μm and hatch spacing was 100 μm. The scan direction was rotated by 67^o after each layer was finished.

Characterization

The blocks were sectioned parallel to the build direction at their center, and the cross-sectioned samples were ground and polished using colloidal silica by following the standard sample preparation practice for metallography. Scanning Electron Microscopy (SEM) characterization was performed on as-polished samples with a FEI Apreo microscope. Images were obtained with an in-lens detector with a filter for higher energy electrons, optimized for backscattered electron signal. The incident electron energy was 2 keV. Electron Backscattered Diffraction (EBSD) was performed to identify grain orientation. EBSD data was captured with an incident beam energy of 20 keV. By combining the use of EBSD and backscattered electron data, regions suitable for Transmission Electron Microscopy (TEM) were chosen and a FEI Helios focused ion-beam (FIB) microscope was used to extract thin foils for TEM. Through this process, the foil analyzed in this study was determined to have its cellular growth direction parallel to the foil plane. Transmission and scanning transmission electron microscopy (STEM) were done with a FEI TF-20 Tecnai 200 kV TEM at 86 mm camera length. The microscope was equipped with an EDAX Apollo XLT Windowless energy dispersive X-ray detector.

X-ray Energy Dispersive Spectroscopy (XEDS) data was collected as a map with a pixel size of approximately 2 nm. Elements considered for the map were Ni, Cr, Fe, Nb, Mo, Co Al, Ti and Si. To minimize noise, the map was down sampled with a 4 x 4 pixel binning. To convert counts into weight fractions, a larger map was collected over a 5 x 5 μm^2 region of the foil. The counts were averaged over the whole map, and scalar factors were determined for each element so that the average number of counts times the scalar factor was equivalent to the nominal composition of the powder. These factors were then applied to obtain compositions at each pixel in the higher magnification map.

CalPhaD assessments

All CalPhaD assessments were made using the Ni thermochemistry (TCNI8) and mobility (MOBNI4) databases from Thermo-Calc® [23]. Scheil calculations were done using the Scheil module within the same software. The calculations were made using the alloy 718 composition shown in Table 8. Two sets of calculations were done, one with all elements in Table 8 and one with limited compositional scope for comparison with the solidification diffusion model. Impurity elements such as S and P were not considered. Within the Scheil model, the para-equilibrium model [7] was used to consider C back diffusion. The iterative calculation was stopped when the fraction of solid reached 0.99.

Diffusion calculations were done with the diffusion module within Thermo-Calc®. The model was set up with cylindrical geometry and 100 nodes, with a system size of 0.5μm, equivalent to the typical cell radius. A γ phase (FCC) nucleus was added to the center of the cylinder. The temperature history of the model started at 1400 °C and was cooled down at a cooling rate of 10^6 °C/s [51],[59]. The calculation was done with a simplified system containing Ni, Cr, Fe and Nb.

Table 8: Composition of the alloy 718 powder.

Element	Ni	Cr	Fe	Nb	Mo	Ti	Al	Co	Mn	Si	C
Weight %	Bal.	20	13.5	5	3	1	0.7	1	0.35	0.35	0.05

Dendrite arm spacing determination

Primary dendrite arm spacing was used to determine the length-scale of the compositional map calculation. A classical model for the prediction of PDAS is the Kurz-Fisher model[63]. In their work, an analytical expression was derived for estimating PDAS using the Mullins-Sekerka instability [64] theory on the solid-liquid interface of a binary alloy. This model was extended to multi-component systems and applied to alloy 718 as explained below.

PDAS for the multicomponent system was calculated using the following equations.

$$M_i = \frac{D_L^i}{C_0^i\left(m_L^i - m_S^i\right) + \left(x_L^i - x_S^i\right)} \quad ; \quad \frac{1}{M_{eff}} = \sum \frac{1}{M_i} \qquad \text{eq. 14}$$

$$PDAS = \mu_0 \left(\left|\frac{dT}{dt}\right| G\right)^{-\frac{1}{4}} \quad ; \quad \mu_0 = \left(128\pi^2 M_{eff} \Gamma_{sl} (\Delta T')^2\right)^{\frac{1}{4}} \qquad \text{eq. 15}$$

where i - index of the solute, (e.g., Cr and Fe), D_L^i - diffusivity of solute i in liquid L, C_o^i – average concentration of solute i, Γ_{sl} – Gibbs-Thompson coefficient of solid-liquid interface, $\Delta T'$ - non-equilibrium solidification range (estimated from Scheil [61]) , G - thermal gradient and $\frac{dT}{dt}$ - cooling rate. The solute-dependent phase diagram constants $m_L^i, m_S^i, x_L^i, x_S^i$ were calculated using Thermo-Calc® [23] and the procedure is detailed below.

Compositions of matrix (γ) and liquid (L) phases were calculated as function of temperature in the equilibrium solidification regime (1260 °C−1330 °C) for alloy 718.

Only the elements showing a significant partitioning between γ and L were considered for PDAS calculation and are shown in Figure 35. A linear fit was performed on these data ($T_L = m_L c_L + x_L, T_S = m_S c_S + x_S$) to obtain the solidus (m_S) and liquidus slopes (m_L) along with their respective y-intercept (x_L and x_S) values.

The model was validated using the experimental data reported by Song et al. [65]. Specifically, the predicted PDAS is within the range of the experimentally measured PDAS values (1.0−1.8μm). Figure 36 shows the calculated PDAS for a set of cooling rates and thermal gradients on the range normally observed during L-PBF of Ni alloys [59].

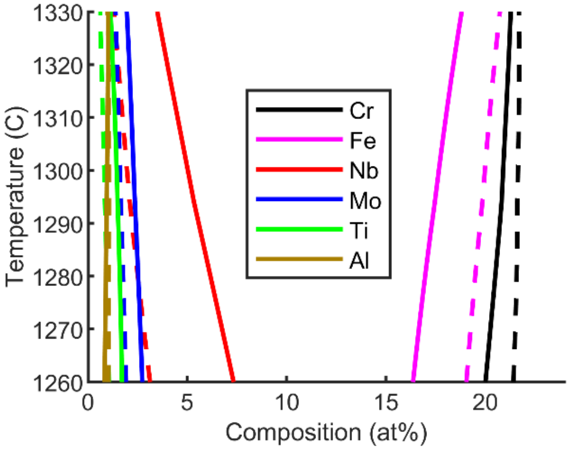

Figure 35: Equilibrium compositions of the solid γ phase (dashed lines) and liquid L phase (solid lines) in the solidification regime (1260 ºC - 1330 ºC) for elements Cr, Fe, Nb, Mo, Ti, and Al.

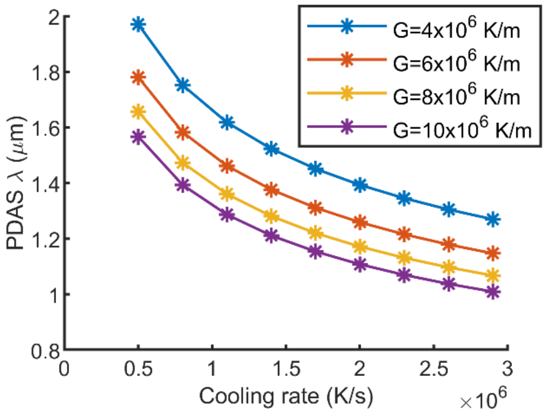

Figure 36: Calculated PDAS as a function of cooling rate for different thermal gradients typically observed in L-PBF [59].

Determination of compositional maps

IME methods deliver compositional information as a function of fraction of solid. Assuming a dendrite cell isotropically grows radially from its core on the plane perpendicular to the cell growth direction, the fraction of solid at each position of the cell can then be correlated with the distance of such position to the center of the cell. This is done by correlating the fraction of solid with the square of the distance from a point in the cell to its axis. However, this relation is not valid at intercellular regions. To overcome this, it is assumed that that cores will be distributed in a hexagonal plane lattice, a spatial arrangement used by Bhadeshia and Svensson for weld metal solidification [66]. Each cell is assumed to grow independently in a cylindrical front (Figure 37). With λ as the dendrite arm spacing and r as the radius in a cylindrical coordinate system centered on the cell core, the fraction of each layer of solid created as the cell grows can be defined as $dS = r\theta(r)$. $\theta(r)$ is fixed when $r < \frac{\lambda}{2}$ and is a function of r when $\frac{\lambda}{2} < r < \frac{\lambda}{\sqrt{3}}$. The fraction of solid as a function of cell radius is determined by integrating $dSdr$:

$$f_s(r) = \frac{\int_0^{\mathrm{r}} r\theta(r)dr}{\int_0^{\sqrt{3}\lambda} r\theta(r)dr} = \frac{1}{\boldsymbol{\lambda}^2}\int_0^{\mathrm{r}} r\theta(r)dr$$

$$\text{where}\quad \theta(r) = \begin{cases} \text{for } r \leq \boldsymbol{\lambda}, & \dfrac{\pi}{2} \\ \text{for } r > \boldsymbol{\lambda},\ 2\cdot\mathrm{acos} & \dfrac{\mathbf{v_1}\cdot\mathbf{v_2}}{|\mathbf{v_1}||\mathbf{v_2}|} \end{cases} \qquad \text{eq. 16}$$

The concentration of solute across the cell structure is determined by interpolating the IME model output on the determined solid fraction.

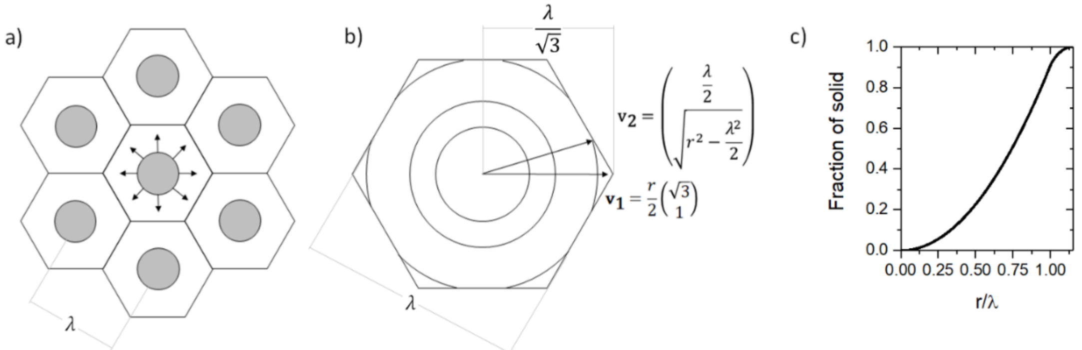

Figure 37: a) Schematic representation of cell distribution as a hexagonal grid. b) Dimensions of a single dendrite cell and mathematical parameters used in $f_s(r)$ calculation. c) Resulting fraction of solid as a function of distance from the cell core.

4.1.3. Results

Figure 38 shows the result of a Scheil model run with the composition in Table 8. On the Scheil method, the metastable condition can be imposed by pre-selecting the phases considered in the CalPhaD calculations [3]. In alloy 718, the second phases commonly observed on solidification are Laves and MX carbonitrides, rich in Nb, Ti, N and C [67]. The model was limited to these phases.

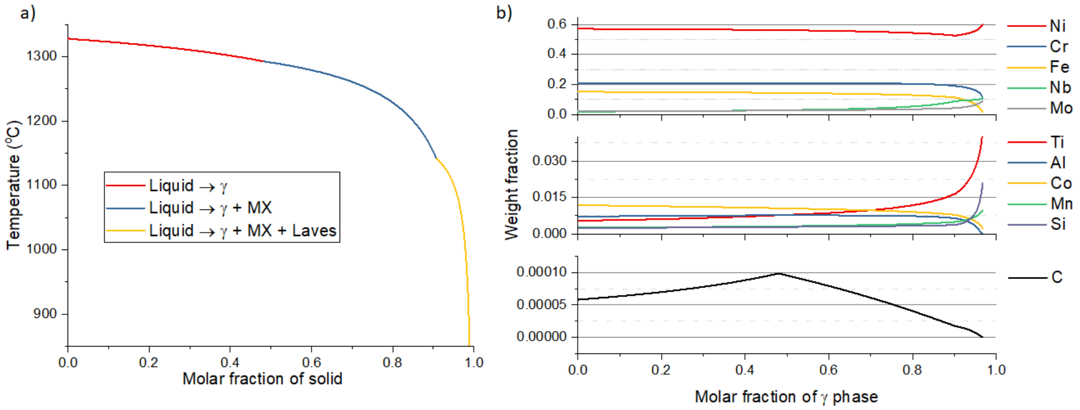

Figure 38: Scheil simulation with full composition results. a) Fraction of solid as a function of temperature. Different lines indicate the transformation path. b) Distribution of solute elements across γ phase as it grows.

The second phases forming on solidification are close to stoichiometric, and therefore, the amount of these phases present when the material completely solidifies will depend on the composition of the liquid while they are being formed. Song et al. [65] identified an average Laves volume percentage of 2.64% in the samples used in this work. Some variability is present, with a maximum volume percentage of 2.81% and minimum of 1.68%. The Scheil model predicts a Laves content of 2.14%. Although there is a match between the model prediction and the measured phase content, this does not imply that the model is correctly representing solidification. Further validation requires comparing the Scheil model γ phase compositional distribution results with the measurements from built materials.

Figure 39 shows the calculated compositional maps derived from the Scheil model results. Gray level corresponds to the expected composition. The regions at the hexagon vertices correspond to the expected volume fraction of Laves and MX phases, and their averaged compositions.

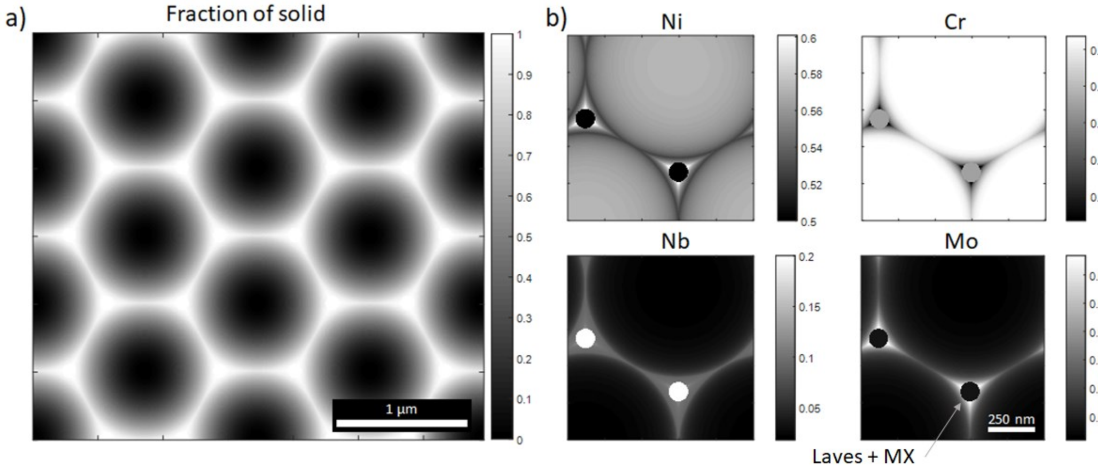

Figure 39: Solidification structure as calculated using the Scheil model with a hexagonal columnar grid. a) Fraction of solid map b) Interpolated distribution for Ni, Cr, Nb and Mo on the solidified structure. The circles at the hexagon vertices have a size equivalent to the volume fraction of as-solidified second phases. The gray level indicates the averaged composition of these phases.

Figure 40 shows the as-solidified alloy 718 AM microstructure imaged using backscattered electrons on the SEM. The orientation of the large grain at the center of Figure 40 (a) was determined through EBSD. The colored cube inset represents the orientation of the austenitic matrix unit cell. The cellular growth direction was at a 45°

angle out of the surface. Due to the imaging condition (backscattered electrons), contrast in these microstructure images is proportional to electron density across the surface, i.e. regions richer in atoms with high atomic number will appear brighter.

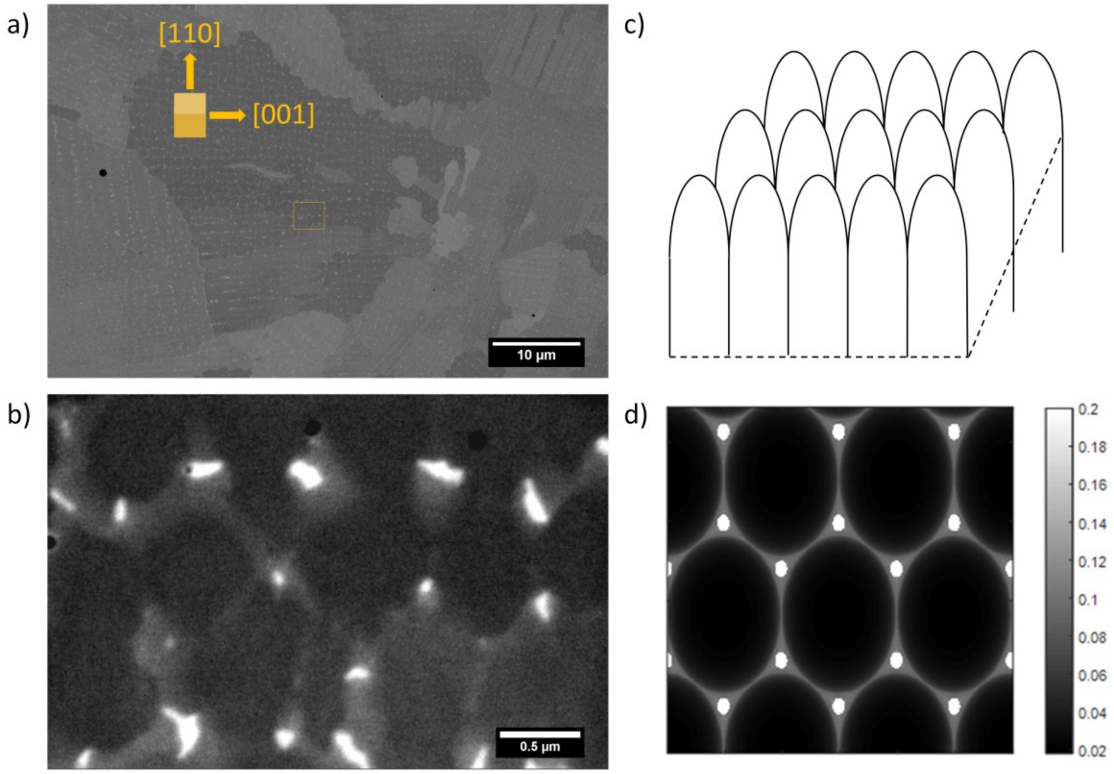

Figure 40: As-solidified additively manufactured Alloy 718 a) Backscattered electron image. The cube shows the crystal orientation regarding the sample surface. Cell growth direction is 45° out of plane in the [100] direction. The rectangle shows the region shown in b. c) Three-dimensional representation of cellular structure with 45° cross section, equivalent to plane on (a). d) Nb distribution for cross section shown in (c).

These figures show that the cellular structure does not follow a perfect hexagonal lattice, with each cell having in average five neighbors. Nonetheless, the bright spots, which correspond to Nb rich regions, follow the expected distribution, being present at the triple boundaries between cells. Additionally, the intercellular regions are rich in high atomic number elements, such as Nb and Mo, as was predicted by the model.

Figure 41 a shows a TEM image of the foil removed from the built sample. The cellular structure can be seen, with the cell axes parallel to the foil. Cell axes are shown as well as the primary dendrite arm spacing. The rectangle region in (a) is further magnified in Figure 41 b. Under the used STEM HAADF imaging condition, the brighter regions in this image are richer in high atomic number elements. A magnified view of the rectangle marked in (b) is shown in Figure c. Both images show that cell edges can be identified through the increased content of high atomic number elements. The rectangle marked on Figure 41 c indicates a region where an XEDS map was collected. The diagonal of the map had a length of approximately 1 μm. Figure 41 d shows maps of the collected X-ray intensity for the Kα edges of some of the elements on the alloy. Image brightness is proportional to number of counts. This image shows that Ni, Cr and Fe are partitioning towards the solid, while Nb, Mo and Ti are partitioning towards the liquid. The intercellular regions are enriched in Ti and Nb. No agglomeration of Ti, Nb, or other measured elements is seen outside of the intercellular region, evidence that no second phases are present at the dendrite core. The larger agglomerates observed at the intercellular region have Nb composition close to that expected for Laves phase. The smaller Ti-rich agglomerates are likely Ti and N rich MX phase. All regions with high Nb and Ti compositions are unlikely to be δ phase, due to the low amount of Ni. Qualitatively, all observations are in accordance with Scheil simulation results.

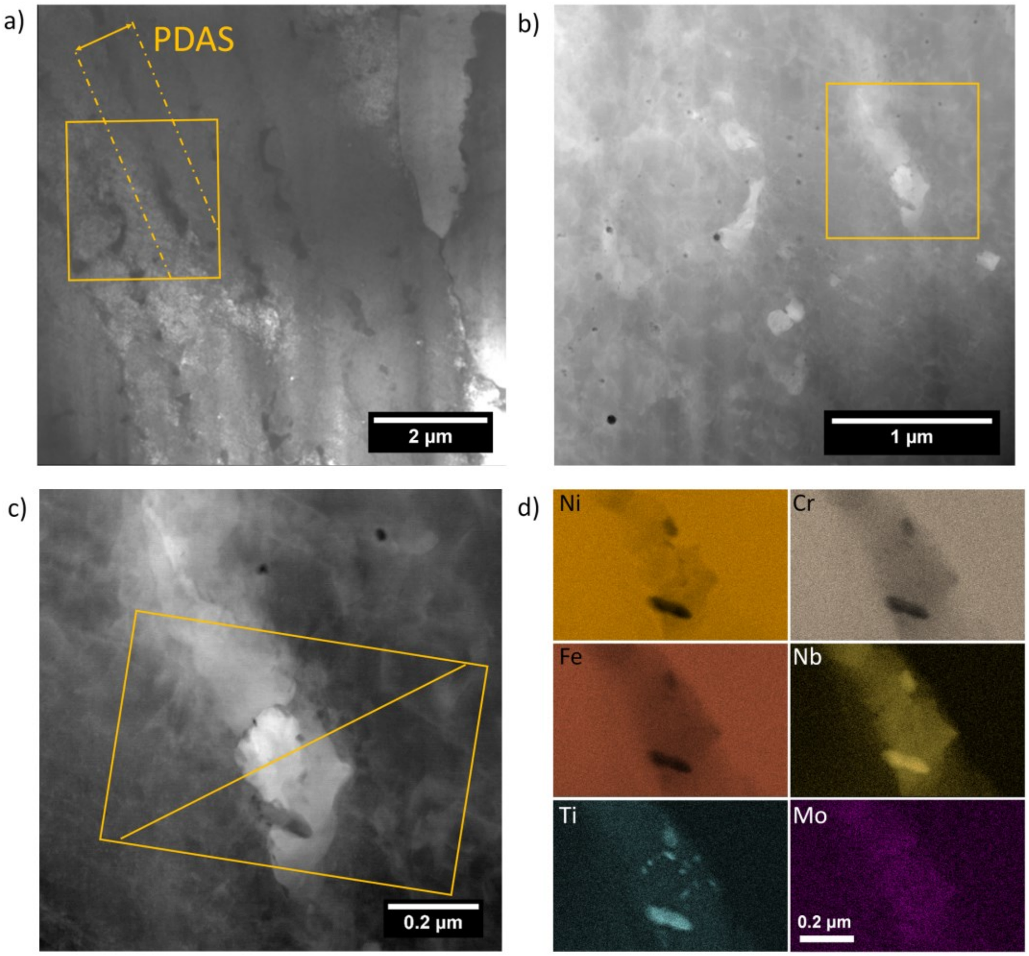

Figure 41: a) TEM image of alloy 718 as-built sample foil. Cell growth direction is parallel to foil. Rectangle shows region in b. b) HAADF STEM image of cellular structure. Rectangle shows region in c. c) Higher magnification image of the foil. Rectangle shows region for XEDS map. Line shows Figure 43 line scan position. d) X-ray counts for different elements.

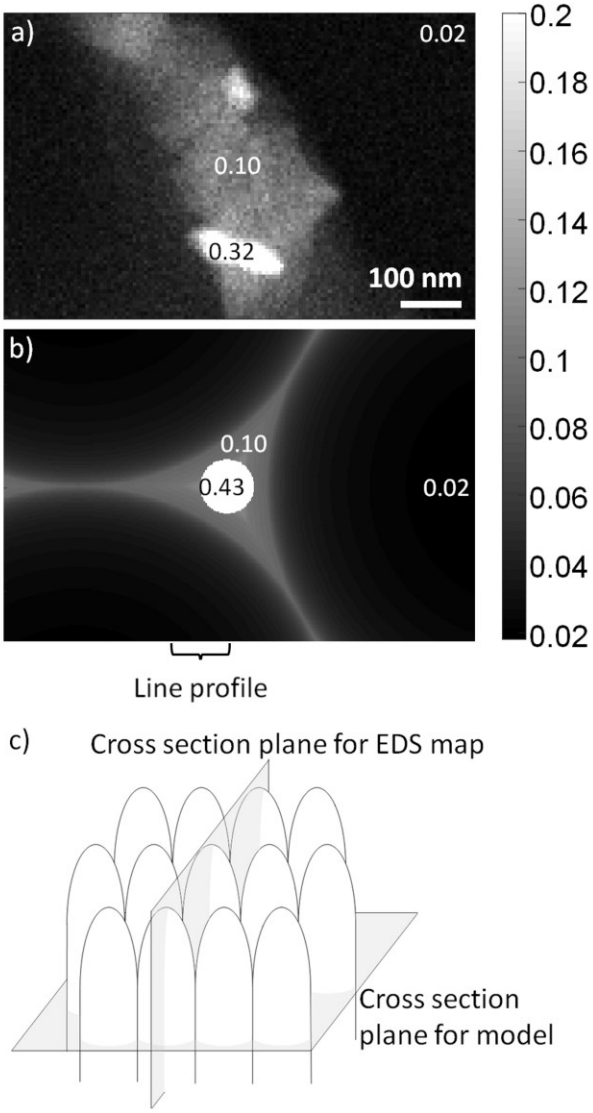

Figure 42: a) Nb mass fraction from TEM XEDS map. b) Modelled Nb mass fraction map. Both maps are on the same spatial and compositional scales. c) Cross section planes for model and measurement. Markers on the bottom of figures b and lines on Figure c show the integration bands from which curves in Figure 43 were obtained.

Figure 42 shows a comparison between the modelled compositional profile and the measured compositional map, specifically for Nb. The dimensions and grey level in both images are at the same scale. The Nb mass fraction is shown for some specific points in both maps. The Nb amount at the core and edges of the cells matches. The mass fraction at the larger particle, however, does not. The foil thickness is estimated to be around 100 nm, and given the dimensions at the particle, it is likely that the measured Nb fraction at that region refers to a combination between the matrix and particle.

The two cross sections represented in Figure 42(a) and (b) are perpendicular to each other. To further compare the measured segregation with the model, the composition profile distribution perpendicular to the cell growth direction was retrieved by a line integration of the compositional maps taken across the line shown in Figure 42 c. In order to compare this profile to model results, the plane at which the cellular structure was sectioned must be considered. The foil position was selected so that it would include cell cores and intercellular regions. Given the presence of Nb-depleted cell core regions and Nb rich intercellular regions with second phases, the foil was determined to be in a plane equivalent to the region marked in Figure 42 b. Considering the foil thickness, the model compositional profile was obtained by averaging the map compositions in a 100 nm band in the horizontal direction as represented on Figure 42 b, as the counts obtained in each pixel of the measured compositional map is an average of the composition across the thickness of the foil. The Nb content at the center of the line profile refers primarily to the composition of Laves phase. It was excluded from the integration since the foil does not show Laves particles along the line profile.

The curves in Figure 10 show that model predictions match observations very closely. Additionally, predictions for the composition of cell core and steepness of the segregation profile are in accordance with measurements. In summary, the Scheil model based compositional mapping can identify the approximate composition at the cell core, cell edges, and an estimation of how the compositional profile is distributed along the cell radial direction.

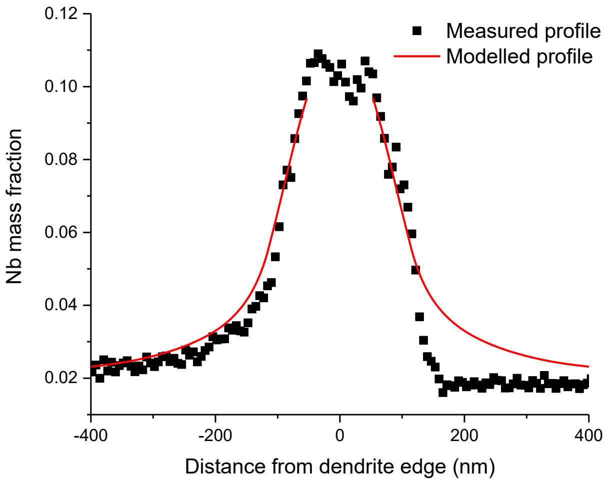

Figure 43: Measured and modelled Nb weight fraction profiles across intercellular region.

4.1.4. Discussion

Overall, the comparison between the observed micro-segregation profiles and model predictions shows promising results regarding the use of IME methods, and particularly, of the Scheil model, in representing the as solidified microstructure on L-PBF. Qualitatively, the match between measured and predicted second phases shows that the model is capturing the transformation pathways, and SEM analyses show that the morphological distribution of solute atoms is close to the model representation.

Quantitatively, the chemical distribution measurements by TEM demonstrate that the predicted segregation profile matches the compositional profile across a cell.

Although the performed measurements support the utilization of the Scheil model, it is still a simplistic implementation of the IME hypothesis, and some discussion is warranted regarding the assumptions it carries. The Scheil model has two main assumptions[68]. The first assumption is that there is no solute redistribution in the solid (other than so-called fast diffusers such as carbon). If there is redistribution, there is a change on the solid interface composition, which changes the chemical potential across both phases, and therefore changes the composition of the newly formed solid layer. The second assumption is that there is complete mixing on the liquid. Similarly, incomplete mixing on the liquid incurs that solute on the liquid close to the interface will either concentrate or dilute compared to the rest of the liquid phase, depending on the partition coefficient. Once again, this would change the conditions for equal chemical potential and the composition of the solid would be changed.

Diffusion in solid and liquid

The Scheil hypotheses with regard to diffusion in solid and liquid were investigated through diffusion kinetics simulations using the diffusion module in Thermo-Calc®. The diffusion module also assumes that the solid-liquid interface is at local metastable equilibrium [23]. Nonetheless, it will calculate driving forces across the solid matrix and solve the diffusion equation during solidification. This modelling strategy has been implemented to calculate segregation in L-PBF alloy 625 AM builds[69]. Due to numerical issues, the diffusion module calculations were limited to a simplified system. Correspondingly, a Scheil simulation with the same characteristics was performed, namely, the same composition was used, and only γ and liquid phases were allowed to form. Figure 44 shows a comparison between the predictions from Scheil and the diffusion module. When compared to the diffusion module results, Scheil predicts a longer solidification temperature range. At the core of the cell, the Scheil model predicts a higher composition of solute with partition coefficient (k_e) higher than one, and lower at the cell edge. The opposite happens when $k_e<1$.

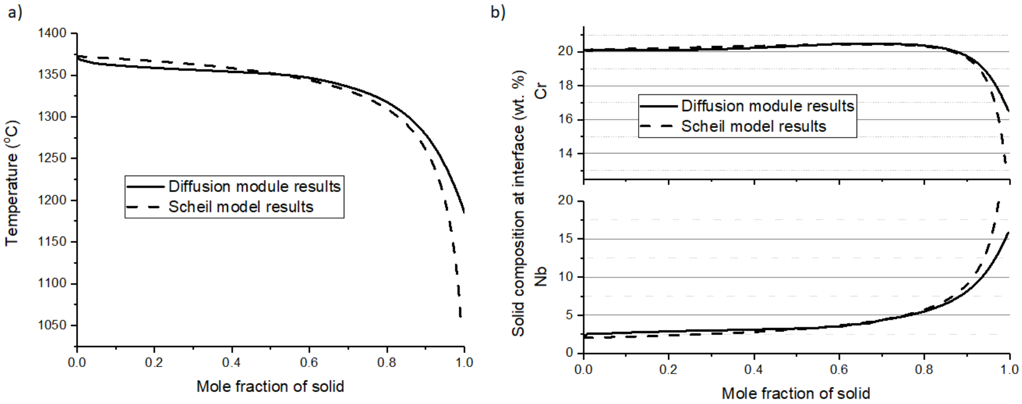

Figure 44: a) Mole fraction of solid as a function of temperature from Scheil and diffusion model. b) Cr and Nb compositions at the solid side of the interface according to Scheil and the diffusion model.

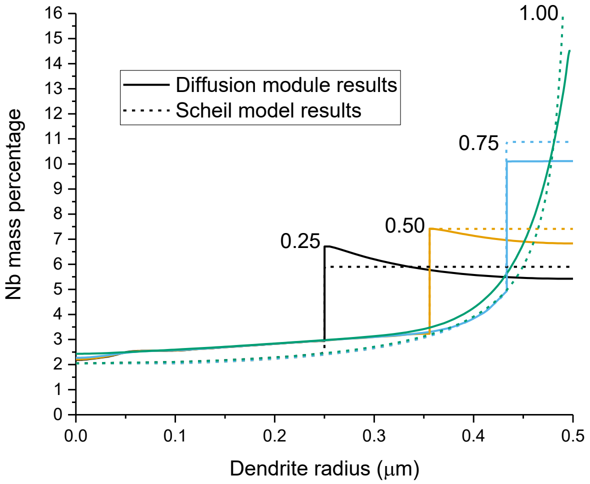

Figure 45: Compositional distribution of Nb across the solidification model. Data is shown for the diffusion and Scheil models. Curves were collected when solid fraction was 0.25, 0.5, 0.75 and 1.00

Figure 45 shows the Nb profile at different fractions of solid predicted by both methods. At the beginning of solidification, Nb concentrates at the interface, changing the composition of the forming solid. As solid grows, there is no variation of the composition of the solid phase. These results show that at the core of the cell, the assumption of no diffusion in solid is accurate, while the assumption of complete mixing in the liquid is not. As the fraction of solid grows, the liquid presents complete mixing, but due to the changes in solid solute content at the beginning of solidification, the liquid at the end of solidification has less solute with $k_e<1$ and more solute with $k_e>1$.

The effect of incomplete mixing on the liquid is not negligible, but still causes minimal changes to the final compositional profile. At the cell core, the diffusion model predicts a Nb composition of 2.54 weight percent, while the Scheil model predicts 2.11 wt.%. This difference ceases to exist when solid fraction reaches around 0.5. From Figure 46, the Nb composition scatter at the cell core can be used to estimate the variance in the TEM XEDS Nb measurements as ± 0.25 %. These models do not fully represent the alloy, as they have a limited composition, but if a similar difference was observed for the complete alloy 718 composition, it would be within the resolution of composition measurements.

Overall, the difference in solute distribution due to incomplete liquid mixing is small. However, this may not be the case for other alloy systems or different process parameters. As the scan speed increases, or when alloy systems in which solute atoms have lower diffusivity on the liquid are considered, this effect will be stronger and may result on different solute distributions. Nevertheless, the effect of solute gradients in the liquid close to the solid-liquid interface can still be taken into account on a Scheil-like model through the method developed by Giovanola and Kurz [10].

Solute trapping

Another implicit assumption on the Scheil model is the interface metastable equilibrium itself. This condition in the interface may become invalid if the interface solidification speed is fast enough. If the interface moves sufficiently fast, solute atoms cannot partition on the liquid fast enough, and the advancing solid layer becomes supersaturated, a phenomenon known as solute trapping [70].

Solute trapping will be more prominent at the cell tip, where interface speed is faster. If considerable solute trapping takes place, the Nb composition at the cell core would be higher than what is predicted by the Scheil model.

Even so, solute-trapping effects can also be taken into account in a Scheil-like model. The equilibrium partition coefficient (k_e) can be changed into kinetic partition coefficient (k_v) to account for high-interface velocities. A simple form of k_v is the Aziz-trapping function [22]:

$$k_v = \frac{k_e + V/V_D}{1 + V/V_D} \qquad \text{eq. 17}$$

where V is the interface velocity, $V_D = D_l/a_0$ is the interface diffusion speed, D_l is the diffusivity of liquid at the interface and a_0 is the interatomic spacing in the liquid.

Ghosh [57] has performed phase field simulations to quantify this effect and V_D for Nb was calculated to be 0.31m/s in the Ni-Nb system. The scan speed on the part analyzed is 0.96 m/s. The interface speed will depend on the alignment between the cell growth direction and the scan speed. Additionally, it will vary as the cell grows, being the highest possible at the cell tip. If the interface is aligned with the scan direction, $\frac{k_v}{k_e} = 1.45$. For a Ni - 5 wt.% Nb binary system, the composition of solid according to the Scheil equation would be 3.3 wt.% at a 0.01 solid molar fraction. Considering the Aziz trapping function this would be 4.6 wt.%. However, this value drops quickly if the cells are not aligned with the scan direction or as the cell grows and the angle between the interface and the cell axis drops. The solute content at the intercellular region would still be changed given the difference in solute content at the cell core.

As evidenced by the very good agreement between the quantitative chemical distribution data collected in this work and the Scheil calculations, solute trapping is not likely playing a marked role for the used set of process parameters and studied alloy.

Implementation of IME based methods for L-PBF

Continued and successful implementation of L-PBF additive manufacturing requires developments in several fields, from streamlined production strategies to tools that allow the optimization of such strategies. Some of the most important tools in this endeavor are models which allow digital prototyping of parts. Successful builds require not only the control of distortions and residual stresses, but also control on microstructure. Obtaining an optimized microstructure requires understanding the microstructural history during the process, and also how it can be modified through post build processing.

As such, a successful build is dependent on the careful selection of all process variables. Many efforts have been directed at the construction of integrated computational materials engineering (ICME) approaches, which would allow the rapid digital prototyping of new parts, and the following design of post processing schedule. The implementation of IME methods is computationally cheap, and when combined with fast acting heat transfer models, may yield a versatile tool for solidification microstructural predictions and as input on how to modify and optimize this microstructure after builds. In this sense, IME based methods are a good candidate for integration in ICME approaches. These methods can consider incomplete liquid mixing and solute trapping, without considerable loss of computational efficiency. For the specific material and process parameters used in this work, the Scheil model was shown to be satisfactory for representing the solidification.

4.1.5. Conclusions

The conclusions of this work can be summarized as follows:

- Characterization results show that the alloy 718 AM microstructure consisted of refined cellular and cellular dendritic structure with an approximately 1 μm primary dendrite arm spacing. The observed spacing matched predictions from Kurz-Fisher model.
- When combined with the predicted primary dendrite arm spacing, the Scheil implementation of the IME condition successfully represented the compositions at the cell core and edge, and especially the micro-segregation profiles along the dendrite radial direction.
- The Scheil model implies some assumptions on the physics of the solidification process. Specifically, it disregards the solute profile on the liquid or the possibility of solute trapping. If these conditions are considered, modelling indicates that for the analyzed material and process parameters, the changes in compositional profile would be still smaller than the scatter observed in the measured

composition. Hence, the Scheil based models are effective to predict the micro-segregation profiles capable of considering a large number of alloying elements at low computational cost.

-

4.1.6. Acknowledgements

This research is supported in part by U.S. NASA ESI Program, under Award No. NNX17AD13G. All microscopy data was collected at the Center for Electron Microscopy and Analysis at the Ohio State University. The authors would like to thank Dr. Adam Hope from Thermo-Calc® for his support. G. Abreu Faria would like to thank the American Welding Society for a graduate research fellowship.

4.2. Modelling and validation of δ formation kinetics on additively manufactured as-built alloy 718.

This work was performed in collaboration with

Kamalnath Kadirvel[1], Alejandro Hinojos[1], Wei Zhang[1], Yunzhi Wang[1] and Antonio Ramirez[1]

1) Department of Materials Science and Engineering, Ohio State University, Columbus, OH, United States

Guilherme Abreu Faria performed the SEM and XRD characterization, and the analysis and modelling.

Kamalnath Kadirvel provided useful discussions.

Alejandro Hinojos provided the TEM data presented.

Wei Zhang, Yunzhi Wang and Antonio Ramirez provided guidance.

Keywords: Nickel base superalloy 718; δ formation kinetics; Additive Manufacturing; in-situ XRD; transformation modelling

Abstract

Additive manufacturing creates a unique solidification microstructure which may not respond to heat treatments in the same ways as wrought or cast products. Efficient

production of additive manufacturing parts requires minimized prototyping of heat treatment procedures. There are widespread modelling approaches in the literature which can identify precipitate solvus temperatures and transformation kinetics across a segregated as-built microstructure. However, these approaches must be compared against actual builds to verify their accuracy. In this work we present a model of the transformation kinetics of δ phase. Decisions made in the modelling were independent of microstructural information, rather being based on literature review of cases similar to the one treated here and on thermodynamic calculations. The model results are compared against the microstructural characterization and in situ synchrotron X-ray diffraction measurements of δ phase precipitation kinetics.

4.2.1. Introduction

Alloy 718 is a precipitation strengthened Ni superalloy, widely used for high temperature applications due to its high strength, oxidation resistance and creep properties. Its outstanding properties come from strengthening phases stabilized by its complex composition [71]. Additionally, when compared to other Ni superalloys, alloy 718 has a higher weldability [1], [72], mainly due to its slower precipitation kinetics.

The main strengthening phases are γ” and γ’ [50], [73], mainly induced by the Nb, Ti and Al content in the alloy. Both precipitate phases are metastable, and at high temperatures (above 800 ºC), γ” is a precursor to δ phase. The effect of δ phase on mechanical properties is complex. Depending on its fraction and morphology, δ phase can reduce ductility at high temperatures [74], or increase formability [75]. It also has the detrimental effect of arresting Nb from the matrix, reducing the volume fraction of beneficial γ”.

The typical aging heat treatment schedule for alloy 718 aims to maximize fraction and density of γ” and γ’ particles. Aging for cast samples consists of two steps: holding between 718 ºC and 760 ºC for 8 to 10 hours, followed by holding between 621 ºC and 649 ºC for 10 hours [76]. The lower temperatures guarantee a large amount of metastable precipitates with negligible amounts of δ phase. Nonetheless, δ formation is much faster in grain boundaries [77]–[79], and as such can still be present in aged microstructures.

The high weldability of alloy 718 combined with its compatibility with high value, temperature resistant and complexly designed parts, such as engine components, make it an ideal application case for additive manufacturing (AM). However, during solidification, alloy 718 experiences large segregation and formation of a number of second phases [1], [80]. This creates a unique solidification structure which may respond unexpectedly to heat treatment schedules designed for cast or wrought materials [53]. The ability to predict how additively manufactured materials respond to heat treatments is necessary for quick development of AM products. In a previous work, we demonstrated a strategy to create a digital representation of the solidification structure, including segregation profiles [81]. In this work we perform a heat treatment on an as-built microstructure and use in situ X-ray diffraction to follow the δ phase volume fraction during the test. The modelled segregation profile is used to create a δ phase growth simulation, and the measured and modelled results are compared.

4.2.2. Experimental Method

Samples

The samples were prepared by laser powder bed additive manufacturing using a Concept Laser Mlab cusing machine. Deposition was done with a laser power of 60 W, 600 mm/s scan speed, 40 μm hatch spacing and 25 μm layer height. Composition of the powder is shown on Table 8.

Table 9: Composition of the alloy 718 powder.

Element	Ni	Cr	Fe	Nb	Mo	Ti	Al	Co	Mn	Si	C
Weight %	Bal.	20	13.5	5	3	1	0.7	1	0.35	0.35	0.05

The parts were built following the design of a Gleeble 3S50 compliant coupon [82]. The build direction was perpendicular to the coupon surface. The region heated during the thermal simulation was ground and polished down to 1 μm diamond paste in preparation for the Synchrotron experiments. Afterwards, the heated region was cut and repolished for electron microscopy imaging.

Synchrotron measurements

In situ δ phase precipitation experiments were performed in the XTMS [83] installation at the Brazilian Synchrotron Light Laboratory. This is an X-ray diffraction (XRD) beamline in which the sample environment is a Gleeble thermo-mechanical simulator. Experiments were performed to follow the precipitation reactions in the samples during a heat treatment by time resolved XRD. Two cases will be considered in this work. In both, the sample was kept at a temperature of 800 ºC for four hours. In one of the experiments, the sample is measured in an as-built condition while in the other, it is homogenized for 30 min at 1100 ºC. For all heat treatments, heating was done at a rate of 100 ºC/s, and cooling at 20 ºC/s. Diffraction data was not collected during the homogenization step due to surface oxidation. On the homogenized sample, the oxidized layer in the surface was removed before the test at 800 ºC.

XRD measurements were done using a Rayonix SX165 detector. Beam energy was 12 keV, and the detector was positioned so that a line connecting the detector window center to the sample would be at 37° of the incoming beam. The detector surface was perpendicular to this line. The distance between detector and sample was approximately 320 mm. A measurement was collected every 120 s. With this setup, each image consisted of partial diffraction cones from the sample. Software GSAS II [84] was used to integrate the arcs in 2θ x Intensity curves. Peak integration was performed in software X'Pert Highscore Plus [85] using a Pearson VII function. Peak intensity was used to determine estimated phase volume fraction using the procedure detailed on [82].

Electron Microscopy Measurements

Electron Microscopy (EM) images were taken at the Center for Electron Microscopy and Analysis at the Ohio State University. Scanning EM images were taken using an FEI Apreo microscope, with a beam energy of 2 keV in backscattered mode. Transmission and scanning transmission electron microscopy were done with a FEI TF-20 Tecnai 200 kV TEM at 86 mm camera length. Diffraction measurements were also performed in this microscope close to the 100 zone axis.

4.2.3. Results and Discussion

Microstructure characterization

Figure 46 shows the materials microstructure for all analyzed conditions. Figure 46 a and b show the as-built microstructure. The solidification structure is cellular, presenting a cell spacing of approximately 1 μm, consistent with previous results. This imaging condition is sensitive to mass contrast, and the segregation structure is visible, mostly due to the effect of Nb. Figure 46 c and d show the homogenized sample. The grain structure of the as-built sample is maintained, with some second phases being present at grain boundaries. The segregation structure is not visible, evidence that composition within each grain is homogenized. Figure 46 e and f show the homogenized sample after heat treatment at 800 ºC. Grains are more polygonal than in the homogenized sample, evidence that substantial grain migration took place during the heat treatment. Globular and needle-shaped particles can be found decorating grain boundaries. This morphology is consistent with δ phase[73]. Figure 46 g and h show the microstructure of a non-homogenized sample after exposure to 800 ºC. Grains are tortuous when compared to Figure 46 c, evidence that grain boundary migration was pinned by second phases at grain boundaries. Needle shaped δ phase particles can be seen inside the grains, following the previous segregation profile. This morphology has been observed for δ phase in non-homogenized additively manufactured Nb bearing Ni alloys exposed to a sub 1000 ºC heat treatment [86].

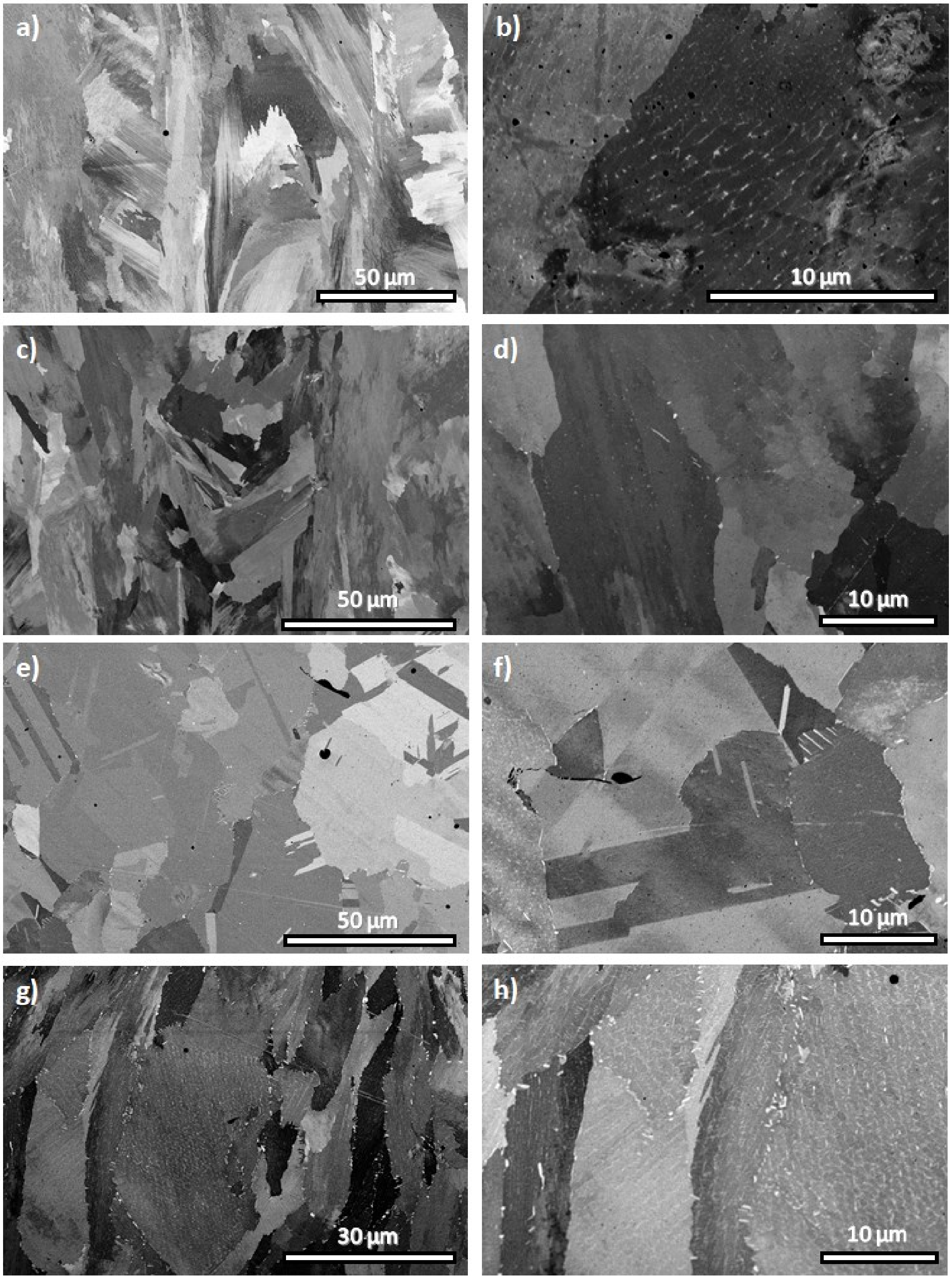

Figure 46: a and b) As-built alloy 718 microstructure. c and d) Microstructure after homogenization (30 min at 1100 ºC). e and f) Microstructure after homogenization and aging (30 min at 1100 ºC and 4 h at 800 ºC). g and h) Direct aging of as-built microstructure (4 h at 800 oC).

Figure 47 shows a high camera length HAADF and diffraction images made with a transmission electron microscope of the as built microstructure. The cellular structure can be seen. The interdendritic region is populated with carbonitrides and intermetallic solidification second phases. As discussed in a previous work, these are most likely Nb rich Laves phase [81]. No evidence of γ’ or γ” can be seen in the as-built microstructure.

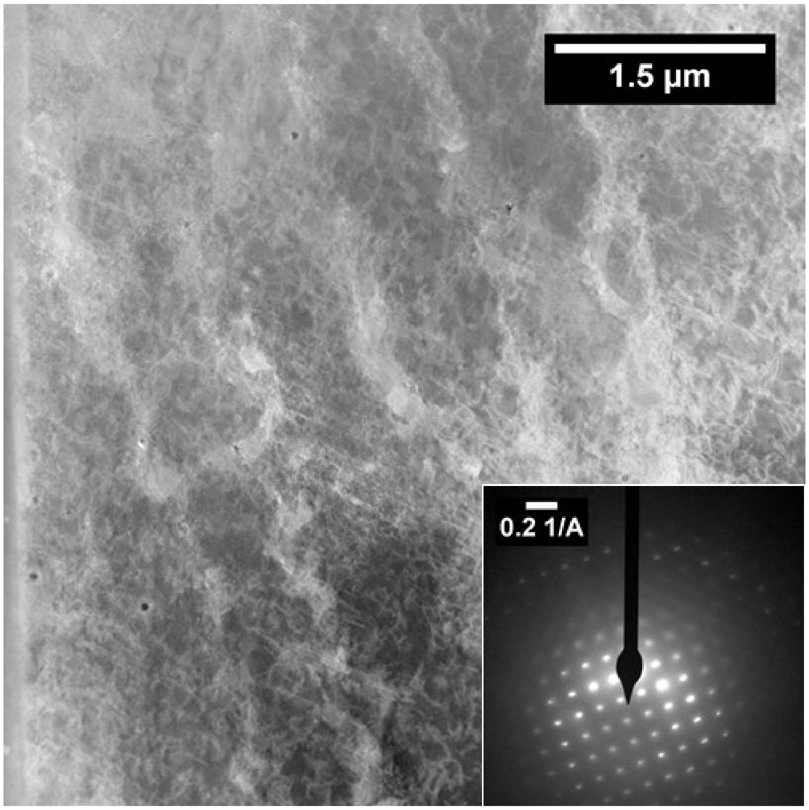

Figure 47: High camera length HAADF image of as-built microstructure TEM foil. Inset shows diffraction image close to the 100 zone axis.

Synchrotron X-ray diffraction measurements

Figure 48 shows an example of diffraction spectra collected for the non-homogenized sample in the as-built state and at 800 °C after approximately 10800 s (3 h) after heating. The peaks present were identified by simulating the diffraction profiles using software PowderCell[87]. The crystal structure used for each phase is shown onTable 10. The lattice parameters were sourced from ICSD and are shown for reference, they were not directly measured in the material.

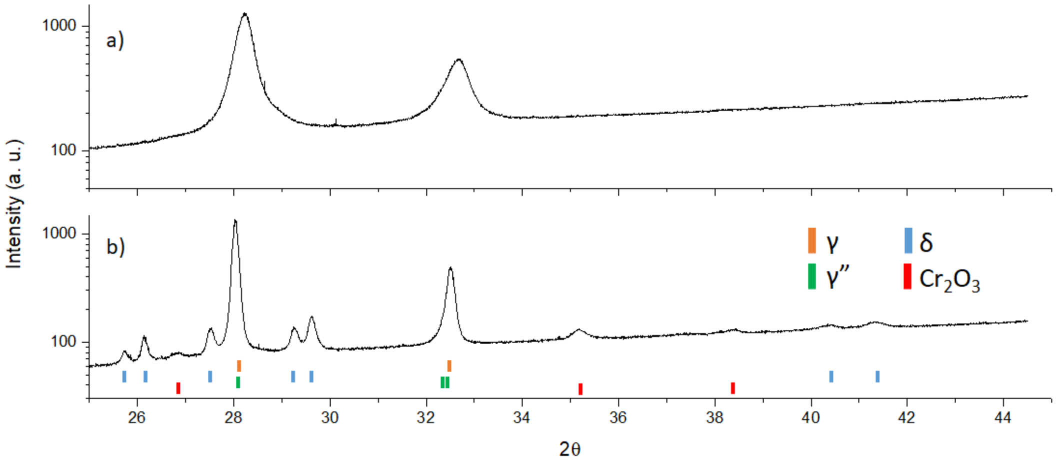

Figure 48: Integrated diffraction curve from AM 718 sample. a) As-built condition. b) Non-homogenized sample after 3 h at 800 °C

Table 10: Crystal structures used to identify observed peaks and compute structure factors.

Phase	Strukuturbericht symbol	Space Group	Lattice parameters
γ	A1	Fm-3m	a=3.524 Å
γ”	$D0_{22}$	I4/mmm	a=3.524 Å, c=7.2 Å
δ	$D0_a$	Pmmn	a=5.162 Å, b=4.347 Å, c=4.531 Å

Figure 48 shows that the as-built microstructure is mainly comprised of γ. The predicted initial phase composition [81] would include carbonitrides and Laves phases. However, the present volume fraction of these phases and their low structure factor makes their peaks not visible in the measured condition. Some asymmetry is seen in the γ matrix peaks. This is normally observed for as-built additive materials and is associated with the segregation present in the matrix [53], [88].

As can be seen on Figure 48, many of the γ" peak positions match the positions of γ peaks. This is accentuated if the two phases are highly coherent, meaning, the lattice parameters match. Coherency between γ and γ" is maximized at the moment γ" is precipitating. Due to this, it was not possible to identify or quantify the amount of γ" present in the system. Some of the asymmetry present in the as-built condition is still present in the second γ peak. This could be due to a transient segregation profile in the matrix or to the formation of δ, however, it was not possible to deconvolute the γ and γ" peaks due to lack of clear shouldering in the main peak.

The structure factor for δ peaks is highly dependent on the composition of the crystal structure, and generally higher than for the γ peaks. This means that the calculated phase fraction of δ has a high dependency on the estimated structure factor. An analysis of possible values for the composition on the δ lattice sites puts the δ volume fraction at the end of the test between approximately 1% and 10% volume for the non-homogenized sample. Due to this large variance, we will only analyze the measured δ volume qualitatively. Figure 49 shows the measured qualitative δ volume behavior during the plateau at 800 °C. There is a considerable amount of δ in the homogenized sample. As can be seen on Figure 46, this δ is either located at grain boundaries, or nucleated at grain boundaries and grew into the grain. This is in accordance with other studies on δ precipitation at similar temperatures and times [89], [90]. The δ fraction measured in the non-homogenized sample includes grain boundary and matrix δ.

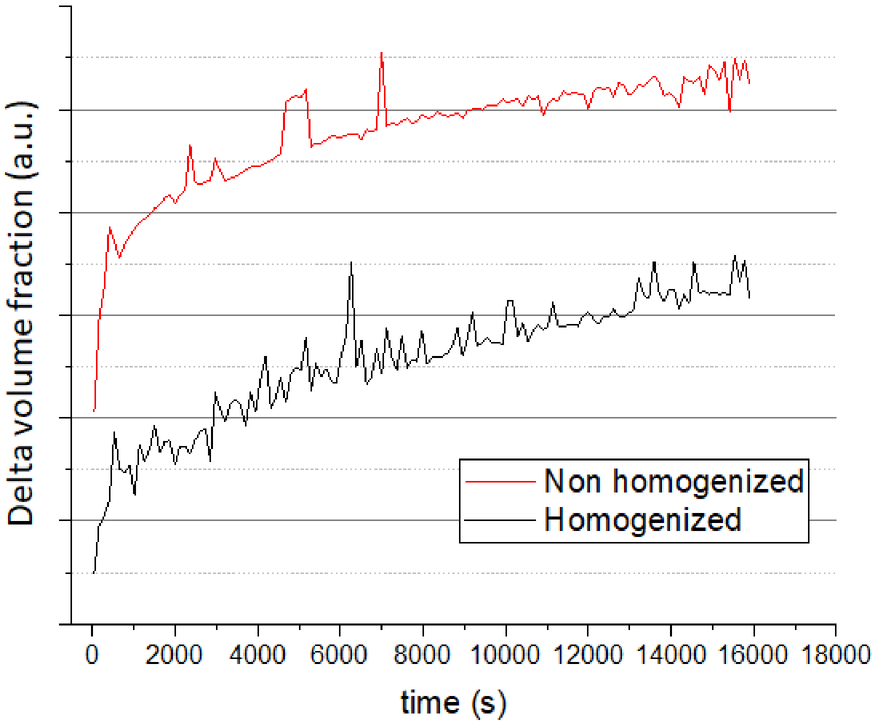

Figure 49: Measured δ volume percentage as a function of time for the homogenized and non-homogenized samples. Final δ volume percentage for the non homogenized case is between 1% and 10%, and for the homogenized case between 0.6% and 6%.

When comparing the homogenized and non-homogenized cases, it is necessary to explore if the formation of δ on grain boundaries would affect the formation of intragranular δ. The mean displacement of Nb in a Ni matrix can be calculated based on the diffusion coefficient of Nb in the system. The diffusion coefficient of Nb in a Ni - 5 wt.% Nb binary system was calculated using the MOBNI5 database in software Thermo-Calc® [23] as 3.386×10^{-13} cm^2/s. With this value, the mean displacement of Nb atoms for the duration of the temperature plateau is approximately 700 nm, orders of magnitude smaller than the grain size. Therefore, δ formation is localized, and formation of intergranular and intragranular δ can be treated as independent precipitation reactions. Additionally, the grain sizes between the homogenized and non-homogenized cases are similar, and the kinetics of formation of intergranular δ should be comparable. It is possible to evaluate the transformation rate for intergranular δ in the non-homogenized case by subtracting the measured δ fraction on both tests.

Figure 50 shows this subtraction resolved against time during the temperature plateau. Formation of intragranular δ is quick, and stagnates at around 2000 s. If a trendline is considered (smoothed data line on Figure 50), there seems to be an overall reduction on the fraction of intragranular δ. The volume fraction of intragranular δ at the end of the test would be between approximately 0.4% and 4%.

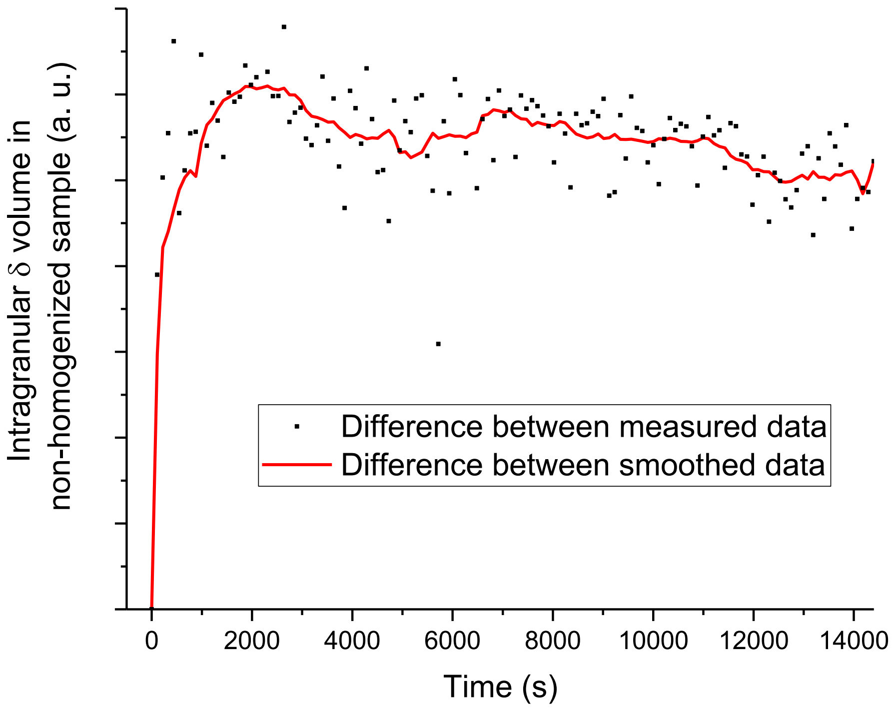

Figure 50: Intragranular δ volume calculated for the non-homogenized sample based on a subtraction of the data in Figure 49. Final calculated intragranular δ volume is between 0.4% and 4%.

CalPhaD assessments

On a previous publication, we demonstrated that the Scheil method [68] can be used to derive compositional maps for an as-built alloy 718 microstructure [81]. The first CalPhaD assessments aimed to understand if homogenization or precipitate formation took place during fabrication. Two pathways were followed to identify if any evolution of the microstructure was taking place. The first was to identify the TTT curves for γ” phase. Calculations were also done for δ but are not shown since this phase formation was always slower than γ”. The compositions used were based on the compositional map derived in [81]. The compositions for different regions of the cellular structure were averaged and used to perform precipitation reaction simulations on software Thermo-Calc® [24]. Nucleation was modelled as homogeneous (nucleation in the matrix, not assisted by dislocations). Default values were used for the interfacial and nucleation barrier energies. Only elements Ni, Cr, Fe, Nb, Mo, Ti and Al were used in the simulation. Figure 51 shows a plot for the time at which the γ” phase reaches 0.01% of equilibrium fraction.

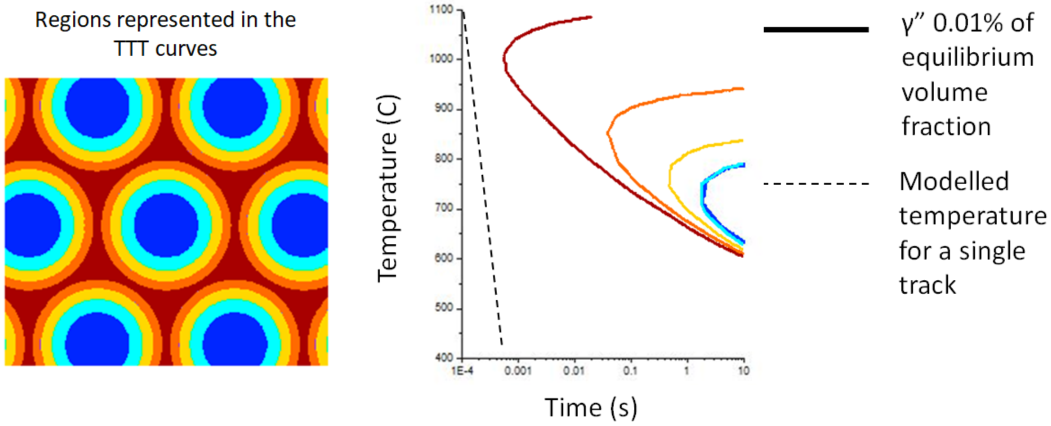

Figure 51: TTT curves for different regions of the cellular structure. The composition used for determining the curves was averaged from the dendritic regions color coded in the schematic representation of the cell structure.

As expected, the kinetics of transformation are much faster in the interdendritic regions than in cell cores, due to segregation of Nb. A similar study has been performed for additively manufactured alloy 625 [69] and found similar results. Nonetheless, due to the high cooling rate experienced by these materials, it is unlikely that any considerable γ” formation takes place. The cooling rate plotted comes from heat and fluid flow simulations from the modelling of a case similar to the one presented here [59]. This is in accordance with the observations in the as-built material.

Homogenization during cooling was also explored by diffusion simulations done on software Thermo-Calc®. These were done by creating a system with cylindrical geometry with a radius of 500 nm. The center of the modelled volume was the center of the cell, and the composition was taken from the compositional profile in [81]. The temperature evolution was taken from [59]. Two passes were considered. The simulation was performed with all elements on Table 8. Figure 52 shows the temperature evolution with time, the initial composition profile in the system, and the composition of C across the system at three different points, the initial profile, after the first pass, and after the second pass. Only C is shown because the compositional change in other element compositions was negligible. Although only two passes were considered, this indicates that except for C, the compositions derived from the Scheil model used in [81] can be directly used in the evaluation of post-build heat treatments, without need for simulations involving temperature variations during the build process. This is because temperature increase due to adjacent passes is not significant after a few passes, and the peak temperature (where most solute flow takes place) drops with each subsequent pass. This discussion is valid for bulky designs and may not be valid for thinner walls or sections with necking profiles, where heat buildup can be significant.

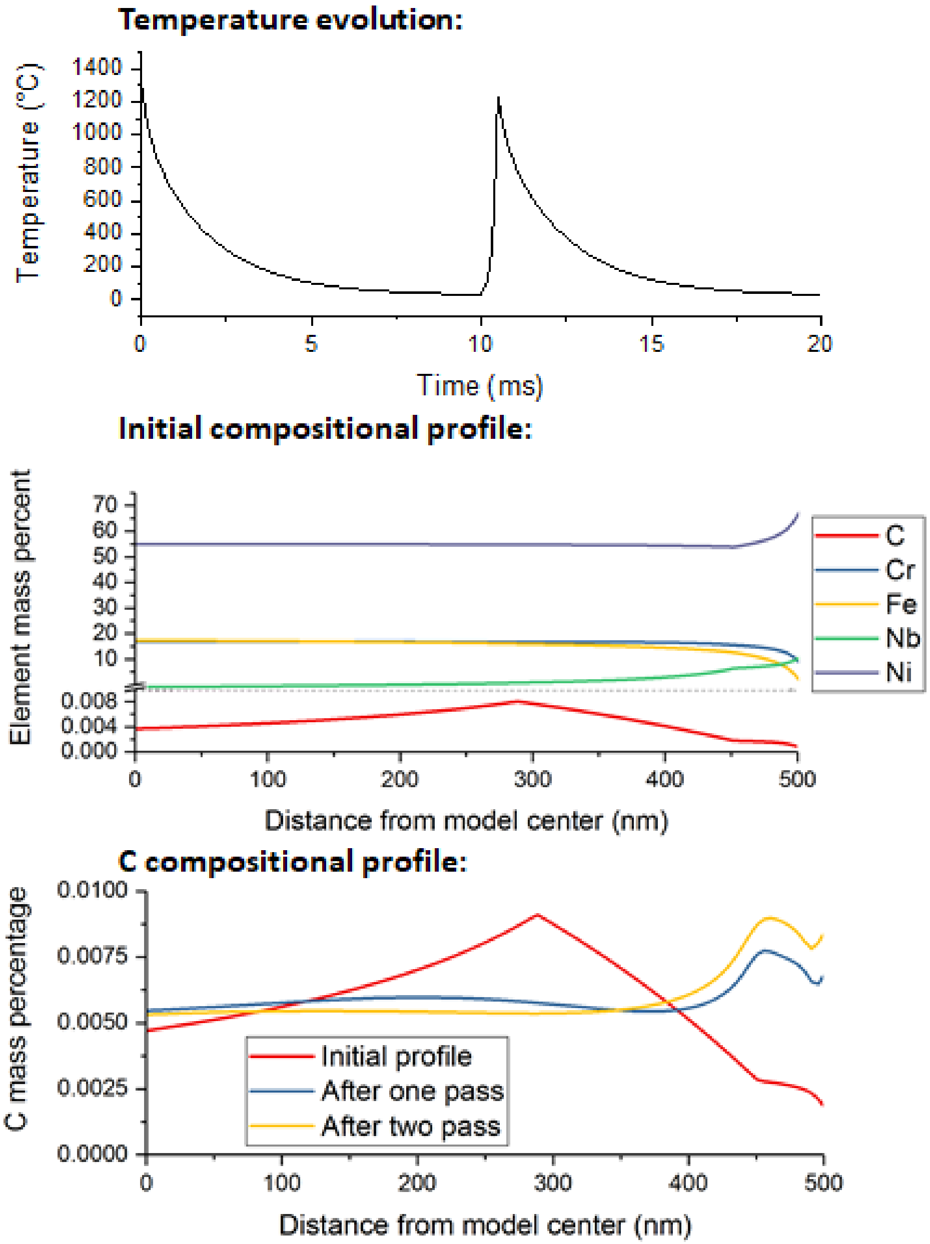

Figure 52: Temperature profile, initial compositional profile and C compositional profile results for the model of the evolution of the segregation profile during the AM build process. C results are shown at 0, 10 and 20 ms. Compositional variation of the substitutional solute elements was negligible and is not shown.

To evaluate how the system would respond at 800 ºC, the solvus temperatures for γ” and δ were evaluated for the matrix compositions along the dendrite radius. The compositions along the radius were defined based on the results on [81]. The solvus determination was done on Thermo-Calc® by only allowing the matrix γ phase and precipitate phase in the system and running an equilibrium calculation where the molar fraction of the precipitate phase was fixed as zero. Database TCNI8 was used, and all elements on Table 8 were included in the calculations. Figure 53 shows the results. The liquid temperature was taken from a Scheil simulation. As discussed in [81], The Scheil method over predicted the solidification temperature range for this material, as it did not consider an increase in the solute partition towards the solid due to lack of complete mixing in the liquid. If this were considered, solidification would end at approximately 1175 ºC. The liquid solvus curve becomes dashed beyond this temperature. Due to the way the calculations were made, the solvus temperature for δ phase goes above the liquid. This curve is also dashed beyond this point.

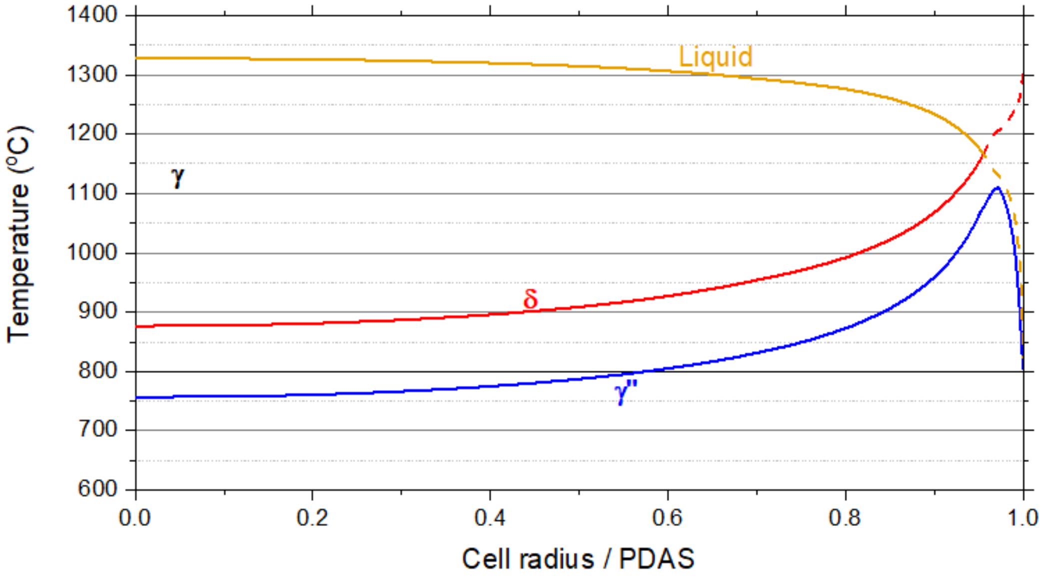

Figure 53: Solvus lines for the Liquid, δ and γ" phases calculated for the modelled composition across the cell.

Figure 53 shows that at 800 °C, δ phase is stable throughout the whole cell. γ" is only stable at regions where the cell is more enriched in Nb. Even with the overestimation of the solidification temperature at the dendrite edge, the Scheil method does not predict a liquid phase at this temperature. To simulate δ formation in the system, a diffusion simulation was set up in Thermo-Calc®. The simulation volume was set with a cylindrical geometry. The radius of the model was set as 505 nm, with its center set as the dendrite core and the edge as the interdendritic region. Two regions were used, one for the matrix with 100 linearly spaced grid points and 500 nm length, and one for Laves phase, with 10 grid points and 5 nm length. The 5nm length corresponds to the approximately 2% volume for the Laves phase detected in [81]. The simulations were performed using a simplified composition of Ni, Cr, Fe, Mo and Nb. Other elements were removed due to their small concentrations. C was also disregarded. The small fraction of C remaining on the matrix was close to the saturation concentration and would have little effect on the system.

Homogeneous nucleation of δ requires a long incubation time, and as such this phase is typically observed in grain boundaries or having γ” particles as its precursor. However, at the dendrite edge, the undercooling regarding the solvus temperature is such that nucleation of this phase can be expected. Additionally, the interfaces between adjacent cells are decorated with dislocations, aiding in the nucleation of δ. As such, to simulate δ growth, an inactive δ phase was added at the edge of the system between the matrix and Laves regions. Activation of this phase was induced in the first time step of the simulation. As for γ”, homogeneous nucleation is typically observed and can happen quickly. As seen on Figure 53, γ” would be stable for some of the dendrite radius. On the modelling software used, it is not possible to model the short-range diffusion controlled nucleation and growth of γ” concomitantly to the long range diffusion controlled growth of δ. However, it is possible to consider diffusion on a two-phase matrix through the use of a homogenization model within Thermo-Calc®. To analyze the effect of the presence of γ”, two versions of the model were run, one where the matrix region was comprised of only a disordered FCC phase (γ), and one where γ and γ” are present. In the second model, when γ” is added, its equilibrium amount will be present at each grid point in the simulation, with the actual phase molar fraction determined by the current composition of that point.

Figure 54 shows a comparison between the two models, and the calculated volume fraction from Figure 54. It should be noted that although the modelled and calculated curves are not in the same scale, the actual δ volume fraction at the end of the test is estimated between 0.004 and 0.04.

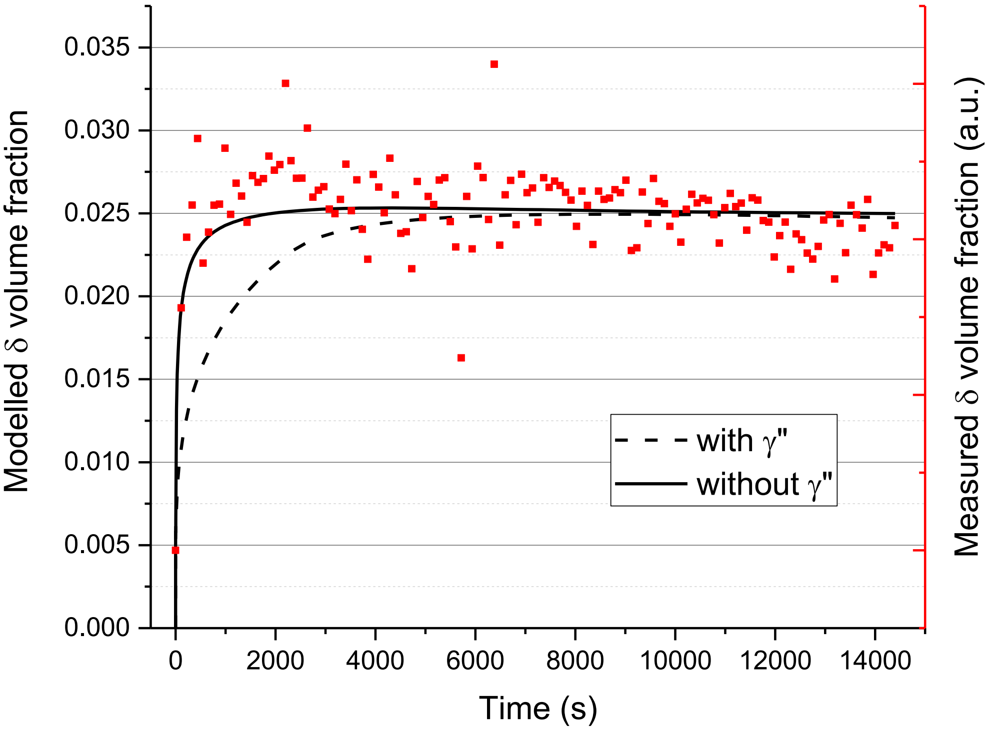

Figure 54: Comparison between calculated and modelled δ volume fraction. Due to high uncertainty in the δ volume fraction measurements, the modelled and calculated results are not in the same scale. The final measured δ volume fraction is between 0.004 and 0.4.

Although there is considerable noise in the calculated δ volume fraction, the transformation kinetics match well with the model without γ”. The reduced kinetics for the model with γ” is due to two reasons. First, the model does not consider diffusion on the γ” phase. This is appropriate since diffusivity on this phase will be orders of magnitude smaller than in the γ phase due to the ordering of the crystal structure [91]. On the homogenization model used, the diffusivity over the volume will be a combination of the diffusivities of the phases present, and necessarily smaller than the diffusivity of γ, since γ” is a diffusionless phase [92]. The second reason is that much of the solute creating a compositional profile in the matrix will be consumed into the formation of γ”, thus reducing the steepness of the compositional profile and the amount of solute available to feed the δ phase growth.

The match between the observed volume fraction and the results from the model without γ” should not be taken as evidence that no γ” exists in the non-homogenized sample. The model with γ” represents an extreme case where the fraction of γ” reaches its equilibrium composition at each grid point instantaneously. If the local growth kinetics of γ” were considered at each grid point, the kinetics of δ growth would increase. Nonetheless, the results from the model without γ are still a better match, suggesting that if there is γ”, its volume fraction across the cell is negligible.

The δ volume fraction in the model without γ” reaches a maximum at around 4000 s and experiences a small reduction afterwards. This happens as Nb close to the γ/δ interface move through the matrix towards the cell core, which is undersaturated with Nb. As more solute moves towards the cell core, the Nb content at the γ side of the interface drops below the saturation point. The neighboring δ phase recedes feeding more Nb to the γ phase and keeping the interface at equilibrium. If the trend line for the calculated δ volume fraction is considered, this reduction should be larger. For this to be the case in the modelled system, a smaller solute content would need to be present in a larger region of the matrix. This could be an indication that the Scheil modelling approach is incorrectly predicting the cell composition distribution. However, as discussed in [81], the opposite is most likely true, that is, if the Scheil model is incorrect, it is because it is underpredicting solute compositions at the dendrite core. Nonetheless, the reduction in calculated δ volume fraction could also be due to some difference between the transformation behavior in the homogenized and non-homogenized samples.

4.2.4. Summary and Conclusions

Modelling of solid-state transformations was done for a laser powder bed additively manufactured alloy 718 material. Modelling was used to identify the evolution or lack thereof of precipitation and matrix compositional homogenization during build, and to identify intragranular δ phase formation and growth in an as-built matrix held at 800 ºC.

To evaluate the modelling efforts, the as-built microstructure was characterized through electron microscopy and microstructural results matched modelling predictions.

The microstructure evolution of a homogenized and non-homogenized sample was compared to evaluate the model for δ growth. The homogenized sample presented evidence of δ at grain boundaries after heat treatment. The non-homogenized sample presented δ both at grain boundaries and inside grains. When inside grains, δ distribution followed the segregation profile of the as built sample. Measurements of δ phase fraction resolved against time for the two cases were used to calculate the fraction of intragranular δ for the non-homogenized sample.

Two conditions were evaluated for δ growth model at 800 ºC, one where γ” was present at its equilibrium concentration across the matrix, and one where γ” was not allowed to form. The second model matches well the calculated intragranular δ volume fraction.

Overall results show that the modelling approach used is consistently matching microstructural observations. However, more investigation is still necessary in other conditions. As we discussed before, γ” formation was negligible during the heat treatment. At lower temperatures, the higher driving force for this phase combined with the slower kinetics for δ growth will create an opportunity for considerable γ” formation. Due to limits in the simulation software, it may not be able to represent this condition fully but may still give a sufficiently accurate representation of the transformation kinetics.

Nonetheless, both on [81] and on this work, little input was needed from microstructural observations and most of the decisions in the modelling effort were taken based on independent calculations. This verifies the potential of the Scheil equation as an input for the segregation profile during AM for the subsequent modelling of heat treatments. Even with some uncertainty due to simulation limits, this approach generated quick and accurate predictions on microstructure behavior.

4.2.5. Acknowledgements

This research is supported in part by U.S. NASA ESI Program, under Award No. NNX17AD13G. All microscopy data was collected at the Center for Electron Microscopy and Analysis at the Ohio State University. All synchrotron data was collected at the Brazilian National Nanotechnology Laboratory. (LNLS) The authors would like to thank Dr. Adam Hope from Thermo-Calc® and Leonardo Wu from LNLS for their support. G. Abreu Faria would like to thank the American Welding Society for a graduate research fellowship.

Chapter 5. Concluding Remarks

This Chapter reflects on the observations taken during the investigations presented in Chapters 3 and 4, specifically referring to the modelling approach used. In the first session, we discuss how the model has been used, the sensibility to input and potential shortcomings. On the second session, we summarize the conclusions that can be drawn from this work. On the third section, we suggest applications which can further understanding of the model limitations, and avenues of work which can improve and broaden its application.

5.1. Discussion

Chapters 3 and 4 present apposite cases for solidification, as shown on Figure 4, but also opposite in terms of how the model was run and results were analyzed. On Chapter 3, much of the materials history is lost. As such, many of the modelling inputs had to be estimated. Despite the quantitative outputs of the model, the conclusions are qualitative. The model showed was that during solidification there was partitioning of Cu, this partitioning remained down to the service temperature, and at the service temperature conditions were present that allowed nucleation and growth of a Cu phase in specific regions of the microstructure. This matched microstructural observations.

On Chapter 4, there was plenty of accurate information required for model inputs and microstructural characterization was available for all steps of the modelled history. Model predictions matched microstructural characterization in terms of volume fraction of phases, microstructural morphology and transformation rates. In Chapter 3, many of the decisions taken when setting up the model were not based on microstructural observations simply because those were not available. In Chapter 4 the decisions made were also mostly independent of the observed microstructure, mostly to verify the robustness of the modelling approach.

Mostly, the modelling approach microstructural predictions matched observed microstructures in both studied cases. It should be noted however that it was not possible to verify the level of accuracy in this match given limitations in the characterization results. Particularly, the techniques necessary for quantifying the Nb content in a specific point of a cell or the volume fraction of δ phase have intrinsic uncertainties that are carried out as noise in the collected data. Additionally, many of the experiments necessary to obtain the microstructural data are challenging enough that obtaining statistical data is unfeasible, for example, obtaining a FIB foil which intersects a creep cavity. As such, modelling predictions match the microstructure within the statistical and uncertainty limits of the characterization data.

Additionally, the systems modelled aimed to represent the bulk of the solidified volume. Many of the decisions made during modelling will only apply to a general description of the molten material. In many solidifying systems there will be regions of the melt with local conditions promoting compositional changes, a change in solidification morphology or local thermal history. These can still be modelled using this approach, but such conditions must inform the model application.

Some comments may be made on the different inputs required and models used on the modelling approach:

$C_s = f(f_s)$ *Equation*

In all results shown, the $C_s = f(f_s)$ equation used was the non-equilibrium lever-rule, or Scheil equation. As demonstrated in the background session, substitutional solute back-diffusion is negligible in most solidification-based manufacturing processes. Some discussion is still warranted for incomplete mixing in the liquid and solute trapping. As demonstrated in session 4.1.4, both phenomena would promote a change in the predicted compositional profile which is within the scatter in the compositional measurements. However, with any change in the system, such as alloying composition or process parameters, these phenomena may have a more marked effect. Using the Giovanola-Kurz model requires empirical inputs and using the Aziz trapping function requires understanding the interface speed variation for the whole solidified volume. This does not necessarily mean that the models need to be calibrated with experiments. Parameters for both functions can be defined using other modelling techniques, such as phase-field methods, as done by [57].

It is still remarkable that the Scheil equation is applicable in such a wide range of solidification conditions. Since diffusion in the solid can be dismissed in most cases, the validity of the Scheil approach rests in the validity of the complete liquid mixing hypothesis. The fact that this hypothesis is reasonable for most solidification conditions can be understood by a discussion on diffusion. In diffusion problems, time and the square of diffusion distance are interchangeable. For example, if a material solidification temperature range is 100 ºC and the material is cooled at 10 ºC/s, there is a 10 s time for the solute in the liquid to homogenize. If the cooling rate is increased to 10^4 ºC/s, the time for solute to diffuse drops considerably. However, as the cooling rate increases, the interdendritic or intercellular spacing decreases, as shown in the relations displayed in Figure 4. The diffusion problems at 10 ºC/s and 10^4 ºC/s become equivalent, diffusion distance required for complete liquid mixing drops as the time available for the liquid to homogenize increases. This ensures that the hypothesis used in the Scheil model are consistent for several solidification phenomena. However, a case by case analysis should still be pursued as this will depend on the specific solidification morphology relations of the material and specific diffusivity of solute in the liquid.

Metastable Condition

In most inputs for the model, the information required for the input can be determined by independent fundamental or empirical materials models. Identifying if solidification happens in a metastable condition and what phases are present in such a condition is the exception. In all cases studied in this work, the equilibrium state of solidification was determined by literature review and confirmed by microstructural observations. This is a weak point of the modelling approach as the metastable condition will be dependent on processing parameters. For example, as reported in [13], the as-solidified phase fractions of a steel will change depending on the welding process used, mostly tied to the relationship between cooling rate and the kinetics of the phase transformations during solidification. As such, previous observations on one material processed under one condition will not necessarily translate to another condition, or to another material of similar composition.

This may be addressed by a fundamentally based empirical approach. A metastable diagram is constructed by eliminating phases. The phases to be eliminated may be chosen based on an argument about kinetics. There are fundamental models for the nucleation rate of a phase in a liquid which are mainly governed by the nucleation driving force, and the driving force for nucleation can be derived from CalPhaD. A nucleation rate threshold can be defined empirically to identify if a phase would be present in a solidification microstructure, and this criterion used to identify the phases in the metastable phase diagram.

Solidification Morphology

In the cases studied two different morphologies were studied, dendritic and cellular. In the second case, a good match was observed between model prediction and observations. In the first case, it was not possible to compare a modelled compositional map with observations. In both cases, the strategy used to identify the microsegregation distribution in the solidification microstructure is the same. However, the accuracy found in the cellular case will likely not be reproduced in the dendritic case. There should exist some compositional difference between the primary dendrite core and secondary dendrite core as they are formed under different temperature conditions, and this is never considered on the observations on Chapter 3. Rather, Chapter 3 solidification simulations should be read as: there is enough concentration of a specific solute atom close to solidification second phase particles, and this local enrichment explains the solid-state transformation and resulting microstructure observed. However, as shown on Chapter 3 and 4, there is very little compositional variation over the first 50% of solid to form. As such, the morphological nature of the dendrite as it starts to grow is of little importance, and a better question to be asked is how it grows, meaning, is the solid/liquid interface planar, cylindrical, spherical or even anisotropic. In the results shown, considering the interface as cylindrical was successful. It would be interesting to verify how this approach fares in other morphologies such as planar or equiaxed, even if these morphologies are not as commonly observed when compared to the dendritic and cellular.

As for the length scale of the solidification morphology, both empirical and fundamental models were used, with successful results. The fundamental model, Kurz-Fisher's equation, was very successful, and the modifications used make it versatile for a wide range of alloying conditions. This model does have the drawback of necessitating thermal history information which is not easily attainable, such as local temperature gradients.

Temperature History

The temperature history input is required for most of the decisions made during modelling. It will inform the length scale for the microsegregation distribution, the choice of $C_s = f(f_s)$ equation to be used, the solid-state models, and may affect the metastable condition to be used. As such this is the first information to be sourced before any implementation of the modelling approach. Some discussion is warranted on the dependency of the model results on the thermal history provided. Most of the effect of the thermal history on the model will happen through the length scale of the solidification structure. As discussed in Chapter 3, this can change the model results drastically. However, the cell spacing dependence on cooling rate is quite small, especially for finer microstructures. In Chapter 3 for example, a variation of two times in the SDAS required a variation of ten times in the cooling rate. Thus, the thermal history information does not need high accuracy, meaning, if the order of magnitude of the cooling rate is defined, this is enough to run an accurate simulation. As such, simplified heat and fluid flow models or literature sourced typical values for the manufacturing process being studied are enough for the modelling approach.

Solid State Diffusion and Phase Transformation models

The models for segregation used are advantageous because of their compositional versatility. This versatility is somewhat lost when the solid-state models used are considered. In all shown cases, computational limitations prevented the usage of the full compositional information available. Different strategies were used to down select the composition. In Chapter 3, the temperature condition of the simplified system had to be modified for it to accurately represent the complete system. All modifications required heavy user intervention and decision making. The solidification model used is straightforward and easily automated. This is not the case for the solid-state models. However, there is room for improvement. The down-selection of elements can be done by comparing element activities or their effect on the system's interdiffusion coefficients. Similar to what was discussed for the metastable condition, this can be codified in an algorithm and reduce the need for any user input. However, any implementation would require extensive testing and validation.

5.2. Conclusions

- A prototype of a modelling approach was developed based on a hierarchical application of different CalPhaD based models for phase transformations. The model was applied in two application cases and in both, yielded successful predictions of the final observed microstructure.
- The Scheil equation was used for solidification simulations. This approach was successful in all observed cases and should be applicable is a wide range of conditions. In cases in which it isn't, other segregation models can be implemented with little change to the model framework.

- The segregation profile description worked well for a cellular solidification structure and yielded accurate predictions when applied to a dendritic structure. It should still be tested against other solidification morphologies.
- The solid-state portion of the modelling approach required constant user input. At this point, the approach has potential to be automated, but it is not ready for such. Automation would require the development of some decision-making algorithms for identifying metastable conditions, element down-selection, etc.

5.3. Future Work

In this work, we attempted to develop a roadmap for the creation of a unified CalPhaD modelling framework for identifying and characterizing phase transformations on a segregated microstructure. Several avenues of work can be drawn to further both the applicability of the modelling approach, and its limitations in its present state. These are listed below:

- We discussed beforehand that the Scheil model was applicable in a broad range of solidification conditions. Furthermore, in Chapter 4 we identified that the prediction of the Scheil method for the fraction of Laves phase at the end of solidification in alloy 718 matched experimental observations. Reference [65] presents a review of volume fraction of Laves present in a 718 alloy composition for various processes (Figure 55). Scheil does not depend on solidification conditions, so either the Scheil method does not represent the systems being analyzed, or there is some Laves formation on the solid state. The modelling approach should be implemented, using Scheil and other methods such as Brody-Flemings, for the range of processing conditions presented on Figure 55 to verify if results are accurate and if not, identify where the modelling approach is failing to represent the microstructure.

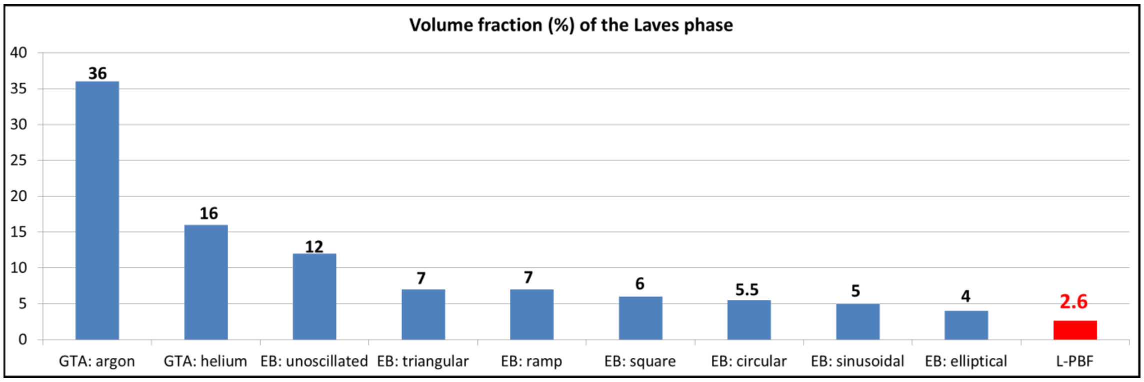

Figure 55: Laves volume fraction for as-solidified microstructures on alloy 718 measured for several processes. From [65].

- Another interesting system to be studied using this modelling approach is Cu bearing Al alloys. Like alloy 718, these are precipitation strengthened alloys in which the precipitate forming element heavily segregates during solidification. A205 is a Cu, Ti and B bearing Al alloy developed for casting, but becoming increasingly popular in AM applications[93]. During solidification, these alloys solidify mostly as fine equiaxed grains (Figure 56). This represents a unique solidification morphology, and implementing the modelling approach for this application case would either prove its versatility, or identify flaws in its applicability.

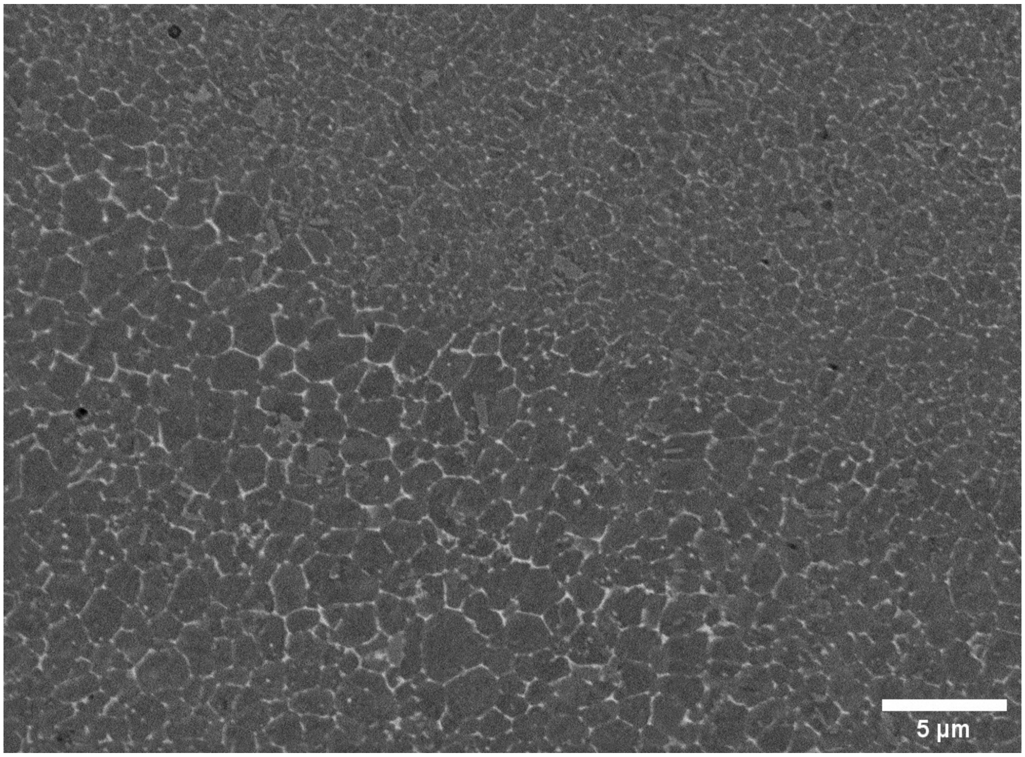

Figure 56: Backscattered electron image of as-built microstructure of A205 alloy produced by Laser powder bed additive manufacturing. All grains are equiaxed and polygonal. No sign of columnar or dendritic structure is observed.

- There is an opportunity for codifying some of the decision-making process behind the model. As was discussed in 5.1, this refers to the development of algorithms to identify metastable phases in a solidification condition, or to perform element down-selection before a solid-state phase transformation simulation. Achieving this would require the establishment of a rigorous and broad matrix of conditions to be tested, along with sourcing or production of microstructure characterization results for validation. Nonetheless, such algorithms would be useful not only in the context of this modelling approach, but also for researchers performing other types of simulations on new systems for which characterization data is scarce, such as High Entropy Alloys.

- In session 4.2, we discussed the possibility of two phase transformations happening concomitantly on a segregated microstructure, local precipitation (γ”) together with long-range diffusion fueled growth of another phase (δ). In that session, we concluded that local precipitation was negligible for the condition studied, but at lower temperatures, it would likely not be. In the current modelling framework, the two phenomena cannot be correctly simulated concomitantly. However, by modifying the models used, it can be. Mean field models can be used to identify local precipitation behavior, whereas the mass flow model can be used to identify long-range diffusion in a two-phase region. If the two models are run concomitantly, this behavior can be represented. This would be done as follows:
    - Diffusion module runs one time iteration from t to t+Δt. Composition for each cell is retrieved on t.
    - Mean-field simulations are performed for each cell with the compositions derived on previous step from t to t+Δt. Precipitate compositions and volume fractions are retrieved.

- Compositions and phase fractions from precipitation module are fed on each cell on the diffusion module. Simulations start again taking initial time as t+Δt.

This can be implemented using the Thermo-Calc® Software Development Kit and compared with characterization results where the two phenomena are happening concomitantly.

References

[1] J. N. DuPont, J. C. Lippold, and S. D. Kiser, *Welding Metallurgy and Weldability of Nickel-Base Alloys*. Wiley, 2009.

[2] A. D. Pelton, “Phase Diagrams,” in *PHYSICAL METALLURGY*, Fourth., R. W. Cahn and P. Haasen, Eds. Elsevier B.V., 1988, pp. 475–533.

[3] N. Saunders and P. Miodownik, *CALPHAD (Calculation of Phase Diagrams): A Comprehensive Guide*, vol. 1. Pergamon, 1998.

[4] H. L. Lukas, S. G. Fries, and B. Sundman, *Computational thermodynamics : the CALPHAD method*. Cambridge University Press, 2007.

[5] B. Sundman, “Modification of the two-sublattice model for liquids,” *Calphad*, vol. 15, no. 2, pp. 109–119, Apr. 1991.

[6] H. Biloni and W. J. Boettinger, “Solidification,” in *PHYSICAL METALLURGY*, 4th editio., R. W. Cahn and P. Haasen, Eds. Elsevier B.V., 1988, pp. 670–842.

[7] Q. Chen and B. Sundman, “Computation of Partial Equilibrium Solidification with Complete Interstitial and Negligible Substitutional Solute Back Diffusion,” 2002.

[8] J. C. Lippold, *Welding Metallurgy and Weldability*, vol. 9781118230. Wiley, 2014.

[9] T. Bower, H. Brody, and M. C. Flemings, “Measurments of Solute Redistribution in Dendritic Solidfication,” *Trans. Metall. Soc. AIME*, vol. 236, no. May, pp. 624–634, 1966.

[10] B. GIOVANOLA and W. KURZ, “Modeling of Microsegregation under Rapid Solidification Conditions,” *Metall. Trans. A* , vol. 21A, no. January, 1990.

[11] M. E. Glicksman, *Principles of Solidification*. New York, NY: Springer New York, 2011.

[12] C. J. (Colin J. Smithells, W. F. (William F. Gale, and T. C. (Terry C. . Totemeier, *Smithells metals reference book.* Elsevier Butterworth-Heinemann, 2004.

[13] S. A. David, J. M. Vitek, R. W. Reed, and T. L. Hebble, “Effect of rapid solidification on stainless steel weld metal microstructures and its implications on the Schaeffler diagram,” Oak Ridge, TN, Sep. 1987.

[14] D. M. Stefanescu, *Science and engineering of casting solidification, second edition*. 2009.

[15] H. Jacobi and K. Schwerdtfeger, “Dendrite morphology of steady state unidirectionally solidified steel,” *Metall. Trans. A*, vol. 33A, pp. 3747–3754, 1976.

[16] I. Y. Suzuki A, Suzuki T, Nagaoka Y, “No Title,” *Nippon Kingaku Gakkai Shuho*, vol. 32, 1968.

[17] S. Milenkovic, M. Rahimian, I. Sabirov, and L. Maestro, “Effect of solidification

parameters on the secondary dendrite arm spacing in MAR M-247 superalloy determined by a novel approach," *MATEC Web Conf.*, vol. 14, p. 13004, Aug. 2014.

[18] R. Acharya, J. A. Sharon, and A. Staroselsky, "Prediction of microstructure in laser powder bed fusion process," *Acta Mater.*, vol. 124, pp. 360–371, Feb. 2017.

[19] P. Sahu, a. S. Hamada, S. Ghosh Chowdhury, and L. P. Karjalainen, "Structure and microstructure evolution during martensitic transformation in wrought Fe–26Mn–0.14C austenitic steel: an effect of cooling rate," *J. Appl. Crystallogr.*, vol. 40, no. 2, pp. 354–361, Mar. 2007.

[20] L.-Q. Chen, "Phase-Field Models for Microstructure Evolution," *Annu. Rev. Mater. Res.*, vol. 32, no. 1, pp. 113–140, Aug. 2002.

[21] T. DebRoy *et al.*, "Additive manufacturing of metallic components – Process, structure and properties," *Prog. Mater. Sci.*, vol. 92, pp. 112–224, Mar. 2018.

[22] M. J. Aziz, "Model for solute redistribution during rapid solidification," *J. Appl. Phys.*, vol. 53, no. 2, pp. 1158–1168, Feb. 1982.

[23] J.-O. O. Andersson *et al.*, "Thermo-Calc & DICTRA, computational tools for materials science," *Calphad Comput. Coupling Phase Diagrams Thermochem.*, vol. 26, no. 2, pp. 273–312, Jun. 2002.

[24] Q. Chen, K. Wu, G. Sterner, and P. Mason, "Modeling Precipitation Kinetics

During Heat Treatment with Calphad-Based Tools," *J. Mater. Eng. Perform.*, vol. 23, no. 12, pp. 4193–4196, Dec. 2014.

[25] R. W. (Robert W. . Cahn and P. (Peter) Haasen, *Physical metallurgy*. North-Holland, 1996.

[26] F. Masuyama and N. Nishimura, "Phase Transformation and Properties of Gr.91 at Around Critical Temperature," *Exp. With Creep-Strength Enhanc. Ferritic Steels New Emerg. Comput. Methods*, vol. 2004, pp. 85–91, 2004.

[27] Vallourec Industries, *The P91 Book*. 1992.

[28] J. a. Francis, W. Mazur, and H. K. D. H. Bhadeshia, "Review Type IV cracking in ferritic power plant steels," *Mater. Sci. Technol.*, vol. 22, no. 12, pp. 1387–1395, 2006.

[29] D. J. Abson and J. S. Rothwell, "Review of type IV cracking of weldments in 9–12%Cr creep strength enhanced ferritic steels," *Int. Mater. Rev.*, vol. 58, no. 8, pp. 437–473, Nov. 2013.

[30] H. Hongo, M. Tabuchi, and T. Watanabe, "Type IV Creep Damage Behavior in Gr.91 Steel Welded Joints," *Metall. Mater. Trans. A*, vol. 43, no. 4, pp. 1163–1173, Apr. 2012.

[31] F. Masuyama, "Creep degradation in welds of Mod.9Cr-1Mo steel," *Int. J. Press. Vessel. Pip.*, vol. 83, no. 11–12, pp. 819–825, Nov. 2006.

[32] J. S. Lee and K. Maruyama, “Mechanism of microstructural deterioration preceding type IV failure in weldment of Mod.9Cr-1Mo steel,” *Met. Mater. Int.*, vol. 21, no. 4, pp. 639–645, 2015.

[33] EPRI, “The Benefits of Improved Control Of Composition Of Creep-Stregth-Enhanced Ferritic Steel Grade 91,” no. August, pp. 1–15, 2014.

[34] J. Liu, M. Strangwood, C. L. Davis, and J. Parker, “Non-destructive characterisation of N/Al level in P91 steels using electromagnetic sensors Non-destructive characterisation of N/Al level in P91 steels using electromagnetic sensors,” 2014.

[35] S. J. Brett, D. L. Oates, and C. Johnston, “In-Service Type IV Cracking in a Modified 9Cr (Grade 91) Header,” vol. 4, no. 1, pp. 1–11, 2007.

[36] J. Parker and S. Brett, “Creep performance of a grade 91 header,” *Int. J. Press. Vessel. Pip.*, vol. 111–112, pp. 82–88, Nov. 2013.

[37] A. Nitsche, D. Allen, and P. Mayr, “Damage assessment of creep affected weldments of a Grade 91 header component after long-term high temperature service,” *Weld. World*, vol. 59, no. 5, pp. 675–682, Sep. 2015.

[38] K. Sawada, M. Tabuchi, and K. Kimura, “Degradation Mechanism of Creep Strength Enhanced Ferritic Steels for Power Plants,” in *Materials Challenges and Testing for Supply of Energy and Resources*, Berlin, Heidelberg: Springer Berlin Heidelberg, 2012, pp. 35–43.

[39] C. G. Panait, W. Bendick, A. Fuchsmann, A.-F. Gourgues-Lorenzon, and J. Besson, “Study of the microstructure of the Grade 91 steel after more than 100,000 h of creep exposure at 600 °C,” *Int. J. Press. Vessel. Pip.*, vol. 87, no. 6, pp. 326–335, Jun. 2010.

[40] S. C. Bose, K. Singh, A. K. Ray, and R. N. Ghosh, “Effect of thermal ageing on mechanical properties and microstructures of a standard G-X 12 CrMoVWNbN 1011 grade of cast steel for turbine casing,” *Mater. Sci. Eng. A*, vol. 476, no. 1–2, pp. 257–266, Mar. 2008.

[41] H. Cerjak and E. Letofsky, “The effect of welding on the properties of advanced 9–12%Cr steels,” *Sci. Technol. Weld. Join.*, vol. 1, no. 1, pp. 36–42, Feb. 1996.

[42] J. Hald, “Creep strength and ductility of 9 to 12% chromium steels,” *Mater. High Temp.*, vol. 21, no. 1, pp. 41–46, Jan. 2004.

[43] T. Fujita, “Advances in 9-12% Cr heat resistant steels for power plants,” in *Advances in Materials Technology for Fossil Power Plants, Conference, 3*, 2001, p. 512.

[44] J. Parker, “Creep cavitation in CSEF steels,” *Adv. Mater. Technol. Foss. Power Plants - Proc. from 7th Int. Conf.*, no. September, pp. 714–731, 2014.

[45] F. Masuyama, “Advances in Physical Metallurgy and Processing of Steels. History of Power Plants and Progress in Heat Resistant Steels.,” *ISIJ Int.*, vol. 41, no. 6, pp. 612–625, Jun. 2001.

[46] D. M. Stefanescu, “Solidification of Single-Phase Alloys; Cells and Dendrites,” *Sci. Eng. Cast. Solidif.*, pp. 145–196, 2015.

[47] D. Hull and J. D. Bacon, *Introduction to Dislocations, 4th Ed. (Elsevier, 2001)(ISBN 0750646810).pdf*. 2001.

[48] S. Kou, “A criterion for cracking during solidification,” *Acta Mater.*, vol. 88, pp. 366–374, Apr. 2015.

[49] F42.91, “ASTM F2792-12a, Standard Terminology for Additive Manufacturing Technologies, (Withdrawn 2015).” 2012.

[50] R. C. Reed, *The Superalloys fundamentals and applications*, vol. 9780521859. Cambridge: Cambridge University Press, 2006.

[51] H. Song, T. McGaughy, A. Sadek, and W. Zhang, “Effect of structural support on microstructure of nickel base superalloy fabricated by laser-powder bed fusion additive manufacturing,” *Addit. Manuf.*, vol. 26, pp. 30–40, Mar. 2019.

[52] A. Uriondo, M. Esperon-Miguez, and S. Perinpanayagam, “The present and future of additive manufacturing in the aerospace sector: A review of important aspects,” *Proceedings of the Institution of Mechanical Engineers, Part G: Journal of Aerospace Engineering*, vol. 229, no. 11. pp. 2132–2147, 2015.

[53] K. N. Amato *et al.*, “Microstructures and mechanical behavior of Inconel 718 fabricated by selective laser melting,” *Acta Mater.*, vol. 60, no. 5, pp. 2229–2239,

Mar. 2012.

[54] I. Steinbach, “Phase-Field Model for Microstructure Evolution at the Mesoscopic Scale,” *Annu. Rev. Mater. Res.*, vol. 43, no. 1, pp. 89–107, Jul. 2013.

[55] Y. Wang and J. Li, “Phase field modeling of defects and deformation,” *Acta Mater.*, vol. 58, no. 4, pp. 1212–1235, Feb. 2010.

[56] J. Kundin, L. Mushongera, and H. Emmerich, “Phase-field modeling of microstructure formation during rapid solidification in Inconel 718 superalloy,” *Acta Mater.*, vol. 95, pp. 343–356, Aug. 2015.

[57] S. Ghosh, L. Ma, N. Ofori-Opoku, and J. E. Guyer, “On the primary spacing and microsegregation of cellular dendrites in laser deposited Ni–Nb alloys,” *Model. Simul. Mater. Sci. Eng.*, vol. 25, no. 6, p. 065002, Sep. 2017.

[58] L.-X. Lu, N. Sridhar, and Y.-W. Zhang, “Phase field simulation of powder bed-based additive manufacturing,” *Acta Mater.*, vol. 144, pp. 801–809, Feb. 2018.

[59] Y. S. Lee and W. Zhang, “Modeling of heat transfer, fluid flow and solidification microstructure of nickel-base superalloy fabricated by laser powder bed fusion,” *Addit. Manuf.*, vol. 12, pp. 178–188, 2016.

[60] N. Raghavan *et al.*, “Numerical modeling of heat-transfer and the influence of process parameters on tailoring the grain morphology of IN718 in electron beam additive manufacturing,” *Acta Mater.*, vol. 112, pp. 303–314, Jun. 2016.

[61] N. Saunders, M. Fahrmann, and C. J. Small, "The Application of Calphad Calculations To Ni-Based Superalloys," *Superalloys 2000*, pp. 803–811, 2000.

[62] R. R. Dehoff *et al.*, "Site specific control of crystallographic grain orientation through electron beam additive manufacturing," *Mater. Sci. Technol.*, vol. 31, no. 8, pp. 931–938, Jun. 2015.

[63] W. Kurz and D. J. Fisher, "Dendrite growth at the limit of stability: tip radius and spacing," *Acta Metall.*, vol. 29, no. 1, pp. 11–20, Jan. 1981.

[64] W. W. Mullins and R. F. Sekerka, "Stability of a Planar Interface During Solidification of a Dilute Binary Alloy," *J. Appl. Phys.*, vol. 35, no. 2, pp. 444–451, Feb. 1964.

[65] H. Y. Song, "Multi-scale Microstructure Characterization for Improved Understanding of Microstructure-Property Relationship in Additive Manufacturing," The Ohio State University, 2016.

[66] K. E. Easterling, H. K. D H Bhadeshia, and L. Svensson, "Mathematical Modelling of Weld Phenomena, eds H Modelling the Evolution of Microstructure in Steel Weld Metal," *Math. Model. Weld Phenom.*, pp. 109–182, 1993.

[67] E. A. Loria, M. and M. S. S. M. D. Minerals, ASM International., National Association of Corrosion Engineers., and Nickel Development Institute (Canada), *Superalloys 718, 625, 706 and various derivatives : proceedings of the International Symposium on Superalloys 718, 625, 706 and Various Derivatives :*

held June 17-20, 2001. TMS, 2001.

[68] B. Sundman and I. Ansara, “The Gulliver-Scheil method for the calculation of solidification paths,” in *The SGTE Casebook: Second Edition: Thermodynamics At Work*, Woodhead Publishing, 2008, pp. 343–346.

[69] G. Lindwall *et al.*, “Simulation of TTT Curves for Additively Manufactured Inconel 625,” *Metall. Mater. Trans. A*, vol. 50, no. 1, pp. 457–467, Jan. 2019.

[70] H. S. Furtado, A. T. Bernardes, R. F. Machado, and C. A. Silva, “Numerical simulation of solute trapping phenomena using phase-field solidification model for dilute binary alloys,” *Mater. Res.*, vol. 12, no. 3, pp. 345–351, Sep. 2009.

[71] J. F. Radavich, “The Physical Metallurgy of Cast and Wrought Alloy 718,” in *Superalloys 718 Metallurgy and Applications (1989)*, 2004, pp. 229–240.

[72] A. Lingenfelter, “Welding of Inconel Alloy 718: A Historical Overview,” *Superalloy 718 - Metall. Appl. Miner. Met. Mater. Soc.*, pp. 673–683, 2012.

[73] M. Durand-Charre and J. H. Davidson, *The microstructure of superalloys*. Gordon and Breach Science Publishers, 2017.

[74] Y. Huang and T. G. Langdon, “The evolution of delta-phase in a superplastic Inconel 718 alloy,” *J. Mater. Sci.*, vol. 42, no. 2, pp. 421–427, Jan. 2007.

[75] H. Y. Zhang, S. H. Zhang, M. Cheng, and Z. X. Li, “Deformation characteristics of δ phase in the delta-processed Inconel 718 alloy,” *Mater. Charact.*, vol. 61, no.

1, pp. 49–53, Jan. 2010.

[76] SAE, “AMS2773E - Heat Treatment - Cast Nickel Alloy and Cobalt Alloy Parts,” 2013.

[77] V. Beaubois, J. Huez, S. Coste, O. Brucelle, and J. Lacaze, “Short term precipitation kinetics of delta phase in strain free Inconel* 718 alloy,” *Mater. Sci. Technol.*, vol. 20, no. 8, pp. 1019–1026, 2004.

[78] M. Jambor, O. Bokůvka, F. Nový, L. Trško, and J. Belan, “Phase transformations in nickel base superalloy INCONEL 718 during cyclic loading at high temperature,” *Prod. Eng. Arch.*, vol. 15, pp. 15–18, Jun. 2017.

[79] H. E. Chandler, *Heat treater’s guide : practices and procedures for nonferrous alloys*. ASM International, 1996.

[80] G. A. Knorovsky, T. J. Headley, A. D. Romig, and M. J. Cieslak, “The Solidification Metallurgy of Alloy 718 and Other Nb-Containing Superalloys,” *Superalloy 718 - Metall. Appl. Miner. Met. Mater. Soc.*, pp. 59–78, 1989.

[81] G. Abreu Faria, K. Kadirvel, A. Hinojos, W. Zhang, Y. Wang, and A. J. Ramirez, “On the use of metastable interface equilibrium assumptions on prediction of solidification micro-segregation in laser powder bed fusion,” *Sci. Technol. Weld. Join.*, vol. 24, no. 5, pp. 446–456, Jul. 2019.

[82] G. A. Faria, “Exploring Metallic Materials Behavior Through In Situ

Crystallographic Studies," State University of Campinas, 2014.

[83] G. A. Faria *et al.*, "Advanced Facility For Parallel Thermo-Mechanical Simulation And Synchrotron X-Ray Diffraction," in *In-situ Studies with Photons, Neutrons and Electrons Scattering II*, 1st ed., T. Kannengiesser, S. S. Babu, Y. Komizo, and A. J. Ramirez, Eds. Springer, 2014, pp. 245–259.

[84] B. H. Toby and R. B. Von Dreele, "*GSAS-II* : the genesis of a modern open-source all purpose crystallography software package," *J. Appl. Crystallogr.*, vol. 46, no. 2, pp. 544–549, Apr. 2013.

[85] T. Degen, M. Sadki, E. Bron, U. König, and G. Nénert, "The HighScore suite," *Powder Diffr.*, vol. 29, no. S2, pp. S13–S18, Dec. 2014.

[86] E. A. Lass, M. R. Stoudt, M. B. Katz, and M. E. Williams, "Precipitation and dissolution of δ and γ″ during heat treatment of a laser powder-bed fusion produced Ni-based superalloy," *Scr. Mater.*, vol. 154, pp. 83–86, Sep. 2018.

[87] W. Kraus and G. Nolze, "*POWDER CELL* – a program for the representation and manipulation of crystal structures and calculation of the resulting X-ray powder patterns," *J. Appl. Crystallogr.*, vol. 29, no. 3, pp. 301–303, Jun. 1996.

[88] F. Zhang *et al.*, "Homogenization kinetics of a nickel-based superalloy produced by powder bed fusion laser sintering," *Scr. Mater.*, vol. 131, pp. 98–102, 2017.

[89] M. Anderson, A. L. Thielin, F. Bridier, P. Bocher, and J. Savoie, "δ Phase

precipitation in Inconel 718 and associated mechanical properties," *Mater. Sci. Eng. A*, vol. 679, no. January 2016, pp. 48–55, 2017.

[90] S. Azadian, L. Y. Wei, and R. Warren, "Delta phase precipitation in inconel 718," *Mater. Charact.*, vol. 53, no. 1, pp. 7–16, 2004.

[91] P. Shewmon, *Diffusion in Solids*, 2nd ed. Warrendale, USA: The Minerals, Metals & Materials Society, 1989.

[92] H. Larsson and L. Höglund, "Multiphase diffusion simulations in 1D using the DICTRA homogenization model," *Calphad*, vol. 33, no. 3, pp. 495–501, Sep. 2009.

[93] B. Stott and J. Forde, "A20X - alloy of the future?," *Mater. World*, vol. 17, no. 11, 2009.